Université de Sherbrooke

Faculté de génie

Département de génie chimique et de génie biotechnologique

Développement d'un nouveau modèle mathématique pour analyser l'effet des paramètres de conception et de fonctionnement sur la consommation d'énergie de cellules d'électrolyse en sels fondus

Development of a new mathematical model to analyse the effect of design and operating parameters on the energy consumption of molten salt electrolysis cells

Thèse de doctorat

Spécialité : génie chimique

Elaheh Oliaii

Jury : Prof. Martin Désilets (directeur)
Prof. Pierre Proulx
Prof. Gisele Azimi
Dr. Gaétan Lantagne

Sherbrooke (Québec) Canada April 2018

Aux lecteurs.

Résumé

Cette thèse présente une étude sur le transfert de masse et la consommation d'énergie dans une cellule d'électrolyse au lithium, dernière étape du processus de production du lithium. En raison de l'environnement sévère (température élevée et existence de matériaux corrosifs), l'obtention de données expérimentales dans une telle cellule est très difficile. Cependant, l'analyse numérique peut aider à surmonter le manque de connaissances. La complexité des équations pour résoudre différents champs couplés (concentration, potentiel et vitesse) et les réactions sont un obstacle au développement d'un modèle fiable. D'après les connaissances de l'auteure, à l'exception des publications présentées dans cette thèse, aucune étude n'a été publiée auparavant sur l'analyse numérique des phénomènes susmentionnés dans la cellule au lithium, ce qui met en évidence l'originalité de la présente thèse.

Le transfert de masse, la distribution de vitesse et de tension ont été simulés à l'intérieur de deux types de cellules au lithium: une cellule avec un diaphragme et une cellule sans diaphragme. Les simulations sont réalisées à l'aide d'un logiciel commercial, COMSOL®, et d'un code développé avec une boîte à outils à accès libre, OpenFOAM. Les cas de référence ont été simulés en fonction de la géométrie et des conditions d'opération d'un banc expérimental conçu et exploité chez Hydro-Québec. La comparaison des résultats expérimentaux et de simulation pour le champ électrique confirme la validité du modèle. En outre, les résultats expérimentaux et de simulation du champ d'écoulement dans une cellule de magnésium similaire à celle d'une cellule au lithium, résultats disponibles dans la littérature publique, ont été utilisés pour la validation des modèles d'écoulement à une et à deux phases.

Pour chaque type de cellules au lithium, les résultats pour les champs de vitesse, de potentiel et de concentration sont présentés dans des sections séparées. Les résultats montrent que la consommation d'énergie des cellules peut être minimisée en modifiant les paramètres de fonctionnement et de conception tels que la distance entre l'anode et la cathode (ACD), la densité de courant et les caractéristiques de la membrane. Une augmentation de la densité de courant et et de l'ACD conduit à une augmentation de la tension de la cellule, c'est-à-dire de la consommation d'énergie. De plus, l'utilisation d'un

petit diaphragme poreux situé loin de l'anode diminue la consommation d'énergie des cellules jusqu'à 40%. De plus, dans la configuration expérimentale, la longueur de l'anode est presque la moitié de celle de la cathode. Les résultats de la simulation pour la cellule sans diaphragme suggèrent que la consommation d'énergie de la cellule est inférieure lorsque la longueur de l'anode est plus grande, sa zone active et sa durée de vie étant plus grande dans ce cas. Pour chaque type de cellules, le meilleur cas simulé pour diminuer la consommation d'énergie et la chute de tension a été introduit.

Les résultats du présent travail de recherche étendent les connaissances sur le transfert de masse à l'intérieur de la cellule d'électrolyse au lithium. De plus, le solveur OpenFOAM développé peut être implémenté pour la simulation de différentes cellules d'électrolyse.

Mots clés: Cellule d’électrolyse du lithium, Modélisation mathématique, Écoulement à deux phases, Réactions électrochimiques, Distribution de courant tertiaire, Transfert de masse multicomposante.

Abstract

This thesis presents an investigation on the mass transfer and energy consumption inside a lithium electrolysis cell, the last step of lithium production process. Due to the harsh environment (high temperature and existence of corrosive materials), obtaining experimental data in such a cell is very difficult. However, the numerical analysis can help overcome the lack of knowledge. The complexity of coupled equations to solve different fields (concentration, electric and momentum fields) and electrochemical reactions are an obstacle for the development of a trustworthy model. According to the author's knowledge, except the publications presented in this thesis, no other study has already been published on the numerical analysis of aforementioned phenomena in a lithium cell. All of which represent the originality of the present thesis.

Mass transfer, velocity and voltage distribution have been simulated inside two types of lithium cell: cell with a diaphragm and diaphragmless cell. Simulations are performed using a commercial software, COMSOL®, and through a code developed with an open access toolbox, OpenFOAM. The benchmark cases have been simulated based on the geometry and conditions of an experimental bench designed and operated at Hydro-Québec. Comparing the experimental and simulation results for the electric field confirm the validity of the model. Moreover, the published experimental and simulation results of the flow field in a magnesium cell, which has similar conditions as lithium cell, have been used for the validation of the one and two-phase flow models.

For each type of lithium cells, the results for the velocity, electric and concentration fields are introduced in separated sections. The results show that the cell energy consumption can be minimized by changing the operating and design parameters such as anode-cathode distance (ACD), current density and diaphragm characteristics. Increasing the current density and ACD lead to an increase of the cell voltage. i.e., energy consumption. Moreover, using a small, porous diaphragm located far from anode decreases the cell energy consumption up to 40%. Furthermore, in the experimental setup, the anode length is almost half of cathode length. The simulation results for the diaphragmless cell with a longer anode suggest that the cell's energy consumption is lower, the active area is larger

and electrodes lifetime is higher. For each type of cells, the best-simulated case to decrease the energy consumption and voltage drop has been introduced.

The results of the present research work extend the knowledge about the mass transfer inside the lithium electrolysis cell. Moreover, the developed OpenFOAM solver can be implemented for the simulation of different electrolysis cells.

Keywords: Lithium electrolysis cell, Mathematical modelling, Two-phase flow, Electrochemical reactions, Tertiary current distribution, Multicomponent mass transfer.

Acknowledgments

Having a great supervisor, I am more interested in research now than the time I started my PhD. Thank you Prof. ***Désilets*** for your support, leadership and friendship.

" What do you need for your project?" Dr. ***Lantagne*** told me in our first meeting. I will always remember you as a humble man from industry who really want to help. Please accept my appreciation.

I would like to also express my gratitude to Prof. ***Proulx*** for his valuable advices and for bringing Giuliana and Camila in my world.

"Challenge is accepted" ***Giuliana***`s sentence, I am trying to use it in my life. Beside the friendship, in our collaboration we were like two peace of puzzle, completing each other. My friend, "Life is a beautiful ride", thank you for riding part of it with me.

I lovely thank my man, ***Suren***, who has been believing, encouraging, and helping me for being better and better.

I am also grateful of surrounding by nice ***friends*** and ***colleagues***.

Finally yet importantly, I cannot thank my ***family*** enough: my parents, my sister, my brother-in-law and my brothers, for supporting me spiritually throughout my PhD and my life in general.

Table of Contents

List of Figures

List of Tables

1 Introduction

1.1 Lithium properties, applications and resources

Lithium is among alkali metals in the first group of the periodic table. It is highly reactive and flammable therefore, lithium cannot exist freely in nature and it should be kept in mineral oil. Lithium is the lightest metal under standard state conditions while its density (534 kg/m^3) is almost half of water density. The importance of lithium has been recognized during Word War I when it was used for lightening aluminum alloys and for hardening lead alloys. Nowadays, lithium is mainly used for the fabrication of rechargeable batteries and ceramics, thus the need for lithium specially in batteries is increasing sharply [1].

brine and spodumene ($LiAlSi_2O_6$) are the main sources for the production of lithium, at present [2]. Table 1-1 presents the world lithium resources. Canada is one of the top 10 countries with largest lithium resources. To meet the demand for lithium markets, the increase of lithium production is inevitable. Improvements in the industrial production process, which is the goal of present research work, will have a noticeable effect on country's economy.

Table 1-1 World lithium resources, 2017 [3]

Countries	Resources/ millions tons	Countries	Resources/ million tons
Argentina	9	Australia	More than 2
Bolivia	9	Canada	2
Chile	More than 7.5	Congo, Russia and Serbia	1 each
China	7	Brazil and Mexico	0.2 each
United States	6.9	Austria and Zimbabwe	0.1 each

There are many different processing steps to extract lithium from its resources, detailed explanations can be found in the research of Wietelmann [2] and Tran [4] . The present thesis focuses on the last step of lithium production process: the electrolysis of LiCl. The electrolyte used in such lithium production cell is an eutectic mixture of 60% LiCl and 40% KCl. The KCl is added to the LiCl for two main reasons:

1. To decrease the melting point of the electrolyte. In fact, this composition shows minimum melting point among all other compositions, 353 °C, while pure LiCl melts at 610°C.
2. To increase the electrolyte conductivity [5].

All of which decrease the cell energy consumption. Therefore, the electrolyte contains three ions: two cations Li^+, K^+ and an anion, Cl^-. The lithium ions are reduced at the cathode and chloride ions are oxidized at the anode. Consequently, molten metallic lithium and gaseous chlorine are produced at the surface of the cathode and anode, respectively, through the general reaction:

$$\mathrm{LiCl\ (liquid)} \rightarrow \mathrm{Li\ (liquid)} + \mathrm{Cl_2\ (gas)}$$

Aforementioned explanations have been visualized through Fig 1-1, which shows the simplified schematic of lithium electrolysis cell.

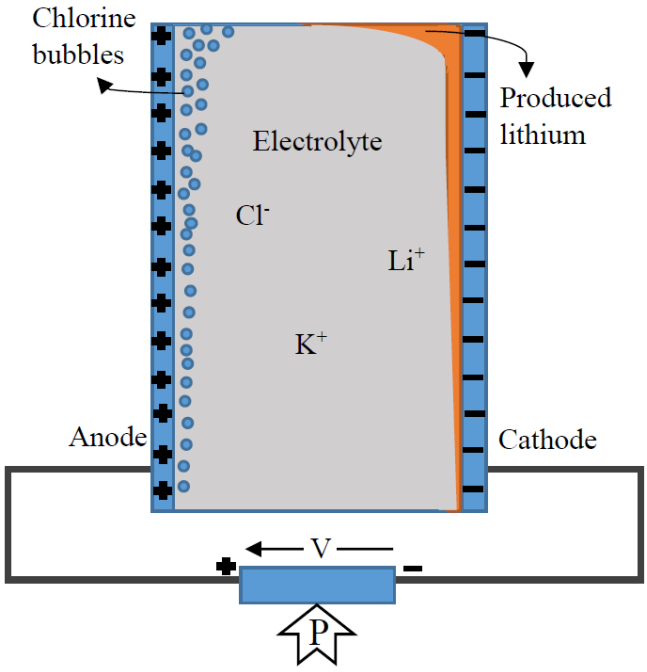

Fig 1-1 A simplified schematic of interpolar section of lithium electrolysis cell

The two products are lighter than the electrolyte, and they move to the top of the cell. During the electrolysis process, some part of the produced lithium can be lost by one of the following mechanisms: firstly, the metallic lithium that is accumulated at the top can be dissolved back in the electrolyte. Secondly, the accumulated lithium can back react with chlorine gas, on the top of electrolyte. Finally, some part of metal is lost in the electrolyte when the produced lithium flux to the anode or chlorine flux to the cathode and reacts back to LiCl. The solutions to decrease the metal losses are a faster removal of lithium from the reaction zone or separating the anodic and cathodic part of the cell by a diaphragm. Based on these two solutions, different lithium cells can be categorized as: cells with a diaphragm and diaphragmless cells. In the present research work, mass transfer in both types of cell has been investigated.

In fact, liquid lithium is formed on the surface of cathode, which is typically made of stainless steel. Lithium has the ability to wet stainless steel. Lithium deposition is affected by two forces: buoyancy which causes an upward movement of lithium and second, surface force between lithium and stainless steel. The second one tends to keep lithium at the surface. When the layer of lithium on stainless steel is thin, the surface force can overcome the buoyancy force. However, if the deposited layer becomes thicker, lithium could form droplets [6]. In this research work, the produced lithium is assumed to be a thin layer at the surface of the cathode, therefore, its effect on mass transfer has been neglected.

On the other side of the cell, the upward velocity of the chlorine bubbles, due to the strong buoyancy force, accelerates rapidly and introduce turbulence in the electrolyte. In fact, the bubbles transfer momentum to the electrolyte and cause the electrolyte circulation. The intensity of the circulation depends on the bubbles production rate, while the distribution of bubbles depends on the anodic current density distribution. In this research work, the anodic current density is high enough to induce a turbulent flow in the electrolyte, the electrolyte turbulent intensity being more than 5%. This effect of the bubbles on flow field results in uniform ions distribution in the electrolyte and a sharp decrease of the cell potential. On the other hand, the bubbles inside the electrolyte and at the surface of the anode block the path of ions and increase the electric resistivity; therefore, increase the cell potential. Changes in the cell voltage affect the current distribution at the surface of electrolyte, which gives the bubbles distribution at the anode.

Furthermore, the bubbles also influence the current efficiency when they react back with the produced lithium.

Aforementioned effects of the bubbles on concentration, electric and flow fields present some of the challenges related to the coupling between these fields. Moreover, the concentration and electric fields are linked through the ions or charge transfer and heterogeneous reactions. In reality, temperature field is also coupled with aforementioned fields inside the electrolysis cell. However, in the present research work, the lithium electrolysis cell is assumed to be isothermal.

1.2 Research project description

Sharp growth of lithium applications shows the importance of the production process efficiency and further necessities for its analysis and optimization. The lithium-chloride electrolysis is the main industrial process for lithium production. Therefore, from technical and economical points of view, an analysis and optimization of the functional parameters of the lithium production cell are important. According to author's knowledge, except the publication of the author and her coworkers, no study has been published on the simulation of mass transfer inside a lithium electrochemical cell. Therefore, the numerical simulation and analysis of mass transfer in the lithium cell is an original research subject that can be beneficial to overcome the lack of scientific knowledge in this field. In addition, the research results are a good foundation for the study of the mass transfer in the electrolysis of light metal halides in molten salt baths.

The complexity of the simulation of mass transfer in the lithium electrolysis cell resulted from the intimate coupling between concentration, electric and flow fields. Furthermore, the experimental analysis of mass transfer inside the molten salt electrolysis cell is extremely difficult due to high temperature and corrosive environment. This research will provides valuable information to understand the motion of species in the cell, and their effect on the important functional parameters of the cell such as cell voltage and energy consumption.

1.3 Objectives

In this project, the general objective is the introduction of a cell design for production of lithium with lower energy consumption. This ultimate objective has been reached step by step from primary to the tertiary objectives.

1.3.1 Primary objective

The primary objective is to develop a model of mass transfer inside lithium electrolytic cell. This model provides us with the concentration profiles of different ions in the cell. The ions concentration is affected noticeably by momentum transfer, kinetics and current density distribution at the electrodes. Consequently, modelling of the current density and voltage distribution is essential for the defined goal. Furthermore, the calculated velocity profile of electrolyte from momentum equations is another preliminary step.

Moreover, the effect of bubbles on the current, momentum and ions distribution and the effect of heterogeneous reactions on current and concentration distribution has been considered.

1.3.2 Secondary objective

After having reached an integrated model of the concentration distribution, the model has to be validated. In this work, the model has been used to simulate the only lithium cell for which experimental measurements were available[7]. The comparison between the electric field of the simulated case, named the base case, with that of experimental cell confirms the validity of the model. Moreover, the work of Liu et al. has been used to validate the flow field [8]. these authors determined the velocity distribution inside a cold model, using a particle image velocimetry (PIV) technique. Their cold model had the same geometry as a typical magnesium cell; the setup is presented in Fig 1-2 . Air is injected from porous glass plate into the water, to represent the bubbles that evolve at the anode. They compare their two-phase flow simulation results with the water velocity distribution measured with their experimental setup.

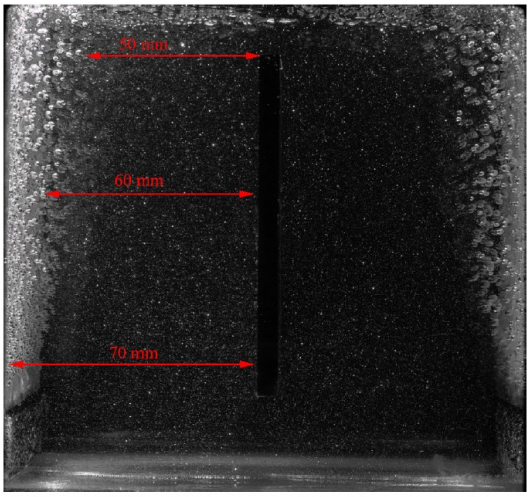

Fig 1-2 Cold model, Liu et al., 2015

1.3.3 Tertiary objective

For the last objective, the effect of the following important parameters on the cell voltage, i.e. cell energy consumption, has been considered.

- geometric design parameters: Anode-cathode distance (ACD), anode height, anode-diaphragm distance (ADD), diaphragm length and porosity
- operating parameters: current density

1.4 Study plan

When the project was started, there was no publication about the lithium electrolysis cell, except for patents. In patents, the effect of different designs and operating parameters on energy consumption and current efficiency have been mentioned. However, such documents do not provide any detailed information about mass transfer and chemo-physical phenomena inside the lithium electrolysis cell. Therefore, the necessary information for the simulation of lithium cell has been collected through:

1. Use of handbooks and software such as FactSage;
2. Published data for other electrolysis cells having operating conditions close to lithium cell

3. Like any other research activities, searching, googling, reading books and talking with experts.

In the next chapter, the state of the art about the lithium electrolysis cell has been introduced. Then, the published literature on the simulation of magnesium electrolysis cells, which are similar to lithium production cell, have been reviewed.

When the available information about the mass transfer in the cell is scarce, a strong commercial software like COMSOL® can ease the solution of complex equations. Therefore, the existing tertiary current density interface has been developed by adding some equations, defining dependent parameters such as electrolyte conductivity, and it has been coupled with turbulent flow interface in COMSOL®. After validation, the effect of diaphragm, ACD and current density on the mass transfer and cell voltage has been investigated. The results have been published as a journal paper, presented in chapter three [9].

The results from chapter three show that the diaphragm has noticeable effect on cell voltage. This motivate us to assess the effect of the diaphragm length, position and porosity on the cell energy consumption. The results of this investigation are given in chapter four [10]. In fact, the geometry and operating parameter used for the simulation of the lithium cell in chapter four is the same as those in chapter three.

The aforementioned parts of the work give us better insight into the different phenomena happening in the lithium cell. Therefore, for the next step, a new solver using an open access toolbox, OpenFOAM, has been developed. The solver was validated by comparing the results of this new model with COMSOL® results for a cell without diaphragm, as given in the chapter three. Due to the successful collaboration with Dr. Litrico, two papers, one with standard cell [11] and another with gas-lift cell was submitted in two well-known journals, Jurnal of Fluid Flow, Heat Mass Transfer, and Electrochemica Acta, respectively. The results for mass transfer and energy consumption in gas-lift cell can be seen in chapter five [12]. It is worth to mention that the new solver can be used for analysis of mass, momentum and electric field inside different cells.

Finally, the conclusion of the present research work, and the suggestions for future works have been proposed in chapter six.

2 State of the art

Every electrolysis cell is representedby six fields, including: electric, flow, concentration, temperature, stress and magnetic fields [13].

Electric field introduces a force on the ions and push them to move toward the opposite electrode. The flow field introduces the general patern of ions movement. Concentration field defines mass transfer for each ion through coupling with flow and electric fields. Temperature field is obtained through energy balance and it affects the electrolyte properties. Stress field is applied for the electrodes if they experience deformation. Magnetic field is produced by the moving ions and charges.

As mentioned before, the present thesis is considering mass transfer inside a lithium cell through the simulation of electric, flow and concentration fields. In fact, since the cell is considered isothermal, the effects of the temperature field on the energy consumption and mass transfer has not been taken into account. The electrolyte being considered as an incompressible fluid, the effects of stress is negligible. Moreover, Magnetic forces can be neglected since the current intensity of the application studied is low enough.

2.1 A review on the simulation of molten salt electrolysis cells

Table 2-1 presents a brief review for the simulation of different fields inside molten salt electrolysis cell representing the synthesis of: Aluminum (Al), Magnesium (Mg), Sodium (Na) and Lithium (Li).

The fields that are considered in each article are identified by black bullets in Table 2-1. In addition, a brief explanation has been given below the table. It worth to mention that the only published article about the lithium electrolysis cell which is not included in this thesis has been reviewed in this section. A more extended review about the simulation of the magnesium electrolysis cell has been covered in the section 2.2. In section 2.3, different lithium electrolysis cell designs are categorised into two groups, cell with and without diaphragm, and the patents related to each group have been presented.

Table 2-1 Modeling studies of molten salt electrolysis cell

Paper	Cell for production of	Dimension	Electric field	Temp. field	Flow field	Conce. field	Stress field	Magnetic field
Dupuis et al. 2004, 2005[14,15]	Al	3D	●	●				●
Severo et al. 2005[16]	Al	3D	●		●			●
Safa et al. 2005, 2008 [17,18]	Al	3D	●	●	●			●
Bojarevics et al. 2006 [19]	Al	3D	●		●			●
Sun et al. 2009[20]	Mg	3D	●		●			
Flueck et al. 2010 [21]	Al	3D	●		●			●
Sun et al. 2010[22]	Mg	3D	●		●			●
Sun et al. 2011[23]	Mg	3D	●		●			
Marceau et al. 2011 [24]	Al	3D	●	●			●	
Zhongxing et al. 2012 [25]	Na	3D	●					
Liu et al. 2014 [26]	Mg	3D	●	●				
Ariana et al. 2014 [27]	Al	3D	●			●		
Liu et al. 2015 [8]	Mg	2D			●			
Sun et al. 2015 [13]	Mg	3D	●					
Zhang et al. 2015 [28]	Al	1D		●	●			
Bardet et al. 2016 [29]	Al	2D		●	●	●		●
Li et al., 2017 [30]	Li Na	3D			●			
Oliaii et al. 2017 [9]	Li	2D-axi	●		●	●		
Oliaii et al. 2018 [12]	Li	2D-axi	●		●	●		
Litrico et al. 2018 [11]	Li	2D-axi	●		●	●		

Dupuis et al. considered the coupling between thermal and electric fields for the simulation of aluminium electrolysis cells [14,15].

Severo et al. developed a magneto-hydrodynamic (MHD) model for the 3-D simulation of the steady-state and transient MHD flow inside aluminium cell [16].

Bojarevics et al. considered the effect of current distribution on MHD through a time dependent model [19]. In their simulation of electromagnetic field, the whole busbar circuit and ferromagnetic effects are taken into account.

In the works of Safa et al., the coupling between the temperature field and magnetohydrodynamic effects inside aluminum cell has been described through a numerical approximation [17,18].

Flueck et al. developed a code named ALUCELL which is used to simulate magnetic, electric and flow fields inside aluminum cell [21].

The coupling between stress, electric and temperature fields inside the aluminium cell has been studied by Marceau et al. [24].

The electric field inside sodium electrolysis cell has been simulated by Zhongxing [25].

Ariana et al. considered the mass transfer inside aluminium cell through the simulation of electric and concentration fields [27].

A thermochemical model has been developed by Zhang et al. to simulate the temperature evolution, chemical composition and temperature distribution inside aluminum cell [28].

Bardet et al developed a 3D model for the simulation of the electric, flow, concentration and magnetic fields inside aluminium cell [29].

Except from the patents and papers presented in this thesis, the only articles about the lithium electrolysis cell has been published by Li et al. [20] and Litrico et al [11]. They simulated the three-phase flow field in the Down's cell for production of both lithium and sodium. In Down's cell, the products are removed form the electrolysis cell, therefore they do not accumulated at the electrolyte surface. In their model, large number of bubbles and drops are tracked in the Lagrangian modeling frame. They concluded that:

- ✓ Since the current density is fixed, i.e. the chlorine production rate is constant, smaller bubble's diameter results in higher mass flow rate because the number of produced bubbles is higher.
- ✓ Smaller lithium drops stay longer in the electrolyte cell.

- ✓ A part of the produced lithium reaching the electrolyte surface is accumulated at the rear of the cell where it is collected and removed from the electrolysis cell.
- ✓ The use of diaphragm is essential for the sodium production cell, otherwise, sodium reacts back with chlorine bubbles. However, the diaphragm can be removed from the lithium electrolysis cell because, as mentioned in the previous chapter, lithium can stick and form a thin layer at the cathode surface.

Although, Li et al. presented some valuable results about the flow field in the Down's cell for the lithium production, they have not taken into account the intimate coupling between electric and flow fields and heterogeneous reactions. Moreover, their work does not provide any information about the cell energy consumption and ions transfer. All of which have been considered in the present work.

Litrico et al. used and developed a code on OpenFOAM for the simulation of lithium electrolysis cell. They considered the strong coupling between electric, flow and concentration fields for the simulation of a lithium electrolysis cell. Their work bring a valuable information about the diffusion and migration flux of the ions inside the cell [11].

2.2 A review on the electrolysis cell for production of magnesium

The lack of published literature about the lithium electrolysis cell pushes the author to consider the electrolysis production of other materials in molten salt electrolytes. There should be some similarities between the electrolysis of those and lithium. Electrochemical cell for the production of magnesium is a good choice. Magnesium, like lithium, is lighter than electrolyte and goes up to the surface of electrolyte. Moreover, it participates in the back reaction with chloride gas produced at the anode.

Magnesium cell contains several parallel electrodes and a mixture of NaCl-$MgCl_2$ as the electrolyte. It works at 710 °C. Fig 2-1 shows the schematic of the magnesium electrolysis cell.

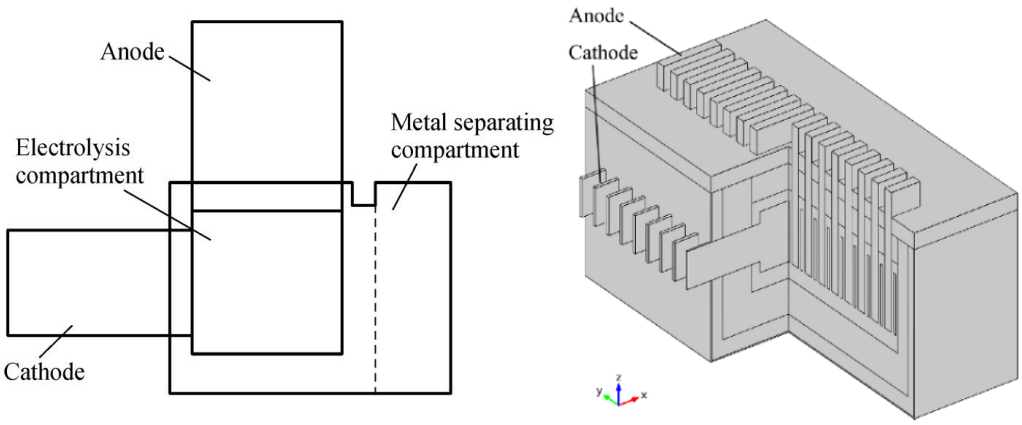

Fig 2-1. Schematic of magnesium electrolysis cell [8,13,26,31]

The analysis of different parameters on energy reduction for the magnesium cell has been done by Kannan and Desikan [32]. According to their results, the effect of the composition of electrolyte on current efficiency is more important than the distance between the electrodes, electrode height and electrolyte temperature. Moreover, minimizing the difference between the density of the electrolyte and molten metal could decrease the oxidation of metal by gaseous chlorine or atmospheric air. When the density of metal is close to the electrolyte, the metal will stay longer in the electrolyte before escaping at the upper surface. The suggested range of density difference between the electrolyte and the molten magnesium is 0.03-0.08 g cm^{-3} at the temperature of electrolyte.

Through experiments, Rao found that the current efficiency increases linearly when increasing the current density up to 0.7 A cm^{-2} and then it stays constant for current densities between 0.7-1.2 A cm^{-2}[33]. Increasing the current density more than 1.2 A cm^{-2} results in a decrease of the current efficiency.

The effect of the residence time of bubbles on the current efficiency in the electrolysis of magnesium has been considered by Demirci and Karakaya [34]. It is concluded that the diffusion of chlorine in electrolyte is the rate controlling step in the back reaction. Therefore, to improve the cell efficiency, one should try to remove chlorine gas faster and decrease the solubility of chlorine in electrolyte.

Sun et al. simulated the three-phase flow field of a magnesium electrolysis cell [20]. They added an electric field force as a source term in the momentum equation to consider the

effect of electric field on the flow field. This modification resulted in a higher electrolyte velocity. They built a physical model to validate their simulation. As it is the case in lithium cell, bubbles introduce a circulation inside the electrolyte of the magnesium electrolysis cell. They observed two main circulation regions in the cell. A part of the electrolyte moves the produced magnesium from the interpolar section to the collector. Another circulation pattern of the electrolyte increases the residence time of the produced magnesium in the electrolysis cell and therefore it increases the possibility of back reaction. In another research work, Sun et al. considered the Lorenz force as a momentum source in the momentum equation to see the effect of the electromagnetic field on the three-phase flow field [22]. They simulated the electromagnetic field by using Ansys 11.0 and coupled it by a user-defined function (UDF) to the three-phase flow field simulated by FLUENT6.3. A 2D two-phase flow model has been developed by Liu et al. and validated by comparing the model predictions with liquid velocity distribution obtained from their physical model [8]. They concluded that the non-uniformity in the distribution of the bubbles on the anode surface has to be taken into account in the simulation. Therefore, the anodic current density distribution from the thermoelectric model represents the boundary condition for the bubble's velocity and volume fraction at the anode. Their results show that higher current intensity leads to higher electrolyte velocity and gas volume fraction. Moreover, lowering the bubble's size decreases the electrolyte velocity (especially for the bubbles smaller than the critical size of 0.9 mm) and enhance bubble's volume fraction.

In another investigation, Liu et al. coupled a partial tracking method with a multi-physical model to evaluate the primary separation rate (PSR) of the magnesium drops [35]. Moreover, they considered the effects of some design and operating parameters on PSR of the magnesium droplets. Finally, the design of the cell has been optimized based on the improvement of PSR.

Sun et al. simulated the electric field in a magnesium cell by using a 3D numerical model. They concluded that the electrodes position and electrolyte height have significant effects on the cell ohmic drop. The optimum cell design with minimum ohmic drop has been obtained by the orthogonal design approach [31]. In another research, Sun et al. indicated that unlike current density, ACD and the height of interpolar section have significant effects on voltage drop [13]

Liu et al. considered the thermoelectric behaviour of a magnesium cell by using COMSOL. They introduced the linear relation between the dimensionless form of current intensity and that of some geometric parameters (ACD, electrodes thickness, anode width and number). They found that the effects of ACD on voltage drop and current density is much more important than the effects of electrodes' thickness. Moreover, since changing anode width alters the working areas, it affects the current density. In addition, increasing the number of anodes number increases the current in the magnesium cell directly [26].

2.3 Different designs for the lithium production cells

In Table 2-2, different patents for the LiCl electrolysis cell are classified in two categories.

Table 2-2 Patents for the lithium production cells based on electrolysis of LiCl.

Cell with diaphragm	Diaphragmless cell
Down, 1924 [36]	Grosbois et al., 1984 [37]
Kadija et al., 1979 [38]	Verdier et al., 1986 [39]
Bergmann et al., 2001 [40]	Muller et al., 1988 [41]
	Roux et al., 1988 [42]
	Christensen et al., 2002 [43]
	Nakamura et al., 2010 [44]

Down's cell is the first cell used for the production of lithium, see

Fig 2-2. In this cell, a cylindrical anode is surrounded by an iron cathode. A hydraulically permeable diaphragm is located between anode and cathode. Moreover, the products are collected in two different chambers [36].

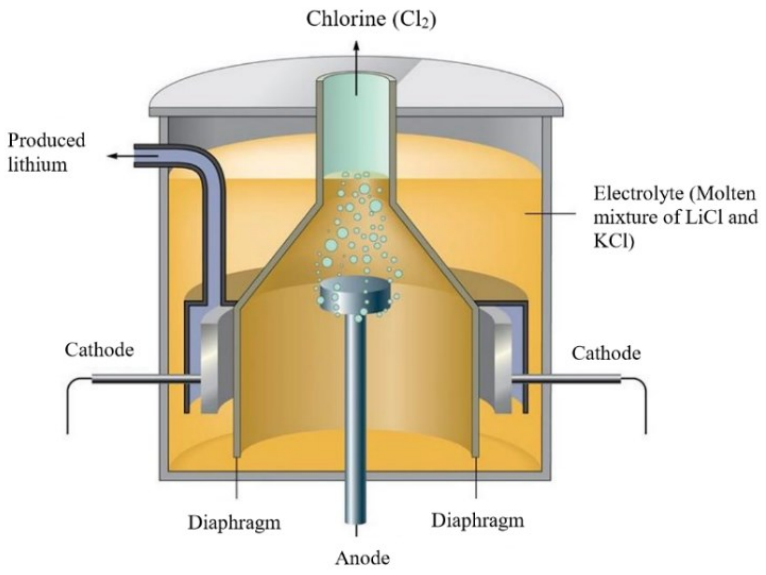

Fig 2-2 Schematic of Down's cell

The costs of maintaining and replacing the diaphragm are the main drawbacks for such designs. All of which are decreased by using a self-aligning diaphragm [19] or improving the quality of the diaphragm and consequently increasing its life time [38].

In 1984, Grosbois suggested a diaphragmless cell for the production of lithium, see Fig 2-3 [11]. In this cell, a cylindrical stainless steel cathode was located around graphite anode and below the surface of electrolyte. The cathode has a flared shape at the top to push the produced lithium toward the wall. To protect the anode from accumulated lithium at the surface of electrolyte, the top part of the anode is covered with an insulating refractory material. Verdier used the same design as Grosbois' cell and added another step to the process to separate the lithium and electrolyte outside of the cell, see Fig 2-4 [39]. In this cell, the electrolyte moves back to the cell continuously [39]. In Muller's cell, shown in Fig 2-5, the cathode is a straight cylinder surrounded by an annular zone that collects the produced lithium. A siphon pipe transfers the produced lithium from the annular zone to the separation chamber [41].

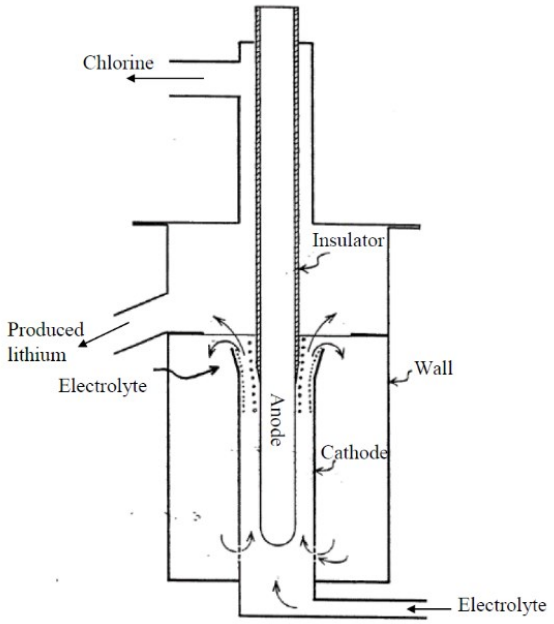

Fig 2-3 Schematic of Grosbois's cell [37]

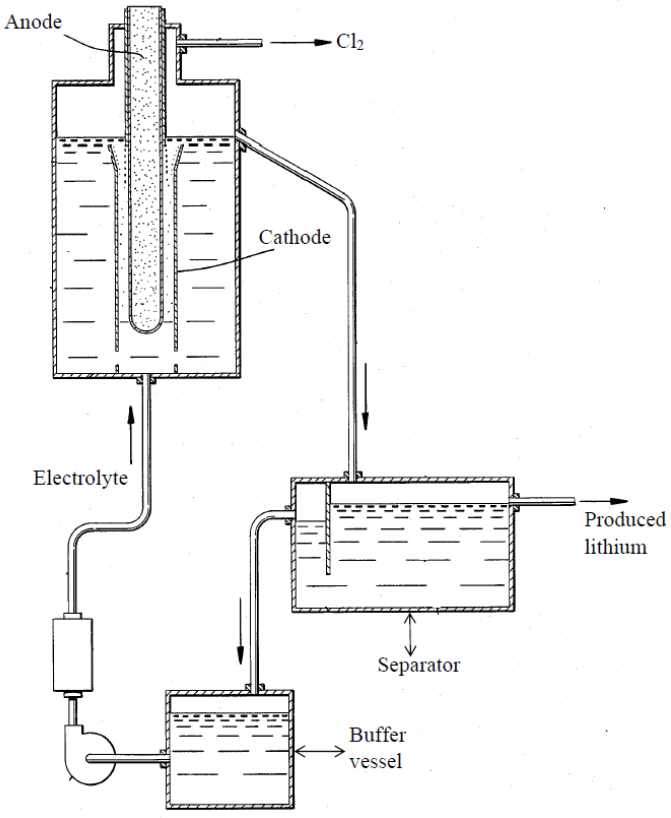

Fig 2-4 Schematic of Verdier's cell [39]

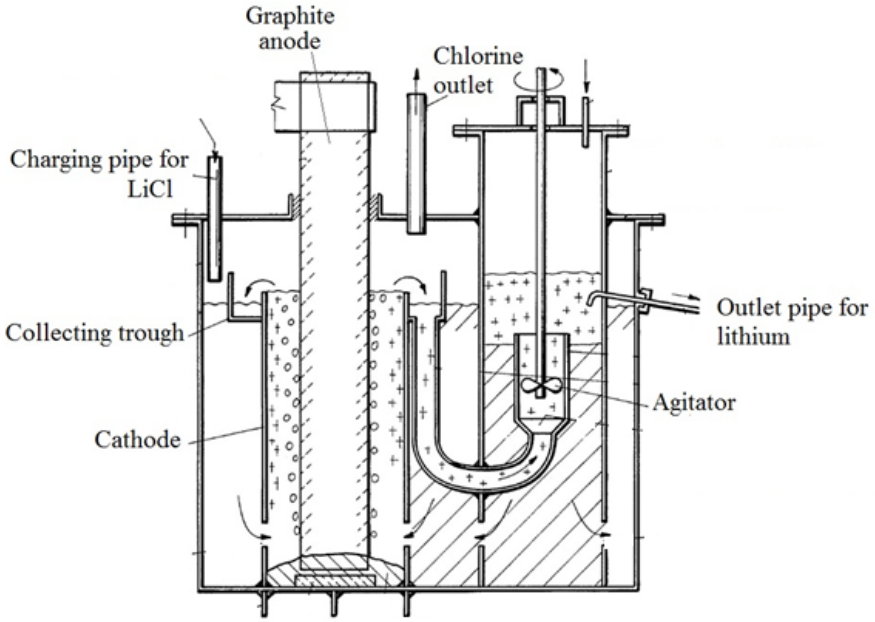

Fig 2-5 Schematic of Muller's cell [41]

As can be seen in Fig 2-6 , in Roux's cell, like other cells, the electrodes are coaxial cylinders and the anode is located in the center [42]. The distinguished feature of Roux's cell is that the cell's temperature is lower. Consequently, a layer of crystallized salts covers the internal wall, close to the electrolyte interface, where the chlorine gas has the highest temperature. In this way, they reduced the corrosion caused by the chlorine and improved the productivity of the cell.

Christensen's cell contains three interpolar electrodes located between anode and cathode encircling anode completely [43]. A hood removes the produced chlorine from the cell to a gas collection chamber and isolates it from produced metal.

Nakamura invented a safe and efficient method for the production of lithium [44], schematic of their cell can be seen in Fig 2-7. The produced chlorine gas from the electrolysis of LiCl is used to generate LiCl from Li_2CO_3 in a reactor located at the top of the cell. Then, the LiCl is fed to the cell as a raw material.

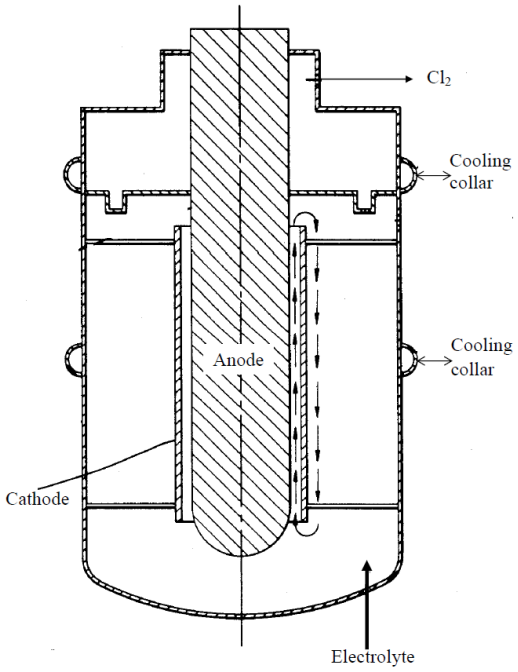

Fig 2-6 Schematic of Roux's cell [42]

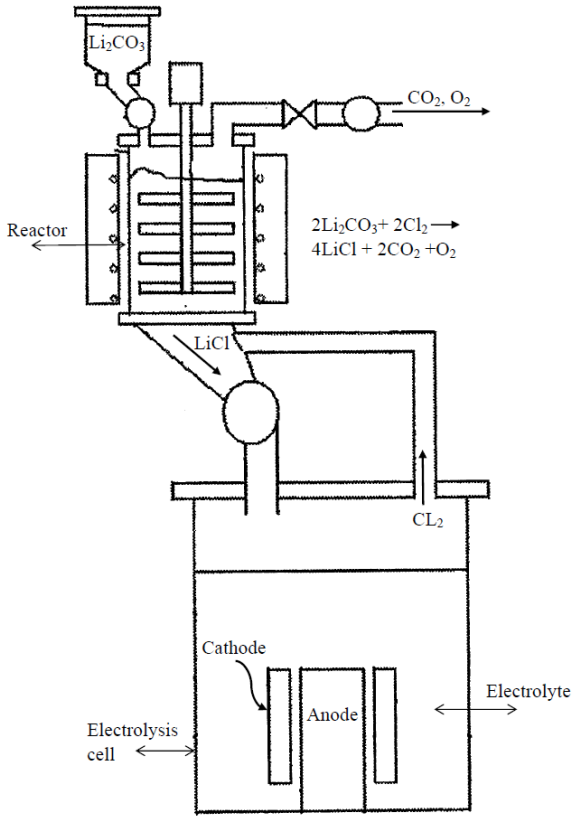

Fig 2-7 Schematic of Nakamura's cell [44]

CHAPITRE 3 : AVANT-PROPOS

Auteurs et affiliation:

- Elaheh Oliaii: étudiante au doctorat, Université de Sherbrooke, Faculté de génie, Département de génie chimique et de génie biotechnologique.
- Martin Désilets: professeur, Université de Sherbrooke, Faculté de génie, Département de génie chimique et de génie biotechnologique.
- Gaétan Lantagne: Directeur - Recherche et innovation, Hydro-Québec, Varennes, QC J3X-1S1, Canada

Date d'acceptation: 9 April 2017
État de l'acceptation: version finale publiée
Revue: Journal of Applied Electrochemistry

Référence: [9]

Titre français: Analyse numérique de l'influence des paramètres structuraux et d'opération sur le champ électrique et le profil de concentration dans une cellule d'électrolyse du lithium.

Contribution au document:

Ce premier article scientifique présente un premier modèle pour la simulation du transfert de masse à l'intérieur d'une cellule d'électrolyse du lithium. Le couplage intime entre les champs électrique, massique et de momentum y a été correctement pris en compte. L'écoulement est initié par une anode qui se déplace représentant de façon simplifiée l'influence de la production de bulles de Cl2 sur le mouvement de l'électrolyte. Les résultats présentés permettent d'améliorer la conception des cellules d'électrolyse en sels fondus et également de compléter les lacunes au niveau des connaissances scientifiques dans ce domaine.

Résumé français:

Un modèle intégrant le transfert de masse et les réactions électrochimiques dans une cellule d'électrolyse pour la production du lithium a été résolu en utilisant une méthode basée sur les éléments finis. Le couplage entre les transferts de momentum et de masse, la cinétique et la résolution du champ électrique a été pris en compte. L'écoulement turbulent résultant du dégagement des bulles générées à l'anode a été résolu en se basant sur un modèle k-ε. La surtension ohmique et l'hyperpolarisation causée par les bulles ont été représentées par une couche résistive et un paramètre de couverture à la surface de l'anode. De plus, les effets de la distance entre l'anode et la cathode (ACD) et de la densité de courant sur les champs électriques et massiques dans la cellule ont été simulés. Les résultats de la simulation transitoire ont montré que le diaphragme divise la cellule en 2 régions présentant des caractéristiques d'écoulement différentes : une première région entre l'anode et le diaphragme et une deuxième zone entre le diaphragme et la cathode. L'écoulement de bulles générées à l'anode a un impact important seulement dans la première région, où les gradients les plus importants sont retrouvés. La concentration des ions est uniforme dans la deuxième région. Tel qu'attendu, la densité de courant joue un rôle important dans l'électrocinétique de la cellule. Le changement de géométrie de la cellule, étudié en variant l'ACD ou en enlevant le diaphragme, a un impact important sur le potentiel de la cellule et sur la concentration des espèces électroactives près des électrodes. Le voltage de la cellule est réduit jusqu'à 40% quand le diaphragme est enlevé.

3 Numerical analysis of the effect of structural and operational parameters on electric and concentration fields of a lithium electrolysis cell

3.1 Graphic abstract

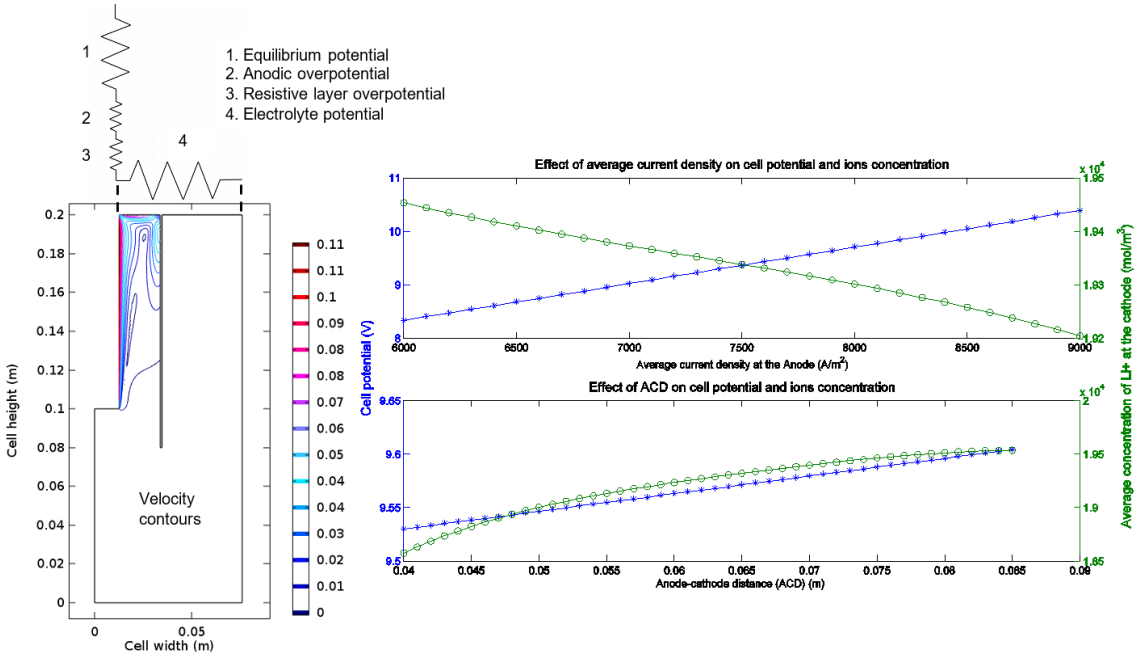

3.2 Abstract

A fully integrated mass transfer and electrochemical model of a lithium production cell solved using a finite element method is presented. The coupled effect of momentum and mass transfer, kinetics and electric fields is taken all into account. The turbulent flow resulting from the bubbles generated at the anode is solved based on a k-ϵ model. The ohmic overpotential and hyperpolarization due to the bubbles are considered through a resistive layer and bubble coverage at the surface of the anode. Furthermore, the effects of the anode-cathode distance (ACD) and current density on the electric and concentration fields of the cell are simulated. The results of the transient simulation reveal that the diaphragm separates the cell in two regions with different flow fields: a first region between the anode and the diaphragm and a second zone between the diaphragm and the cathode.

The flow of bubbles generated at the anode have an important impact only in the first region, where the most important gradients are found. The concentration of ions is uniform in the second region. As expected, the current density plays an important role in the electro-kinetic of the cell. The change in the geometry of the cell, studied by varying the ACD or by removing the diaphragm, has an important impact on the cell potential and on the concentration of electroactive species near the electrodes. The cell voltage is reduced by as much as 40% when the diaphragm is removed.

Keywords: Lithium electrochemical cell; mass transfer; turbulent flow; finite element model

3.3 Introduction

Lithium is the lightest metal in standard state conditions with a density (534 kg m^{-3}) almost half of that of water. This property of lithium makes it very useful for different industrial applications, such as in alloys for aircrafts, in electrodes for batteries, and ceramics composition.

Metallic lithium is typically produced by the electrolysis of LiCl, while this raw material results from the conversion of hard rock ore (like spodumene) or brine to carbonate, then to chloride .[36,39,41,44,45] According to the two half reactions below, the lithium electrolysis cell is specially designed to get two products that have a lower density than the electrolyte.

Cathodic reaction: $Li^+ + e^- \leftrightarrow Li(liquid)$

Anodic reaction: $Cl^- \leftrightarrow \frac{1}{2}Cl_2(gas) + e^-$

These two products can also react back, a situation that is controlled by using a separator as diaphragm between the anode and the cathode. Industrial production of metallic lithium is generated inside the so-called “Down cell” whose conception dates back to 1924, when C. D. James designed the first commercial electrolysis cell used for the production of sodium [36]. To avoid the main cell’s back reaction, in addition to using a diaphragm, he thought of keeping the freshly produced chemicals in separated chambers once extracted from the electrochemical reactor. Later, different cell designs were invented to improve the

purity of the produced lithium and to increase the current efficiency by prohibiting the back reactions inside the cell [39,41,42,44] However, none of these sources showed detailed information on what is happening inside the cell such as the distribution of species or the electrical potential.

According to the knowledge of the authors, no studies have been published on the simulation of such electrolysis process that considers the full coupling between mass, momentum and electrical charge transfer inside a lithium electrochemical cell. Therefore, the numerical simulation and the analysis of mass transfer inside a lithium production cell is an original subject of research that can be beneficial to improve the design of molten salts electrolysis cells and to overcome the lack of scientific knowledge in this field.

In addition, these results represent a good foundation for the study of mass transfer occurring during the electrolysis of other light metal halides in molten salt electrolytes. Mass transfer inside electrochemical cells is strongly affected by momentum and heat transfer, electrode kinetics, and electric fields in the cell. The coupling of these phenomena represents a major difficulty in cell modeling. Furthermore, high temperature, various number of corrosive species interacting inside the concentrated solutions, and the lack of knowledge of the electrolytic parameters surely add to the complexity of the problem.

This research is providing valuable information to understand the motion of various species in the cell, the effect of current density and anode/cathode distance (ACD) on the concentration and electric fields. Moreover the influence of a dense diaphragm- no porous flow nor ion-exchange mechanism-on mass transfer and energy consumption is presented. All simulations are conducted using COMSOL® a well-known commercial finite element simulation software.

3.4 Simulation

3.4.1 Methodology

In this study, an experimental lithium electrochemical cell is simulated as a one-phase flow. In fact, there are three phases present in the cell: the molten salt electrolyte, the liquid lithium produced at the cathode and the gaseous chlorine evolving at the anode. However, only the most important phase which is the electrolyte containing all ionic species is

considered in this research. All significant transport and kinetic phenomena have been considered, either inside the electrolyte or at the two electrode interfaces. The second phase, which is the highly conductive metallic lithium produced, sticks on the surface of the cathode and goes up with a negligible velocity. Hence, its effect on the electric and velocity fields could be ignored. The chloride bubbles in the 3rd phase increase the electrical resistivity of the cell and affect also the mass transport in the electrolyte. Moreover, the bubbles directly influence the chloride oxidation rate by blocking a part of the anode surface, which is then not available to the electrolysis. Furthermore, the effect of bubbles on the velocity and electric fields are simulated using a moving anode, and by considering a layer of higher electrical resistivity at the anode surface (see Electrode Equations section).

In industrial lithium production cells, a mixture of 60% LiCl, 40% KCl (molar basis) is used as the working electrolyte. The basic operating parameters shown in Table 3-1 and representing those of an experimental cell used to mimic the behaviour of industrial cells have been provided. The geometry of the experimental setup is shown in Fig 3-1[7]. The main properties for the electrolyte as well as for the electrochemical reactions are found in Table 3-2.

Table 3-1 Simulation parameters based on experimental data [7]

Initial concentration of K^+ (mol m^{-3})	10.8e3	Initial concentration of Li^+ (mol m^{-3})	19.2e3
Initial concentration of Cl^- (mol m^{-3})	30e3	Temperature (K)	723
Current (A)	60	Current density (A m^{-2})	7800

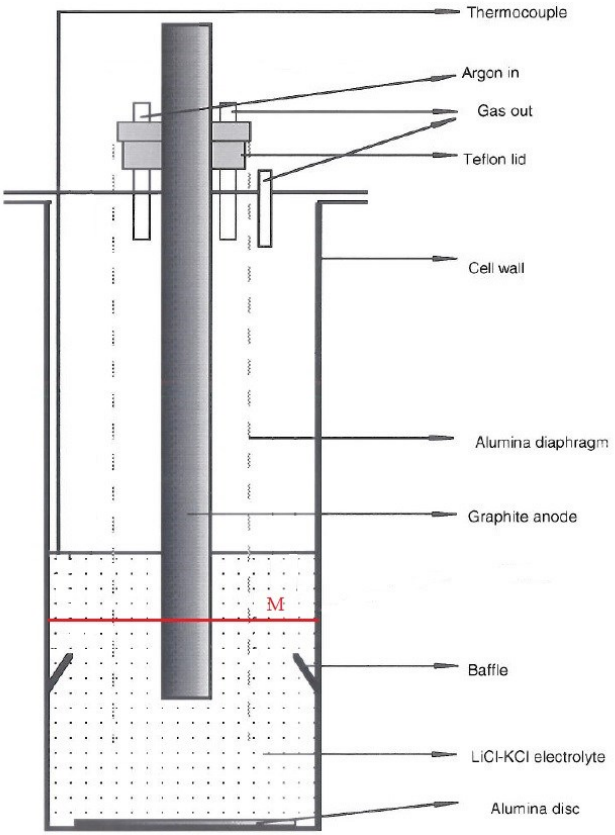

Fig 3-1 Schematic illustration of the experimental standard cell [7]

As mentioned in Table 3-1, a current of 60 A has been applied to the experimental setup. At the end of the experiment, the external voltage was measured at 10.8 V. This value is including all source of voltage drop between the two terminals of the power supply: kinetic, ohmic and transport overpotentials, voltage drop effect due to the high resistance of Cl_2 gaseous film formed at the surface of the anode, and voltage losses in external parts (like bus-bars, electrical connections). For the purpose of the simulation, external losses have been neglected. Considering the external voltage drops and the evolution of the cell voltage over time, the total initial voltage of the cell at the current density fixed during experiments (7800 A m^{-2}) has been estimated at 9.5 V. Accordingly, the energy requirement of the simulated cell is approximately 33.5 kWh kg^{-1} Li, which is reasonable when compared to typical values reported for industrial cells at around 30 kWh kg^{-1} Li [46]. Considering the nature of the experimental set-up as a lab-scale unit, the agreement between the energy density obtained industrially and at the lab-scale is considered reasonable.

The binary molecular diffusion coefficients for Li^+, Cl^- and K^+ at high temperatures have been measured by Janz and Bansal[47]. However, the binary diffusion coefficients reported in Table 3-2 have been estimated by extrapolating these measurements because our cell temperature falls outside of the experimental range considered by Janz and Bansal. The accuracy of these estimations is indirectly validated by comparing the electrolyte conductivity- estimated from equations 3-1, 3-3 and 3-7 below using these diffusion coefficients and initial ion concentrations- (209 S m^{-1}) with that of Van Artsdalen and Yaffe (157 S m^{-1}) [5].

Table 3-2 Properties of the electrolyte and kinetic parameters

Electrolyte density (kg m^{-3}) [48]	1648	Anodic and cathodic transfer coefficient	0.5
Anodic equilibrium potential (V)*	3.6	Electrolyte viscosity (Pa s) [49]	1.2e-3
Binary diffusion coefficient of Li^+ and Cl^- in LiCl (m^2 s^{-1})	3e-9	Cathodic equilibrium potential (V)[a]	0
Binary diffusion coefficient of Li^+ in KCL and K^+ in LiCl (m^2 s^{-1})	2e-9	Binary diffusion coefficient of Cl^- and K^+ in KCL (m^2 s^{-1})	1.5e-9

[a] In this simulation, the cathodic equilibrium potential is set to zero for convenience. Accordingly, the anodic equilibrium potential has been set to a value representing the difference between equilibrium potential of the oxidation of chloride and that of lithium reduction

3.4.2 General Equations

In our case, the molten bath is containing only ionic species. Ions are categorized into reacting and non-reacting species or supporting electrolyte. In reality, the electrolyte in lithium production cell is a concentrated solution. However, the lack of data for multicomponent diffusion coefficients and for the activity coefficients forces us to adopt an effective diffusion approach using the Wilke's correlation [50]:

$$D_{i,eff} = \frac{1-x_i}{\sum_{\substack{i=1 \\ i\neq j}} \frac{x_j}{D_{ij}}} \tag{3-1}$$

Where x_i and x_j are the mole fractions of ions and depend on the local concentration of ions in the cell.

The transport of ionic species inside an electrochemical cell consists of three mechanisms: convection, diffusion and migration. Taking into account these mechanisms, the flux N_i of each i species in an electrochemical cell is written by means of the Nernst-Planck equation as:

$$\mathbf{N_i} = c_i\mathbf{V} - D_{i,eff}\boldsymbol{\nabla}c_i - z_i F u_{m,i} c_i \boldsymbol{\nabla}\Phi \quad (3\text{-}2)$$

The ions mobility, $u_{m,i}$, is calculated through the Nernst-Einstein equation:

$$u_{m,i} = \frac{D_{i,eff}}{RT} \quad (3\text{-}3)$$

Applying the mass conservation law to each species, we finally get:

$$\frac{\partial c_i}{\partial t} = \boldsymbol{\nabla}.\mathbf{N_i} + R_i' \quad (3\text{-}4)$$

With

$$\sum_i z_i c_i = 0 \quad (3\text{-}5)$$

The term R_i' in Equation (3-4) represents the homogeneous reaction rate of each species in the bulk the value of which is set to zero in our case because only electrochemical reactions are considered. According to Equation (3-1) and (3-4) and considering the axisymmetric (2D) configuration of the electrochemical reactor modeled, there are N+4 unknown variables: concentration of species (N), electrical potential (1), velocity field (2) and pressure field (1). Equation (3-4) is written for n-1 species and the concentration of the last species is calculated by considering electroneutrality, given in Equation (3-5). The velocity and the pressure field is obtained from the solution of the Navier-Stokes equation. Finally, the electrical potential is obtained from the general electrolyte current conservation:

$$\boldsymbol{\nabla}.\left(-F\left(\boldsymbol{\nabla}\sum_i z_i D_{i,eff} c_i\right) - \sigma_l \boldsymbol{\nabla}\Phi_l\right) = 0 \quad (3\text{-}6)$$

Where σ_l is the electrolyte conductivity and it relates to the ions mobility through equation below:

$$\sigma_l = F^2 \sum_i z_i^2 u_{m,i} c_i \quad (3\text{-}7)$$

At the electrode surfaces, the flux N_i is zero for all electroinactive ions. For the electroactive ions, the flux is related to the current through Faraday's law.

As mentioned before, the velocity field is turbulent base on the calculation of Reynolds number (Re=2.8e4) in the zone between the anode and the diaphragm. As such, a turbulent diffusion coefficient is added to the effective molecular diffusion coefficient to consider the effect of eddy diffusivity on ions transfer. For most practical cases, the turbulent Schmidt number- defined as eddy viscosity/eddy diffusivity- is assumed to be equal to 1[50]. Consequently, the turbulent diffusion coefficient is estimated based on the turbulent kinematic viscosity resulting from the velocity field.

3.4.3 Electrodes Equations

The proper equations representing the current density at each electrode are selected based on systems representing molten salt electrolysis that have proven electrochemical similarities with Li electrolysis cells [27]. The cathode reaction is expressed by a linearized Butler-Volmer (B.V.) equation. It is a realistic assumption for representing an electrochemical reaction with a small overpotential, also known as low-polarization reaction [51]. In such a case:

$$i_{loc} = i_{0_c} \frac{F\eta}{RT} \tag{3-8}$$

On the other side of the cell, the heterogeneous reaction rate at the anode is expected to be slow. Consequently, the anodic kinetic overpotential is expected to be relatively high. Additionally, the bubbles create a hyperpolarization: in other words, a part of the overpotential is caused by gas bubbles occupying a certain proportion of the anode surface. The bubble coverage variable ($\emptyset_g$) is representing the fraction of the electrode surface covered by bubbles. As a matter of fact, only the rest of the electrode surface (1-$\emptyset_g$) is available for the electrochemical reaction. Although the bubbles are blocking the path of chloride ions towards the anode, the concentration gradient is quite low due to the concentrated electrolyte and the turbulent flow. As a result, the concentration overpotential is negligible. The equation below relates the current density to the anode overpotential and bubble coverage [52]:

$$i_{loc} = i_{0a}(1 - \emptyset_g)[exp\left\{\frac{\alpha_{O_a} F}{RT}\eta\right\}] \tag{3-9}$$

Where α_{O_a} is the transfer coefficient of the oxidation reaction at the anode taken to be 0.5. Also, according to the investigations of Vogt and Balzer in stagnant liquids, the bubble coverage is related to the current density and can tentatively be correlated by[53]:

$$\emptyset_g = 0.023\, i^{0.3} \tag{3-10}$$

The presence of bubbles also reduces the conductivity of the electrolyte layer near the anode. The shape and the thickness of the layer are estimated based on sound experimental results obtained with magnesium cells [8], an electrochemical system which has similar conditions (temperature, ions, current densities) as those found in a lithium production cell. The conductivity of this layer is calculated according to the following Bruggeman correction [52]:

$$\sigma_{mix} = \sigma_l\left(1 - \emptyset_g\right)^{1.5} \tag{3-11}$$

According to this equation, the conductivity of this layer depends on current density and concentration of ions as per Equation (3-7) and (3-10) above.

To solve Equations (3-8) and (3-9), the exchange current must be specified. Due to the lack of published information about the reaction rates at the electrodes of a lithium production cell, approximated exchange current densities have been indirectly obtained as follows.

The exchange current density is related to the ionic concentration and to the reaction rate by the following equation considering that the system is far from the limiting current condition and that the concentration at the electrode surface can reasonably be assumed as the bulk concentration. Equation 12 also implicitly considers the specific stoichiometry of the electrode reactions

$$i_0 = k_r F c^* \tag{3-12}$$

The measured reaction rate constant for sluggish reactions, like for our anodic reaction, is typically between 1e-9 and 1e-11 m s^{-1} [51]. As a result, i_{0_a} is in the order of 1, depending on the concentration of Cl^- in the bulk. At the cathode, the reaction rate constant is high enough so that the linearized B.V. equation can be used. Accordingly, the estimated i_{0_c} is in the order of 1000.

3.4.4 Simulation of the Velocity Field

One important aspect of this modeling work is that it takes into consideration the effect of the velocity field on the mass transfer inside the lithium cell. The two basic assumptions in this simulation are:

The anode is considered as an upward moving wall having the terminal velocity of the bubbles, u_t.

This velocity is calculated based on the work of Clift et al. [54]. The dimensionless numbers: Reynolds (Re), Eotvos (Eo) and Morton (M) are calculated with the help of the equations below:

$$\text{Re}=\rho u_T d_b/\mu \tag{3-13}$$

$$E_o = g\Delta\rho d_b^2/\gamma \tag{3-14}$$

$$M = g\mu^4\Delta\rho/\rho^2\gamma^3 \tag{3-15}$$

The estimation procedure starts with the selection of a mean bubble diameter. Based on Cl_2 bubbly flow at the anode of a magnesium production cell, operated in conditions very close to those found in a lithium cell, the range of bubble diameters is between 50 μm to 2 mm [8]. A diameter of 1.5 mm has been considered in this research. Then, the terminal velocity has been evaluated at 0.29 m s^{-1} from Re = f(Eo, M) relationships found in Figure 2.5 of Clift et al. [54]. The velocity field resulting from this bubble terminal velocity have been validated with the results obtained by Liu et al., (see section Validation of the Simulation Model, 3.4.8).

On the cathodic side, the metallic lithium produced is lighter that the electrolyte and consequently goes up at an estimated upward velocity of 1e-5 m s^{-1}, a very low value considered to have a negligible effect on the mass transport.

Furthermore, a standard k-ϵ approach is used to represent the turbulent nature of the flow through the solution of two additional variables: k, the turbulent kinetic energy and ϵ the rate of dissipation of kinetic energy [55].

The equation for the turbulent kinetic energy is:

$$\rho(V.\nabla)k = \nabla.\left[\left(\mu + \frac{\mu_T}{\sigma_k}\right)\nabla k\right] + P_k - \rho\epsilon \tag{3-16}$$

The equation for the rate of dissipation of kinetic energy is:

$$\rho(V.\nabla)\epsilon = \nabla.\left[\left(\mu + \frac{\mu_T}{\sigma_\epsilon}\right)\nabla\epsilon\right] + C_{\epsilon 1}\frac{\epsilon}{k}P_k - C_{\epsilon 2}\rho\frac{\epsilon^2}{k} \tag{3-17}$$

Where:

$$\mu_T = \rho C_\mu \frac{k^2}{\epsilon}, \quad P_k = \mu_T[\nabla V : (\nabla V + (\nabla V)^T)] \tag{3-18}$$

The constants used are described in Table 3-3.

Table 3-3 The constants of the standard k-ϵ approach

$C_{\epsilon 1}$	$C_{\epsilon 2}$	C_μ	σ_k	σ_ϵ
1.44	1.92	0.09	1	1.3

The impact of the other fields on the velocity has been neglected. Due to the constant velocity of the electrolyte entrained by the bubbles, represented here by the movement of the anode, the velocity field can be solved with a stationary solver. Finally, the resulting velocity field is used in the resolution of the electric and concentrations fields, which are solved with a time dependent solver.

3.4.5 Boundary Conditions

The geometry used in the simulation is 2D-axisymmetric as shown in Fig 3-2. All dimensions are in meter. The numbers used at the various boundaries are presented in Table 3-4, where the different conditions in velocity, electric and concentration fields are defined. It should be noticed that the cell diaphragm used in the experimental was a dense alumina tube, simulated as a wall in the model.

Table 3-4 Boundary conditions for velocity, electric and concentration fields

	Flow field B.C.	Electric field B.C.	Concentration field B.C.
1	V_r=0, V_z=u_t (moving wall)	i_m=7800 (A m^{-2})	-$n.N_i$=i_{loc}/F, for i_{loc} see Equation 9
2	V_r=0, V_z=0	i_m=7800 (A m^{-2})	-$n.N_i$=i_{loc}/F, for i_{loc} see Equation 9
3	dV_r/dr=0, dV_z/dr=0 (symmetry)	di_l/dr=0 (symmetry)	dN_i/dr=0 (symmetry)
4	V_r=0, V_z=0 (wall)	$i_f.n$=0, f=s,l (insulated)	-$n.N_i$=0
5	V_r=0, V_z=0 (wall)	Φ =0 (V)	-$n.N_i$=i_{loc}/F, for i_{loc} see Equation 8
6	V_r=0, V_z=0 (wall)	$i_f.n$=0, f=s,l (insulated)	-$n.N_i$=0
7	V_r=0, V_z=0 (wall)	$i_f.n$=0, f=s,l (insulated)	-$n.N_i$=0

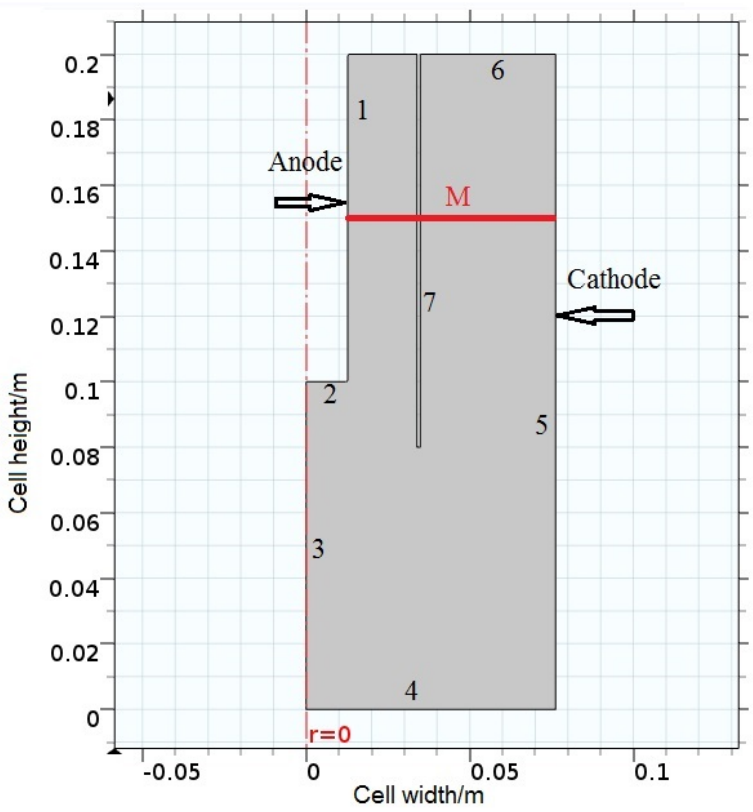

Fig 3-2 Geometry considered in all simulations

3.4.6 The problem solving process steps

The problem solving process steps are described in the diagram below:

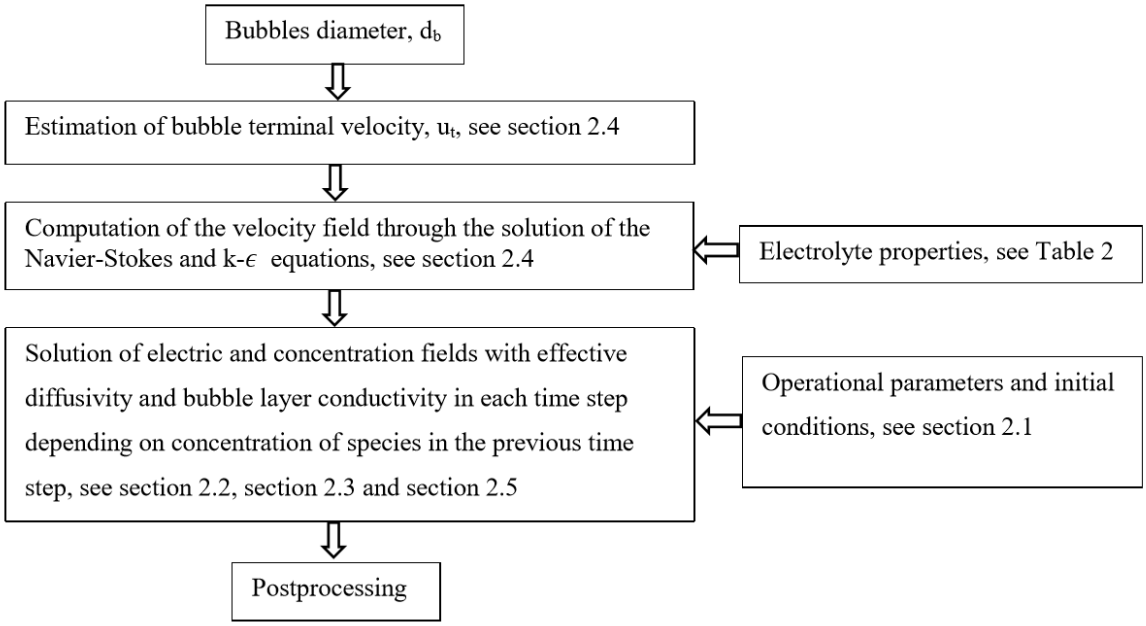

3.4.7 Mesh Independency

The mesh independency is checked to ensure the quality of the simulation results and to determine whether the decrease of mesh size influences the results or not. Structured (S) and unstructured (NS) meshes with different sizes have been tested. Because the gradients of concentration and the species mass fluxes are the largest near the electrodes, smaller meshes are used there. For unstructured mesh, triangular shaped elements are used while rectangular elements are used for structured mesh. With unstructured mesh, a thin layer (0.1 cm thickness) of structured boundary layer mesh has been considered normal to the surface of the electrode. The number of elements has been changed from 12000 to 35000 for both types of mesh. The mesh independency study shows that the main results such as overpotentials, cell potential, velocity and current are mesh independent when the number of elements is more than 25000. For instance, Fig 3-3 shows the electrolyte potential at the anode surface for 7 different sizes of mesh. The positive values shown on the y-axis represent the height of the anode while the negative values are located along the width of the anode, at the bottom and in the radius direction, from the corner to the center.

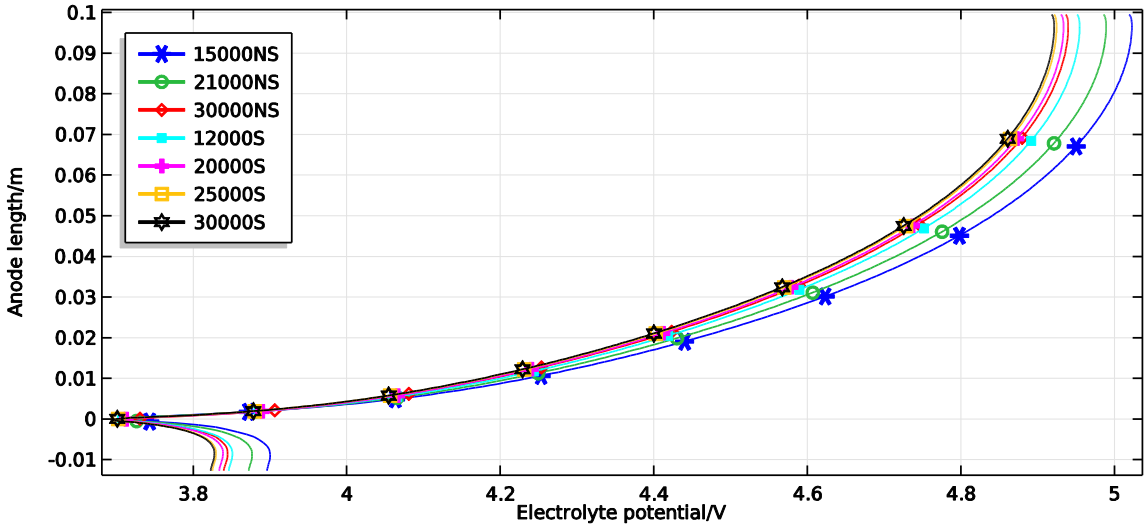

Fig 3-3 Study of mesh independency: impact of different mesh sizes on the simulation results, NS: non structured mesh, S: structured mesh

3.4.8 Validation of the Simulation Model

Due to the harsh conditions prevailing inside molten salt electrochemical cells, it is a challenging task to obtain trustworthy experimental data. Although there is no published studies done on lithium production cells to validate our numerical results, some data resulting from the experimental studies conducted at Hydro-Québec have been used to validate the results obtained in this numerical study[7]. The geometry and some of the operational parameters relevant to the simulation are taken directly from this report. In the setup, shown in Fig 3-1, an alumina tube is employed as a diaphragm to recover the metallic lithium produced at the cathode, formed by the stainless steel outer wall of the reactor. Lithium is then prevented from reacting with the chlorine gas evolving at the anode, taking the form of a graphite rod.

As mentioned before, the velocity field is simulated by considering a one-phase flow with a moving wall as the anode. In order to assess the impact of this simplification, the velocity field of a magnesium cell, operated with similar boundary conditions as the lithium production cell, is simulated. As shown in Fig 3-4, the validity of this simplification has been proven by comparing the results obtained from the simulation of a magnesium cell with such simplification to the experimental measurements and to the simulated two-phase flow obtained by Liu et al [8].

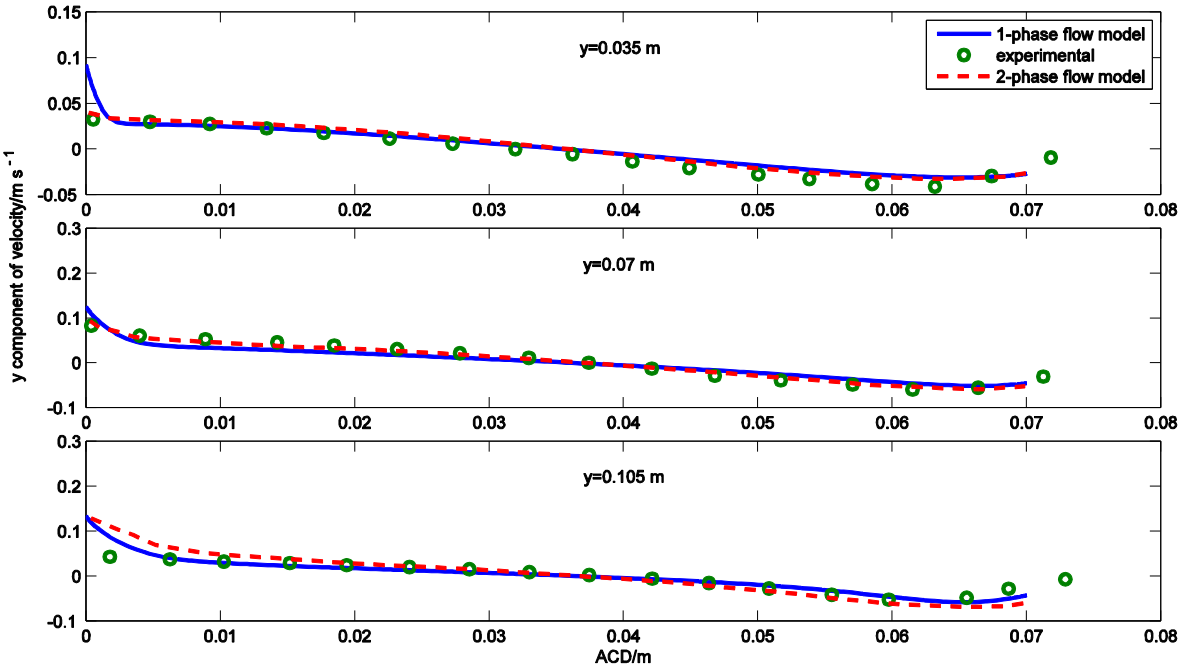

Fig 3-4 Resulting velocity field from a magnesium production cell: comparison between experimental, one-phase and two-phases flow simulations at different levels from the bottom of the cell

3.5 Results and Discussion

All the simulations are done in COMSOL® using a 2D-axisymmetric configuration and including multiphysics modeling. Level M, mentioned later in some results, is also shown in Fig 3-1 and Fig 3-2. It goes from the anode to the cathode at a vertical position of 0.15 m from the bottom of the cell. The ACD of the base case is 0.0635 m.

The maximum mesh size is 0.002 mm and the total number of degrees of freedom to be solved for the base case is 437185. The number of degrees of freedom includes:

- 102531for each of the electrolyte potential, concentration of Cl^- and Li^+
- 51732 for velocity field
- 25866 for each of the pressure, turbulent kinetic energy and turbulent dissipation rate
- 261 for potential drop over the bubble layer
- 1 for external electric potential

3.5.1 Results from a Base Case

As expected, the number of moles of active ions decreases linearly over time while that of inactive ions is maintained constant, thereby showing the mass conservativeness of the numeric solution as implied if Faraday's law is verified. Fig 3-5 presents the relative change in the number of moles for lithium, chloride and potassium ions. Due to the stoichiometry of the reaction, the rate of mole consumption for both lithium and chloride ions is the same. However, as the initial concentration of chloride ions is higher than that of lithium, the relative chlorine consumption is lower than that of lithium.

While the total amount of ions in a closed electrochemical cell with no supply is only affected by the electrochemical reactions, the local concentration of these charged species is under the influence of all transport phenomena such as diffusion, migration and convection as well as reactions at the electrode surfaces.

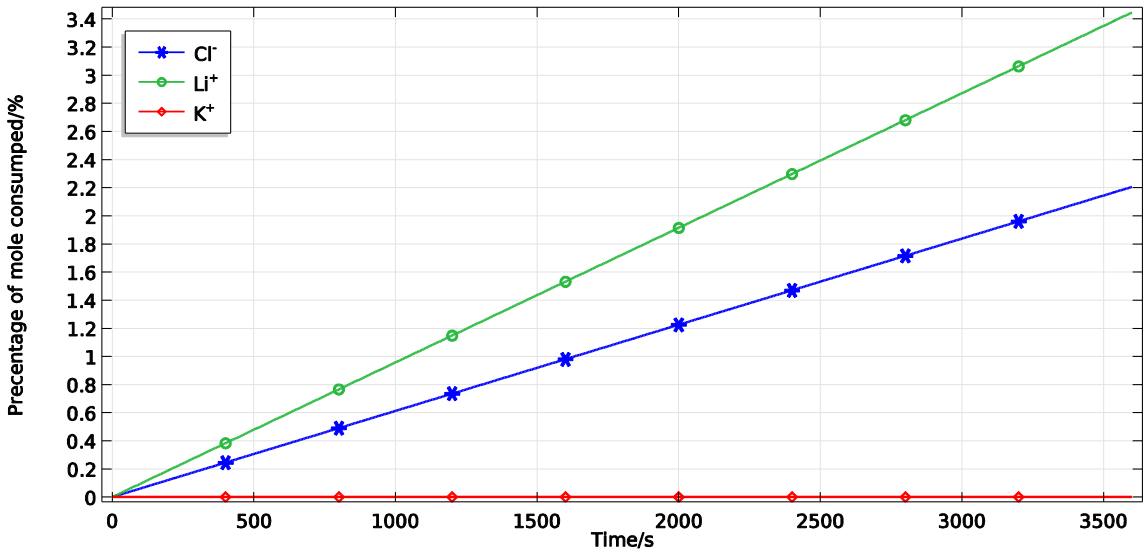

Fig 3-5 Percentage of mole consumed over time for different ions in the cell

Fig 3-6 shows the concentration difference relative to the initial concentration of ions at the level M after 1 h of simulation. The diaphragm, considered as a wall, separates the cell in two regions, one between the anode and the diaphragm and a second one from the diaphragm to the cathode. In region 1 at level M, the concentration of electroactive ions increases away from the anode and diaphragm. This behavior is due to the mass transport, to the flow pattern and to the electrochemical reactions at the anode. Bubbles induced flow is responsible for the circulation pattern between the anode and the diaphragm, which could

be seen in Fig 3-7a. More precisely, the migration pushes the cations away from the surface of the anode to the center where the global movement of ions is determined by the velocity field. In region 2 at level M, the ions concentration is slightly decreasing from the diaphragm to the cathode surface. It can be seen in Fig 3-6 that the difference relative to the initial concentration is higher in the first region mainly due to the fact that the second region contains more electrolyte, i.e. more mole of electroactive ions.

Furthermore, in the region near the anode, the chloride concentration is lower than that of the other ions because of the anodic reaction involving only chlorides. The same situation is prevailing in region 2 for the Li ions. Potassium ions move from the first region to the second one to maintain electroneutrality. This mass transport is essentially done by migration.

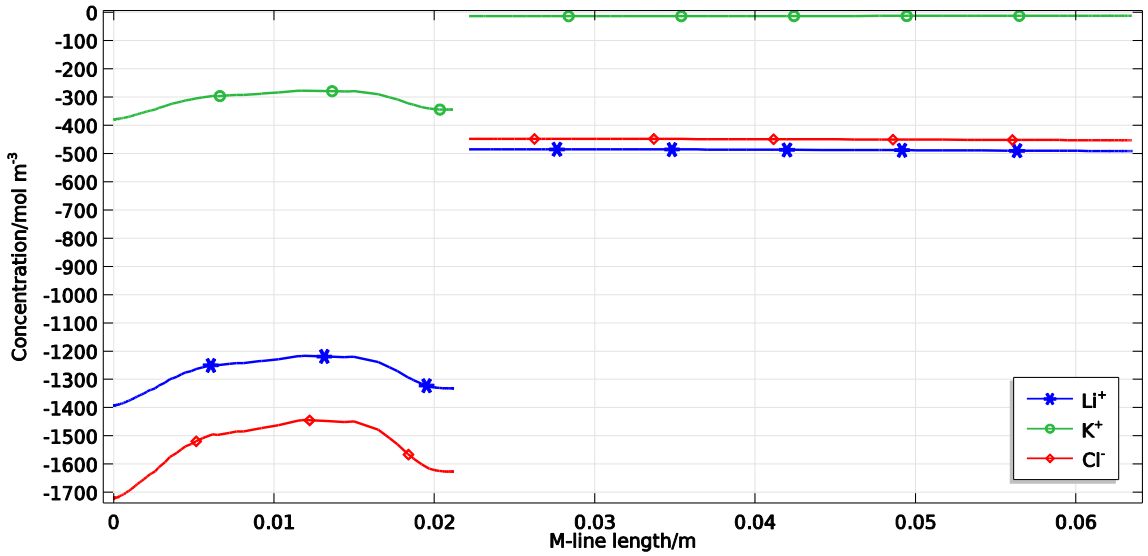

Fig 3-6 Difference between ions concentration after 1h and initial concentration of ions along the level M

3.5.2 Effect of the Diaphragm on the Velocity and Electric Fields

The effect of the presence of the diaphragm on the velocity field is shown in Fig 3-7. Even if the chlorine gas is not specifically taken into account in this simulation, the uplifting effect of Cl_2 bubbles simulated by a moving wall gives rise to the flow pattern seen in Fig 3-7b. In fact, the velocity contours show the possible entrainment of Cl_2 bubbles to the cathode and a fair possibility of a back reaction with the liquid lithium. This phenomenon could be the main reason for the low current efficiency of such processes. In some of the

patents related to Li electrolysis cells, new ways are proposed to break this circulation pattern or to limit the chlorine mass transfer to the cathode, in order to prevent the back reactions [39–41,56] . In this work, the diaphragm blocks the bubbles path from the anode to the cathode, see Fig 3-7a, and prohibits the back reaction thus increasing the current efficiency. On the other side, the diaphragm, being considered as an insulating wall, has an important drawback: it introduces an additional potential drop of 3.84 V, which causes an important increase in the specific energy consumption of the cell.

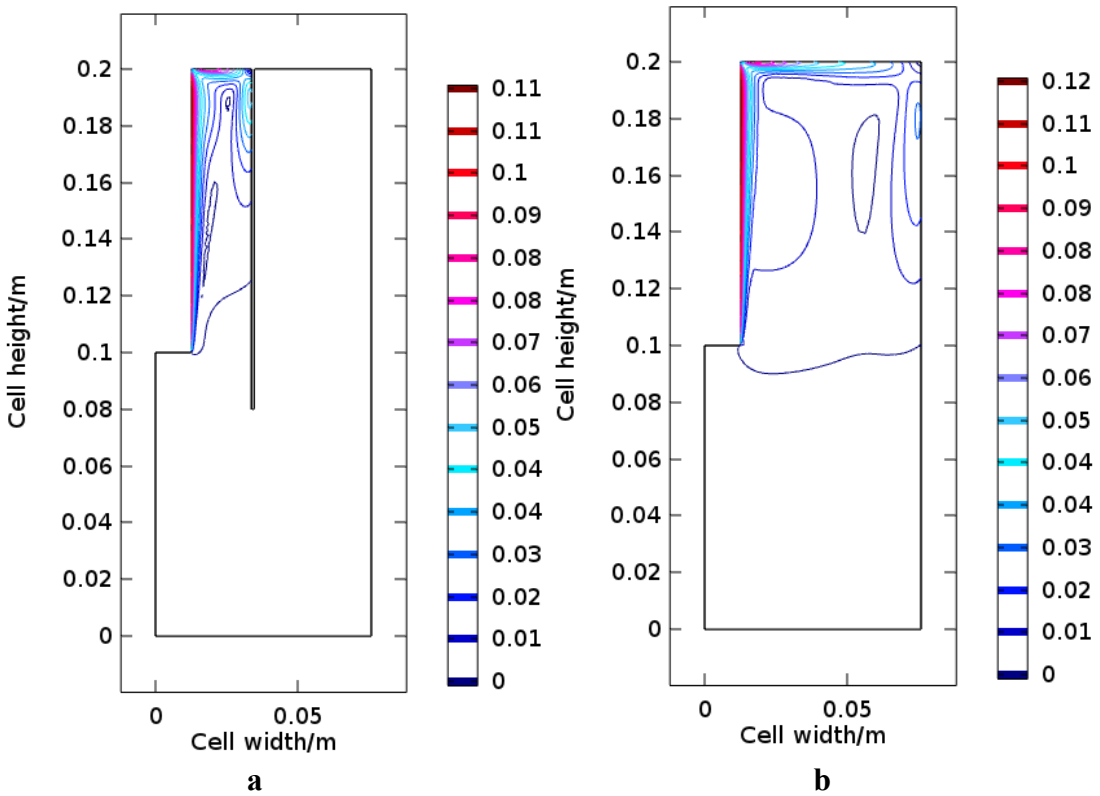

Fig 3-7 Velocity contours in the cell a) with diaphragm b) without diaphragm

The cell potential for the base case, with the use of a diaphragm, is 9.54 V while it goes down to 5.7 V when the diaphragm is removed. This high potential drop due to the diaphragm can be explained by its effect on the ionic mass transfer. In fact, the diaphragm separates the cell into two velocity field regions. The smaller region near the anode is turbulent while the velocity for the rest of the cell is almost zero. As a result, the turbulent diffusivity in the region between the anode and the diaphragm boosts the mass transfer. Moreover, the electrodes are less accessible for the ions when there is a diaphragm in the

cell as it is defined in this work. In other words, the diaphragm is introducing an additional ohmic overpotential in the cell by blocking the path of ions. Moreover, the distribution of the current density along the anode is greatly influenced by the diaphragm, see Fig 3-8. The diaphragm blocks the passage of current in the solution: the chloride/lithium ions should then bypass the diaphragm to reach the anode/cathode. The bottom corner of the anode then becomes the shortest path for the ions to reach the anode or to escape from it. Therefore, the current density sharply increases from the top to the bottom along the anode with a maximum current density located at the bottom corner of the anode, see Fig 3-8. In addition, the resistance of the bubble layer is proportional to its thickness and increases from the bottom to the top of the anode. All those phenomena cause a 3.84 V increase in the electrolyte potential.

At the beginning of the simulation, the cell potential is 9.3 while it increases to 9.5 V after 1 h of simulation. A voltage distribution along the anode height is shown for the design with a diaphragm (see Fig 3-9). In fact, the cell potential is the sum of the anodic equilibrium potential (fixed by thermodynamics) and two different overpotentials: ohmic overpotential (sum of electrolyte potential and resistive layer overpotential) and anodic overpotential.

Firstly, the anodic overpotential is approximately 1 V along the whole anode surface. Secondly, it should be noticed here that the equilibrium potential of the anode is the difference between the equilibrium potential of the oxidation of chloride and that of the lithium reduction. Thirdly, the resistive layer overpotential representing the product of the current density and of the local resistance decreases from the bottom to the top of the anode. The resistive layer overpotential due to bubbles and the electrolyte potential behave quite differently depending on the presence or not of a diaphragm in the cell. In the case with a diaphragm, the current density at the bottom of the anode is 10 times of that at the top. The decrease of the current density overcomes the increase of resistance along the anode height. Such a situation does not apply in the case without diaphragm where the resistive layer

overpotential increases from the bottom to the top of anode, see Fig 3-10. For both cases, the behaviour of the electrolyte potential and of the resistive layer overpotential is opposite.

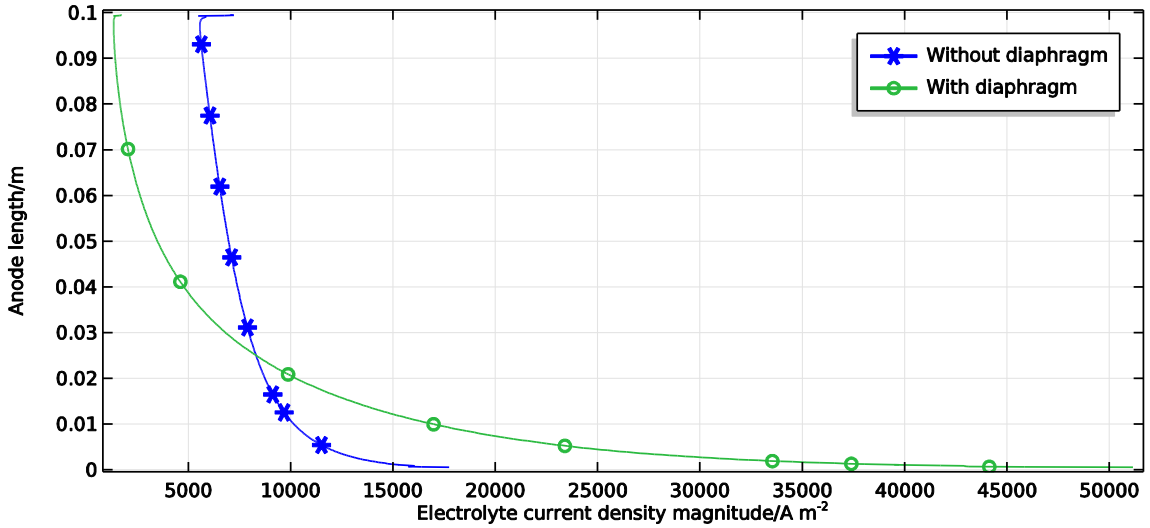

Fig 3-8 Electrolyte current density magnitude for the cell with and without diaphragm along the anode height

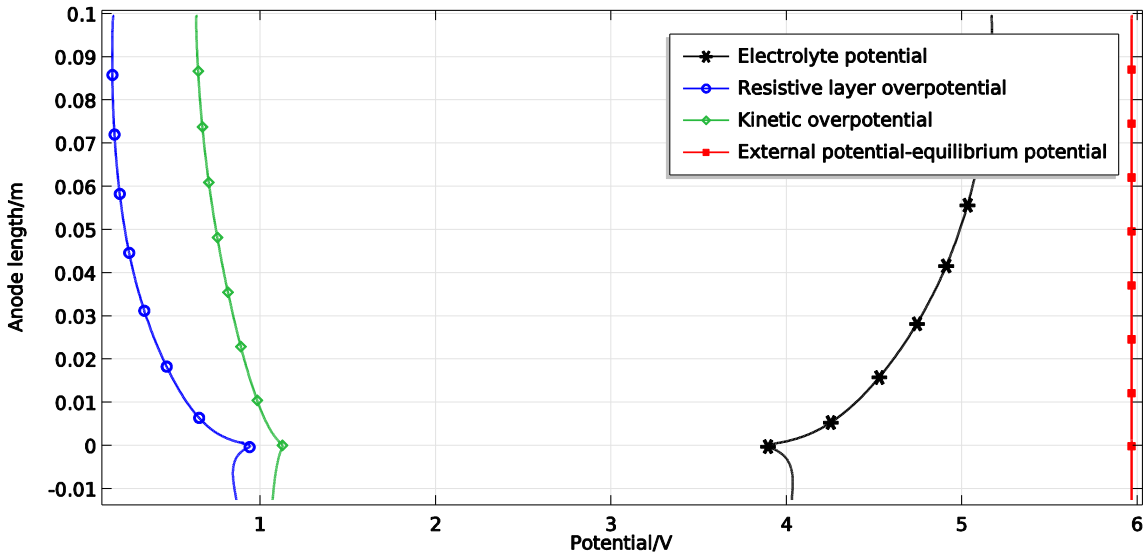

Fig 3-9 Potential and overpotentials along the anode height for the cell with a diaphragm

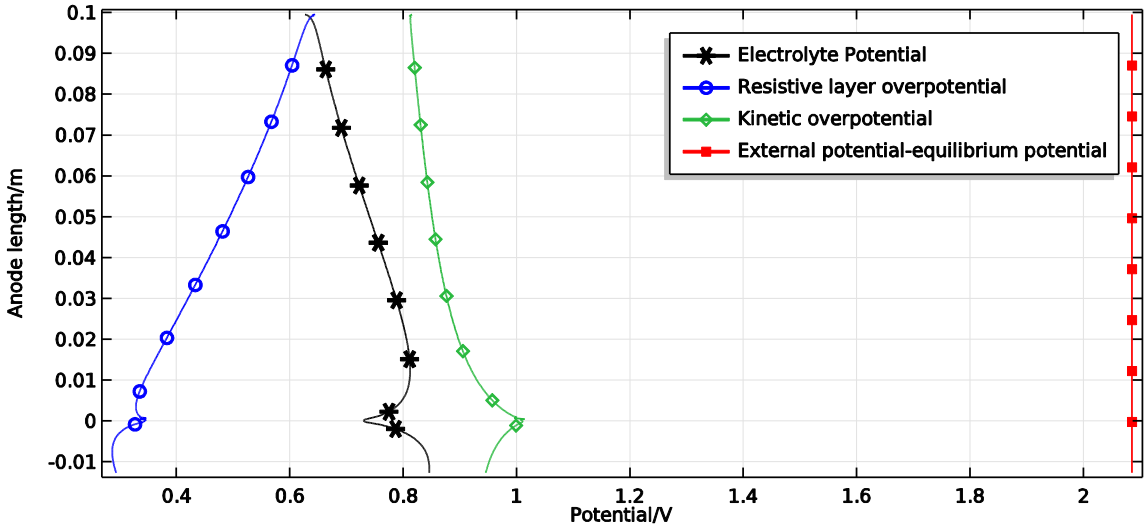

Fig 3-10 Potential and overpotentials along the anode height in the cell without diaphragm

At the cathode, for the cell with a diaphragm, the maximum kinetic overpotential is approximately -45 mV, found at the surface of the cathode facing the bottom corner of the diaphragm. For the cell without diaphragm, it becomes -35 mV, found at the surface of the cathode facing the anode. For both cases, the Li^+ concentration gradient is maximum at these locations. A linearized B.V. kinetic is thus appropriate for such cases.

The effect of the current density and of the ACD on the concentration and electric fields of the experimental lithium production cell are next considered. To ease the comparison, the simulation of the cell with different current densities is done using the geometry of the base case. On the other hand, the simulations with different ACD are performed with the boundary conditions used in the base case. The four dimensionless numbers below are used for the following results:

cLi* = lithium ions concentration per initial lithium ions concentration

cLi** = lithium concentration per that of the base case

Cd** = current density per that of the base case (7800 A m^{-2})

ACD** = ACD per ACD of the base case (0.635 m)

3.5.3 Effects of the Current Density on the Electric and Concentration Fields

A total polarization curve, including ohmic, electrochemical and transport polarizations and showing the current density versus the total cell potential, is first presented in Fig 3-11 . As one should expect from an electrochemical cell, the potential increases with the current density. As an explanation of the linearity between the current and the voltage, the effect of current on the ohmic polarization is dominant and much higher than its effect on the electrochemical polarization.

Out of the eleven cases presented in Fig 3-11, four cases are selected to show the effects of the current density on the concentration of lithium ions at the level M (see Fig 3-12). As expected, the higher current density causes lower concentrations of electroactive ions at each time step, while their behaviour follow the same trend. It shows that if the current increases by an increment of 1000 A m^{-2}, the concentration in each point will decrease by a constant amount.

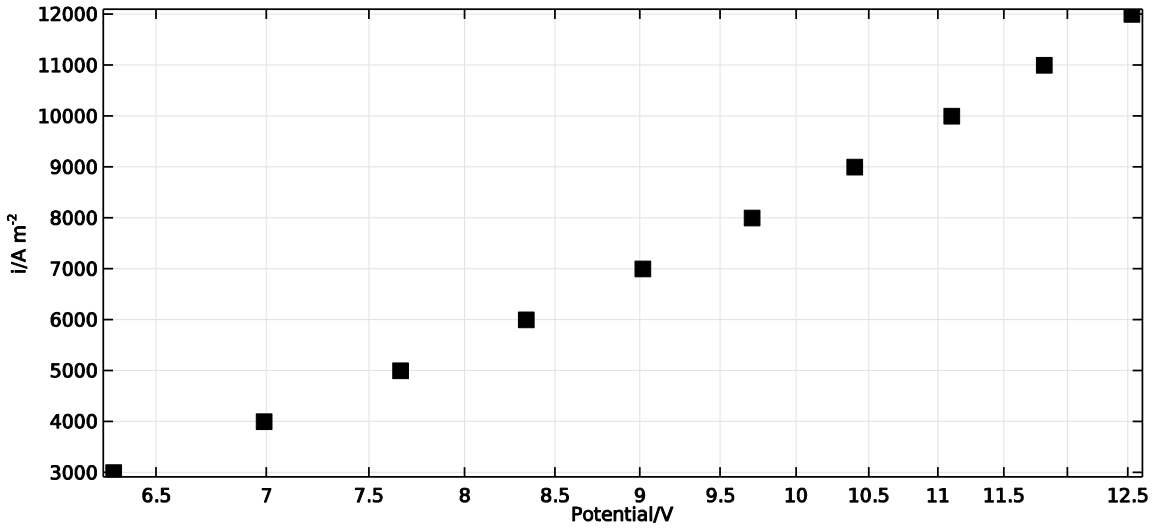

Fig 3-11 Total polarization curve after 1h of simulation

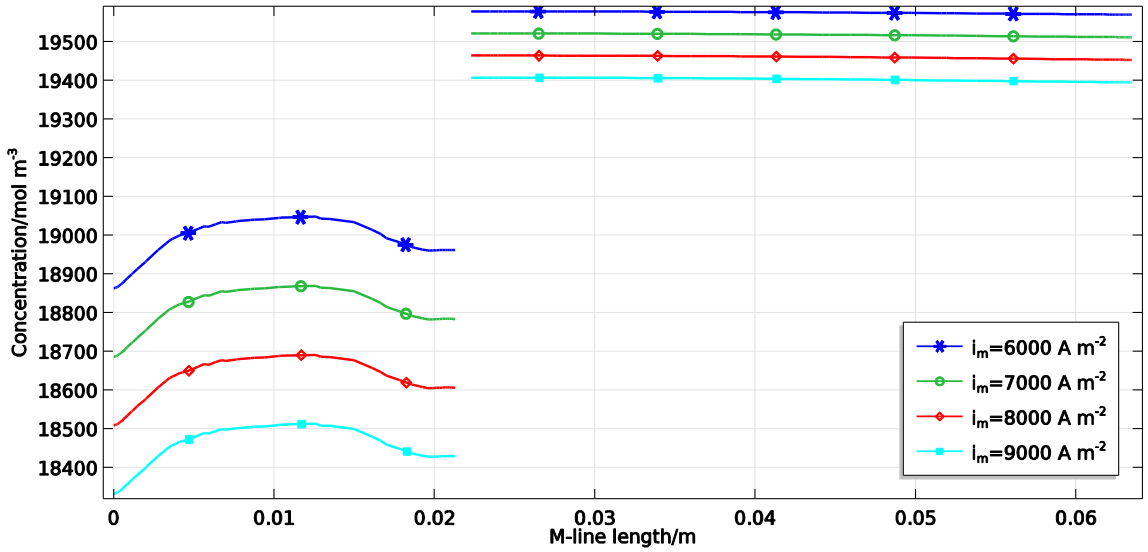

Fig 3-12 Concentration of lithium ions at the level M for the simulations with different average current density (im) with a diaphragm and after 1 h of simulation

Previously, the variation of the different components of the anodic overpotential along the height of the anode was shown in Fig 3-9. The current density doesn't have a noticeable effect on the anodic overpotential but the bubble resistive layer overpotential and the electrolyte potential are affected significantly by the current density, see Fig 3-13. In fact, the effect of the gas bubbles on the electric field is important as the presence of a resistive layer at the surface of the anode is changing the local current density. The resistivity of this layer is proportional to the bubble coverage, which is a function of the current density. As expected, the ohmic overpotential of this layer is proportional to the local current density and its resistivity (Ohm's law), due to the bubble production which is proportional to current density. Therefore, as can be seen in Fig 3-13, at any given position of the anode, the resistive layer overpotential increases when the current density increases. Moreover, Fig 3-13 shows that for any given position on the anode, the electrolyte overpotential increases by a constant value when the current density increases by increments of 1000 A m^{-2}.

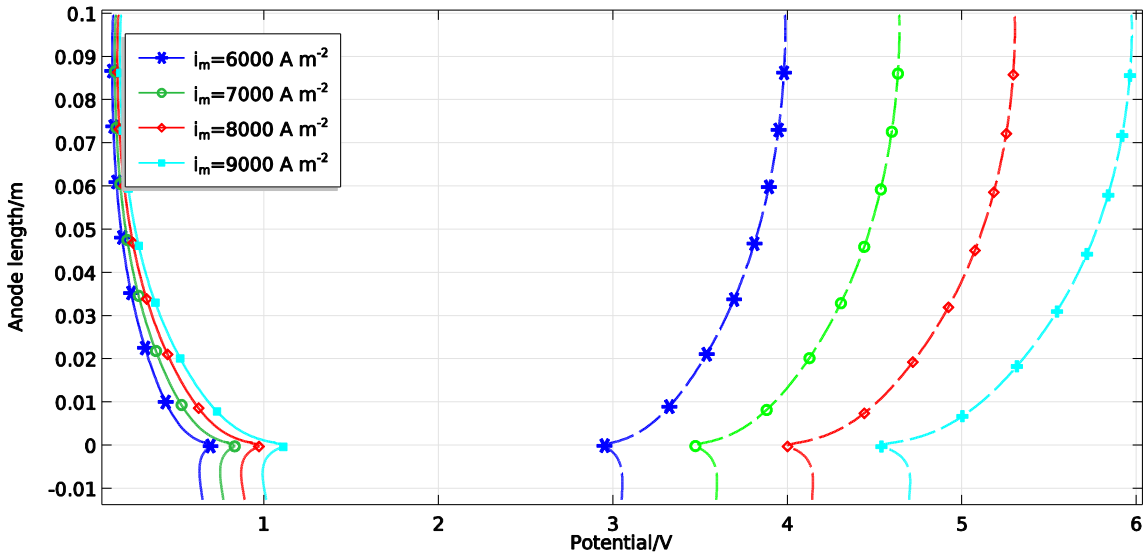

Fig 3-13 Bubble resistive layer overpotential (solid lines) and electrolyte overpotential (dash lines) for the simulations with different i_m with a diaphragm and for 1 h of simulation

3.5.4 Effect of the ACD on the Electric and Concentration Fields

The ACD has noticeable effects on both electric and concentration fields. As expected, at a fixed current density, the ACD has no effect on the mole consumption of active ions. However, the cells with smaller ACD contain less electrolyte and, as a result, their ions concentrations decrease faster than in cells with larger ACD. Fig 3-14 shows the lithium ions concentration per its initial concentration along the level M for the cells with 5 different ACD, after 1 h of simulation.

On the other hand, while the concentration of electroactive ions at the surface of electrodes decreases with a decrease of ACD, the cathodic and anodic overpotentials increase. Below a limiting ACD value, which was estimated at 4.5 cm in the configuration with a diaphragm, the cathodic overpotential gets bigger than 50 mV and the B.V. equation, instead of linearized B.V. as was used previously, has to be used for the cathodic reaction. Fig 3-15 shows the effect of the ACD on the cell potential. According to Ohm's law, the potential of the cell is proportional to ACD. In fact, at a constant current density, the potential is proportional to the total resistivity of the cell, increased at higher ACD. At fixed current density, the cell potential is affected by the electrode kinetics, by the resistivity and thus by the concentration. A decrease of the concentration of active ions increases the cell

potential through an increase of the kinetic, concentration and ohmic overpotentials. Moreover, according to Fig 3-15, the difference between the cell potential for different ACD decreases over the time because the decrease of the conductivity is faster in smaller ACD.

ACD also affects the flux of the ions perpendicular to the surface of electrodes. In other words, it affects the electrolyte current density, which is maximum at the surface of cathode, facing the bottom corner of the diaphragm, where is the shortest path for the ions to go from one electrode to the other. At smaller ACD, the electric field is stronger because the electrodes are closer. As a result, more ions transfer through the shortest path. All of which cause the maximum of electrolyte current density to be much higher at smaller ACD, see Fig 3-16.

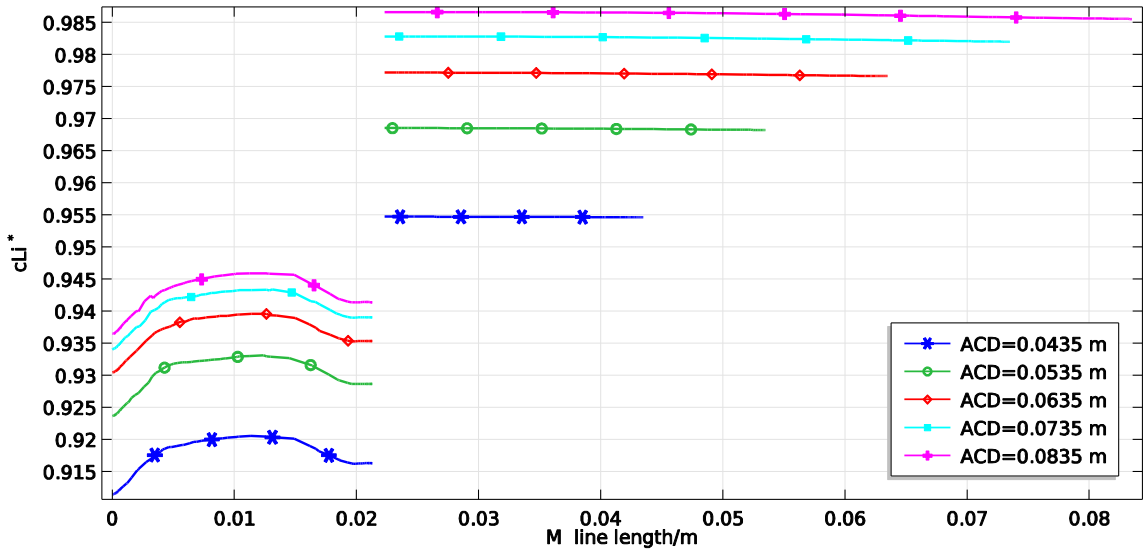

Fig 3-14 Li^+ concentration per initial concentration at M line for different ACD after 1 h of simulation and with diaphragm

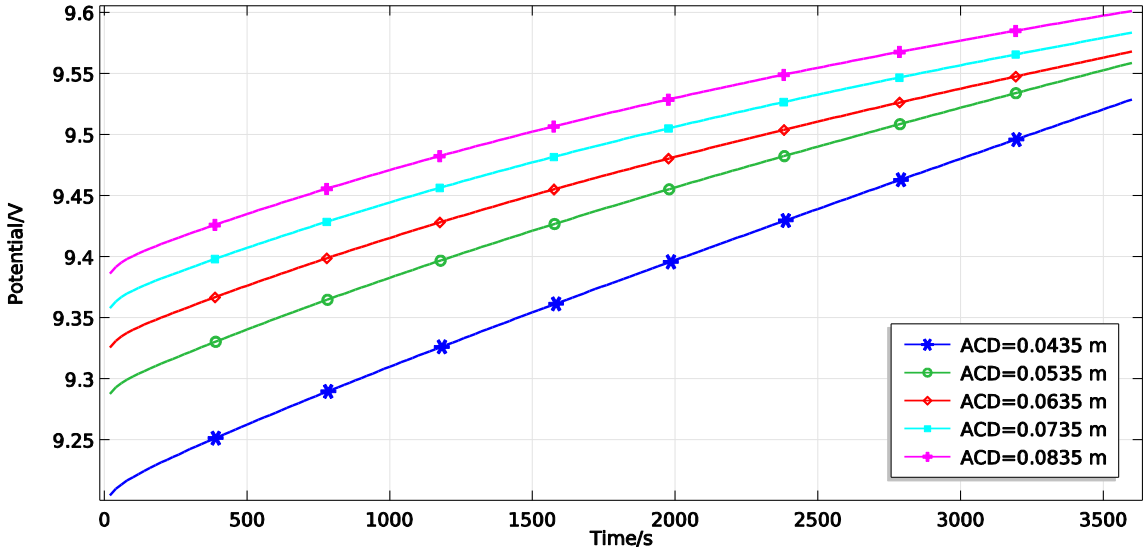

Fig 3-15 Cell potential over the time for the simulations with different ACD

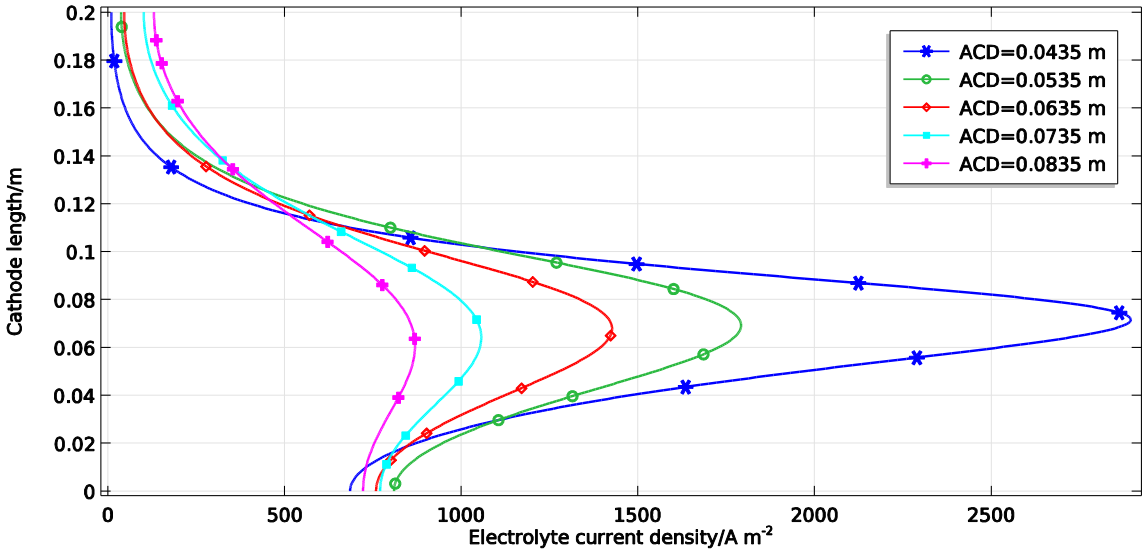

Fig 3-16 Electrolyte current density magnitude along cathode with diaphragm and 1 h simulation

The effects of the current density and of the ACD on the concentration of ions over time were explained previously. It is interesting to see which of ACD and current density is the most influential on the concentration of electroactive ions at the surface of electrodes. Consequently, we tried to fit the results obtained after 1 h of simulation with the equations below:

$$cLi^{**} = (ACD^{**})^{0.1} \tag{3-19}$$

$$cLi^{**} = (Cd^{**})^{-0.0298} \tag{3-20}$$

According to equations (3-19) and (3-20), the lithium ions concentration at the surface of the cathode is more influenced by the dimensionless ACD than by the dimensionless current density. This result can be extended to the concentration of all ions at both electrodes.

3.6 Conclusion

This research presented an integrated mass transfer model for the lithium production cell based on the use of COMSOL®, a CFD commercial software. In this study, a one-phase axisymmetric electrochemical cell model has been developed and calibrated with the measurements of an experimental setup in order to investigate the effect of cell operating parameters like current density or ACD distance on the electric, flow and concentration fields inside a lithium production cell. A moving wall anode has been used to simulate the effect of the anodic bubbles generation on the flow field. This simplified model has been checked and validated by simulating a magnesium cell and comparing the one-phase results with the experimental and numerical data of two phases flow obtained by Liu et al.[8].

A comparison between the flow pattern inside an experimental cell with and without the presence of a dense diaphragm confirms the role of the diaphragm in preventing the back reaction between the chlorine bubbles and the produced liquid lithium. However, such a design feature introduces an additional voltage drop, which can lead to a specific energy consumption increase of about 40%. Moreover, the effect of the current density and of the ACD on the electric and concentration fields of the cell were considered separately. The analysis showed that the concentration of ions at the surface of the electrodes decreases with an increase of the current density and with a decrease of the ACD, whereas the

dimensionless ACD is more influential than the dimensionless current. As expected, the cell potential is higher when both current density and ACD are larger.

For the next steps, the authors suggest to study the effect of diaphragm porosity, size and location on the velocity, electric and concentration fields. Different cell design could also be studied to look after the effect of the geometry of the cell on the flow and on the mass transfer.

The new knowledge and the simulation tool developed in this work open up new possibilities as to design a novel low energy consumption cell. Furthermore, this work shows an important progression in the simulation of the electrolysis of light metal halides.

3.7 Nomenclature

c	Concentration (mol m^{-3})
D	Diffusion coefficient (m^2 s^{-1})
D_{eff}	Effective diffusion coefficient (m^2 s^{-1})
d	Diameter (m)
E_o	Eotvos number
F	Faraday‘s constant (A s mol^{-1})
g	Earth gravitational acceleration (m s^{-2})
i	Current density (A m^{-2})
i_0	Exchange current density (A m^{-2})
i_m	Average current density (A m^{-2})
k	Turbulent kinetic energy (m^2 s^{-2})
k_r	Reaction rate constant (m s-1)
M	Morton number
n	Number of electrons
N	Mole flux (mol m^{-2} s^{-1})
R	Gas constant (J mol^{-1} K^{-1})
R′	Production term (mol m^{-3} s^{-1})
Re	Reynolds
t	Time (s)
T	Temperature (K)
u_m	Ions mobility (m^2 s^{-1} V^{-1})
u_T	Bubble terminal velocity (m s^{-1})
V	Velocity vector (m s^{-1})
x	Mole fraction
z	Valence

Greek letters

α	Transfer coefficient
ϵ	Rate of dissipation of kinetic energy (m^2 s^{-3})

σ	Conductivity (S m^{-1})
ρ	Density (kg m^{-3})
μ	Viscosity (kg s^{-1} m^{-1})
γ	Surface tension (N m^{-1})
Φ	Potential field (V)
$\emptyset_g$	Bubble coverage
η	Activation overpotential (V)

Subscript/ Superscripts

a, c	Anode/ Cathode
b	Bubble
l	Electrolyte
i	Species i
j	Species j
m	Average
mix	Mixture
s	Electrodes' surface
T	Turbulent
*	Bulk

CHAPITRE 4 : AVANT-PROPOS

Auteurs et affiliation:

- Elaheh Oliaii: étudiante au doctorat, Université de Sherbrooke, Faculté de génie, Département de génie chimique et de génie biotechnologique.
- Martin Désilets: professeur, Université de Sherbrooke, Faculté de génie, Département de génie chimique et de génie biotechnologique.
- Gaétan Lantagne: Directeur - Recherche et innovation, Hydro-Québec, Varennes, QC J3X-1S1, Canada

Date d'acceptation: Feb 2018
État de l'acceptation: version finale accepté
Revue: Journal of Applied Electrochemistry
Référence: [10]

Titre français: Effet des paramètres de design sur le transfert de masse et la consommation d'énergie dans une cellule d'électrolyse du lithium

Contribution au document:

Cet article contribue à l'étude de la même cellule d'électrolyse du lithium, avec l'analyse de différentes variables de design comme la longueur du diaphragme, sa position et sa porosité. Le modèle a été amélioré par la simulation d'un écoulement à 2 phases, la présence du Cl_2 étant prise en compte de façon plus rigoureuse.

Résumé français:

Un modèle 2-D axisymétrique représentant les phénomènes électrochimiques se produisant au sein d'une cellule expérimentale de production de lithium a été résolu en utilisant une méthode basée sur les éléments finis. Le modèle prend en compte le couplage entre les phénomènes suivants : transfert de masse et de momentum, électrocinétique, électrostatique. Le diaphragme dense utilisé dans le montage expérimental n'est pas

hydrauliquement perméable. Il sépare la cellule en 2 régions : 1- une région turbulente entre l'anode et le diaphragme et 2- une région laminaire entre le diaphragme et la cathode. Un modèle k-epsilon est utilisé pour résoudre l'écoulement turbulent résultant des bulles générées à l'anode. Un modèle d'écoulement à 2 phases a également été développé pour simuler les fractions volumiques de bulles et d'électrolyte dans la cellule. La distribution non uniforme de bulles sur la surface de l'anode, tributaire de la distribution non uniforme de courant, a été prise en compte dans le modèle à 2 phases.

Les effets de la longueur du diaphragme, de sa position et de sa porosité sur les champs électrique et d'écoulement ont été simulés. En fait, la position du diaphragme et sa longueur influencent la distribution du courant à la surface des électrodes et la distribution des vitesses dans la cellule, qui à leur tour influencent les surtensions ohmiques et cinétiques. Les résultats montrent que jusqu'à 40% de l'énergie peut être sauvée lorsque la cellule d'électrolyse du lithium est opérée avec un diaphragme plus court, poreux et situé aussi loin que possible de la surface de l'anode. La densité de courant maximale, observé au coin inférieur de l'anode, est plus élevée quand le diaphragme est plus long et lorsqu'il est situé plus près de l'anode.

4 Effect of the design parameters on mass transfer and energy consumption inside a lithium electrolysis cell

4.1 Abstract

A 2D axisymmetric electrochemical model of a lithium experimental cell is solved using a finite element method. The model is considering the coupled effect of momentum, electric, kinetic and mass transfer phenomena. The dense diaphragm used in the setup, which is not hydraulically permeable, separates the cell into two regions: 1- a turbulent region, between the anode and the diaphragm, and 2- a laminar region between the diaphragm and the cathode. The k-epsilon model is used to solve the turbulent flow resulting from bubbles generation at the anode. A two-phase flow model is also developed to simulate the volume fractions of bubbles and electrolyte in the cell. The non-uniform bubbles distribution over the anode surface, derived from the non-uniform current distribution, has been added to the two-phase model.

The effects of the diaphragm length, position and porosity on the electric and two-phase flow fields are simulated. In fact, the diaphragm position and length both influence the current distribution at the surface of electrodes and the velocity distribution in the cell, all of which influence ohmic and kinetic overpotentials. The results show that up to 40% of energy can be saved when running the lithium electrolysis cell with a shorter porous diaphragm located as far as possible from the anode. The maximum current density, found at the bottom corner of anode, is higher when the diaphragm is longer and when it is closer to the anode.

Keywords: Lithium electrochemical cell, mass transfer, turbulent two-phase flow, finite element model

4.2 Introduction

Being the lightest metal in the periodical table makes lithium very attractive for different industrial purposes from lithium batteries to low-weight alloys for transport applications.

The most common process for the industrial production of metallic lithium is from the electrolysis of lithium chloride, through reactions presented below:

At the cathode: $Li^+ + e^- \rightarrow Li\ (liquid)$

At the anode: $2Cl^- \rightarrow Cl_2(gas) + 2e^-$

The electrolyte of the cell contained 60% LiCl and 40% KCl.

However, the technology has an important limitation related to the back reaction between chlorine and metallic lithium formed as a result of the electrochemical reactions:

$$Cl_2\ (gas) + 2Li\ (liquid) \rightarrow 2\ LiCl\ (liquid)$$

The problem can be limited by working with a quasi-divided cell blocking the path of the chlorine gas to the cathode via the use of a diaphragm or separator, located between the electrodes. Different cells have been designed to increase the purity of the produced lithium and the current efficiency by preventing the back reaction inside the cell [36,39–42,44,57]. However, the information provided in these documents is very general and does not include any technical details like concentration, potential and velocity distributions in the cell.

The energy consumption of an electrolysis cell with fixed current depends on its potential. The potential distribution inside an electrochemical cell depends on ion mass transfer, controlled by the velocity field, electrolyte properties and the design of the cell. The potential field is also affected by heterogeneous reactions. When all these phenomena occur at high temperature inside a corrosive environment, it becomes a serious obstacle to the experimental analysis of the detailed cell behavior. Furthermore, the numerical solution of the differential equations representing such a system is a challenging task due to the inherent coupling between these phenomena. A three-phase flow and mass transfer inside a commercial lithium electrolysis cell was simulated by Li et al [30]. They concluded that the bubbles diameter size does not have a significant effect on the flow field. Moreover, the transfer of ions to the electrodes through convection, produced by the bubbles, are much higher than the electrochemical reaction rate. However, these results were obtained without any consideration of the coupling between the electric field and mass transfer. According to the author's knowledge, this thesis is the first to present the numerical model solving the species mass transfer and potential distribution simultaneously inside a lithium cell.

In this chapter, the effect of design parameters like the diaphragm length, position and porosity on electric fields and mass transfer is presented. Two types of simulations are conducted: firstly, the electric field is coupled to the concentration and velocity fields in order to assess the impact of design parameters on the electric field. In these simulations, the momentum conservation is modeled by a one-phase flow to decrease the computational effort, and to make it easier to converge. In the second part of this chapter, a two-phase flow model is developed to solve the volume fraction of the chlorine gas and electrolyte and to show the effect of the diaphragm length and position on the velocity field. In this part, the electric field is not solved. All simulations are conducted using COMSOL®, a commercial finite element simulation software. The base case model, onto which all simulations are based, has been previously validated with the use of experimental measurements conducted on lab cells at Hydro-Québec facilities [8].

4.3 Methodology

4.3.1 Base case

A base case has been simulated and validated by the use of experimental data obtained from a lithium electrolysis cell setup, operated in Hydro-Québec, Canada by Amouzegar and Harrison [7]. Schematic of this cell and operating parameters are presented in Fig 4-1 and Table 4-1, respectively. The cylindrical shape of the cell is simplified and simulated as a 2D-axysimetric, see Fig 4-1b. The upper part of the cell, above the electrolyte surface, is not considered in the simulation because its effects on electric, concentration and flow fields are negligible. The numbers in Fig 4-1b point out the boundaries, identified in the Figure's caption.

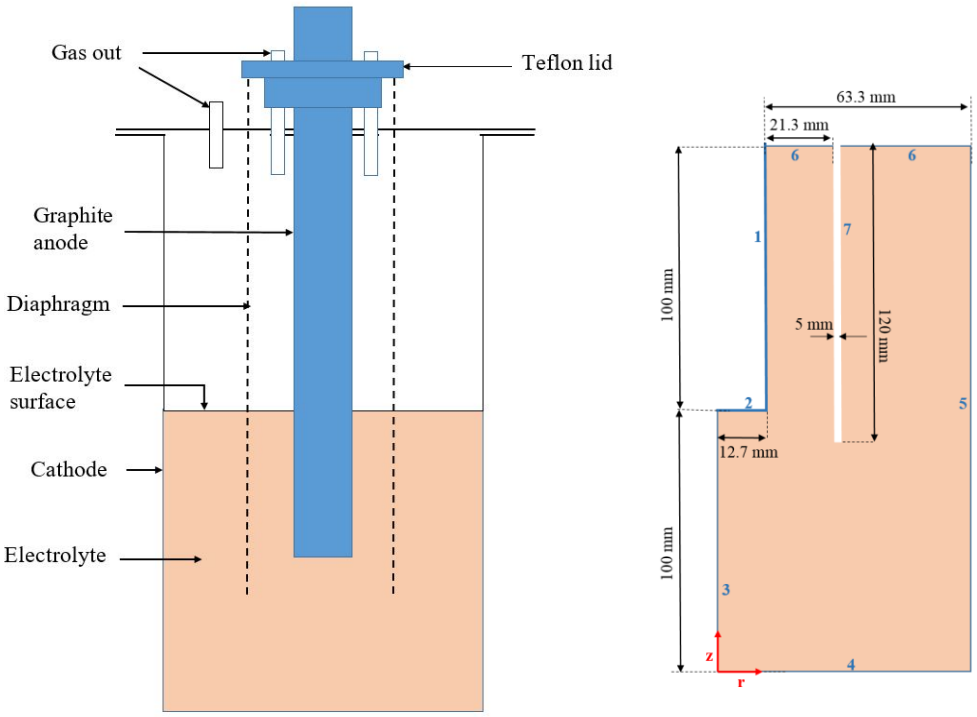

a b

Fig 4-1 Schematic of standard cell a) experimental setup b) simulation geometry (1:Anode, 2:Anode, 3: Symmetry, 4: Bottom, 5:Cathode, 6: electrolyte surface, 7: Diaphragm)

Table 4-1 Experimental operating parameters

c_{K+} at t=0 [kmol m^{-3}]	c_{Cl-} at t=0 [kmol m^{-3}]	c_{Li+} at t=0 [kmol m^{-3}]	Temperature [K]	Current [A]	Current density [A m^{-2}]
10.8	30	19.2	723	60	7800

More data and information about this lithium electrolysis cell such as ions diffusion coefficients can be find in the previous chapter, Table 3-2 [9].

4.3.2 Simulation of electric and concentration fields - one phase flow

For the first part of this work, the electric and concentration fields are solved using a tertiary current distribution approach, coupled with a one-phase turbulent flow. In reality, three phases are present in a lithium electrolysis cell: metallic liquid lithium that forms at the cathode, chlorine bubbles evolving at the anode and a molten KCl-LiCl salt used as the electrolyte. According to the assumptions listed below, only the most important phenomena

are considered in the simulation of this simplified one-phase flow, like the effects of the bubbles on the electric, concentration and flow fields:

- The liquid electrolyte is the phase which has been simulated
- The kinetic overpotential at the cathode is low enough to be represented by a linearized Butler-Volmer (B.V.) equation.
- The highly conductive metallic lithium, sticking at the surface of the cathode and moving upward slowly, does not have any significant effect on the electric, concentration and velocity fields.
- The oxidation of chlorine is a slow reaction and its overpotential is high. As a result, the anodic kinetic overpotential is expressed by a Tafel equation.
- Cl_2 bubbles are covering part of the anode surface, so not all the surface of the anode is available for the oxidation reaction. In this way, the bubbles create an additional overpotential, called hyperpolarization, which can be expressed as [58]:

$$\eta_h = \frac{RT}{\alpha_{O_a} F} \log(A/A_h) \tag{4-1}$$

Where α_{O_a} is the transfer coefficient of the oxidation reaction at the anode, taken to be 0.5, and A_h is the anode's area not covered by gas bubbles. Inserting this expression into the Tafel equation results in:

$$i_a = i_{0_a}\left(1 - \emptyset_g\right)\left[exp\left\{\frac{\alpha_{O_a} F}{RT}\eta\right\}\right] \tag{4-2}$$

Where $\emptyset_g$, the bubble coverage, is related to the anodic current density, i_a, by the following equation [53,59]:

$$\emptyset_g = 0.023\ {i_a}^{0.3} \tag{4-3}$$

Accordingly, one can interpret the hyperpolarization as a reduction of the anode surface that is available for the oxidation reaction.

- A resistive layer defined at the surface of the anode represents the effect of the bubbles on the electrolyte conductivity. The thickness of this layer is considered to increase from the bottom to the top of the anode, resulting in a bubble layer shape similar to what is found at the surface of the anode of magnesium production cells [8]. The conductivity of this resistive layer is calculated according to the Bruggeman's correlation [52]:

$$\sigma_{mix} = \sigma_c\left(1 - \emptyset_g\right)^{1.5} \quad (4\text{-}4)$$

- Electrolyte conductivity is a function of ions concentration and mobility. Since no information is available about the mobility of the lithium cell's ions, their mobilities are replaced by the Nernst-Einstein equation. As a result, the equation below is used for the electrolyte conductivity:

$$\sigma_c = F^2 \sum_i z_i^2 \frac{D_{i,eff}}{RT} c_i \quad (4\text{-}5)$$

Where $D_{i,eff}$, the effective diffusion coefficient is calculated by the Wilke's correlation [50]:

$$D_{i,eff} = \frac{1 - x_i}{\sum_{\substack{j=1 \\ j \neq i}} \frac{x_j}{D_{ij}}} \quad (4\text{-}6)$$

D_{ij}, the binary diffusion coefficients, can be find in Chapter three, Table 3-2.

- As mentioned before, the bubbles movement is simulated by considering the anode as an upward moving wall [9]. Its velocity is set in the way to have the same velocity pattern as that of two-phase flow simulations.
- The effect of turbulence on the mass transfer is considered through the additive effect of the turbulent and effective molecular diffusivities. It is worth mentioning that when the turbulent Schmidt number is assumed to be one [50,60–62], the turbulent diffusion coefficient is equal to turbulent kinematic viscosity, a result taken directly from the simulation of the turbulent flow.
- The ions flux is solved through Nernst-Planck equation and electroneutrality [9].
- The potential distribution is obtained from charge conservation equation:

$$\boldsymbol{\nabla}.\left(-F\left(\boldsymbol{\nabla} \sum_i z_i D_{i,eff} c_i\right) - \sigma_c \boldsymbol{\nabla} \Phi_c\right) = 0 \quad (4\text{-}7)$$

This model, including a one-phase turbulent flow fully coupled with the electrochemical problem, has already been described in details and validated in a previous chapter. Boundary conditions for the electric, concentration and one-phase flow fields are the same as those are mentioned in the previous work, see Table 4-2. The boundaries are referring to the caption of Fig 4-1b.

Table 4-2 Boundary conditions for velocity, electric and concentration fields [9]

Boundaries	Flow field B.C.	Electric field B.C.	Concentration field B.C.
1	V_r=0, V_z=u_t (moving wall)	i_{mean}=7800 [A m^{-2}]	-$n.N_i$=i_a/F
2	V_r=0, V_z=0	i_{mean}=7800 [A m^{-2}]	-$n.N_i$=i_a/F
3	dV_r/dr=0, dV_z/dr=0	di/dr=0	dN_i/dr=0
4	V_r=0, V_z=0	$i.n$=0	-$n.N_i$=0
5	V_r=0, V_z=0	Φ =0 [V]	-$n.N_i$=i_c/F
6	V_r=0, V_z=0	$i.n$=0	-$n.N_i$=0
7	V_r=0, V_z=0	$i.n$=0	-$n.N_i$=0

One shall also note that to simulate the effect of length and position of diaphragm on the electric, concentration and flow field, the diaphragm was considered as a dense insulator with no hydraulic porous flow. In addition, the effects of porosity on aforementioned fields is also considered through equations given in the following section.

4.3.3 Equations for the porous diaphragm

Introducing the transport phenomena occurring inside a porous diaphragm involves writing a mass conservation law for each species, and the flux of species as defined by the Nernst-Planck equation, by integrating the porosity ε parameter, as follows:

$$\frac{\partial \varepsilon c_i}{\partial t} = \nabla.\left(c_i \mathrm{V} - D_{i,eff_{dia}} \nabla c_i - \mathrm{z_i} F u_{m,i} c_i \nabla \Phi\right) \quad (4\text{-}8)$$

In fact, in a porous diaphragm, the cross section available for the diffusion is less than that in the electrolyte. Moreover, to bypass the diaphragm, ions should travel a bigger distance than through the diaphragm thickness. As a result, the diffusion coefficient of ions in the diaphragm, $D_{i,eff_{dia}}$, is less than that in the electrolyte and it is given by the equation below:

$$D_{i,eff_{dia}} = \frac{\varepsilon}{\tau} D_{i,eff} \quad (4\text{-}9)$$

While the tortuosity, τ, is related to the porosity with the Bruggeman correlation [63–65]:

$$\tau = \varepsilon^{-0.5} \quad (4\text{-}10)$$

Other equations used to estimate the electric and concentration fields can be taken from chapter three, by first substituting the transport properties applicable to the bulk by those applicable to porous media as the Bruggeman correlation.

4.3.4 Two-Phase Flow Simulation

A two-phase flow model is also developed to investigate the behavior of the chlorine bubbles in the cell and to assess the volume fraction of chlorine gas near the cathode, a result closely linked to the importance of the back reaction between chlorine and liquid lithium.

4.3.4.1 General Equations

Different models are available for the simulation of two-phase flows and can be classified in two main categories: interface tracking methods and disperse methods. The interface tracking methods provide a clearer picture of the flow field, but their computational cost is prohibitively high and many experimental parameters need to be defined. On the other side, the most versatile method amongst the portfolio of disperse methods is the Eulerian-Eulerian model, in which the velocity field for each phase is calculated through the solution of two sets of Navier-Stokes equations, one for each phase. This model is computing the volume fraction of each phase instead of tracking the position of the interface between the two phases, thus lowering the computational effort. In this work, an Eulerian-Eulerian, gas-liquid model is developed to simulate the two-phase flow inside the Li production cell.

To solve the mass conservation and momentum governing equations below, it was assumed that:

- all material properties are constant,
- based on previous one-phase flow simulations in chapter three, the bubble size is considered to be constant, d_b=1.5 mm [9].
- there is no mass exchange between the phases.

In a 2-phase flow, the mass conservation equations become:

$$\frac{\partial \varphi_k \rho_k}{\partial t} + \nabla.(\varphi_k \rho_k u_k) = 0 \qquad \text{k = c (continuous phase); d (disperse phase)} \quad (4\text{-}11)$$

The momentum conservation equations are expressed by:

$$\frac{\partial(\varphi_k \rho_k u_k)}{\partial t} + \nabla.(\varphi_k \rho_k u_k u_c) = -\varphi_k \nabla p + \nabla.\left(\varphi_k T_k^{turb}\right) + \varphi_k \rho_k g + F_b \qquad \text{k= c, d} \qquad (4\text{-}12)$$

With $\varphi_c = 1 - \varphi_d$ (4-13)

Where T_k^{turb}, the stress tensor, is described as follow:

$$T_k^{turb} = -(\mu_k + \mu_{T,k})(\nabla u_k + (\nabla u_k)^T - \frac{2}{3} I(\nabla u_k)^T) \qquad (4\text{-}14)$$

The volume force, F_b, typically includes drag, lift and virtual mass forces. The effect of lift and virtual mass forces are considered negligible in comparison with the drag force [66], which was given by:

$$F_D = -\frac{3\, C_D}{4 d_b} \varphi_d \rho_c |u_d - u_c| (V_d - V_c) \qquad (4\text{-}15)$$

Where

$$C_D = \begin{cases} \frac{24}{Re}(1 + 0.15 Re^{0.687}) & Re \leq 1000 \\ 0.44 & Re > 1000 \end{cases} \qquad Re = \frac{d_b \rho_c |u_c - u_d|}{\mu_c} \qquad (4\text{-}16)$$

The same value of the drag force is acting on the electrolyte continuous phase (but in the opposite in direction).

The widespread k-epsilon model is used to solve the turbulent flow with a stationary and time independent solver.

4.3.4.2 Boundary conditions for the two-phase flow

It is assumed that the bubbles are entering into the electrolyte in a direction normal to the vertical part of the anode surface. Their inlet velocity is estimated according to the Faraday's law [67]:

$$u_{d_{in}} = \frac{i_a M_d}{z F \rho_d \emptyset_g} \qquad (4\text{-}17)$$

Where z = 2 represents the number of electrons involved in the generation of 1 mole of chlorine gas. The current density distribution at the surface of the anode, i_a, is calculated using a secondary current distribution approach. For all cases, the cell current is equal to 60 A and the potential of the cathode is fixed to zero.

No slip conditions are applied on all walls of the cell, for the continuous and disperse phases. The electrolyte surface is considered as an outlet, which is modelled as a zero shear stress for the continuous phase. The dispersed phase is considered to flow out of the cell at

the same rate as it reaches this outlet surface. This condition is consistent with the experimental conditions. As a matter of fact, a negative pressure condition (-3386 Pa) is imposed above the surface of the electrolyte to avoid any chlorine leakage from the reactor.

The two-phase flow was solved using COMSOL Multiphysics version 5.2 in a stationary mode. All simulations were performed on Intel(R) Core(TM) i7-4900MQ CPU @ 2.80 GHz.

For the sake of validation of two-phase flow, the published case of magnesium electrolysis, done by Liu et al.[8], was considered and the agreement observed actually validated the approach, see Fig 4-2.

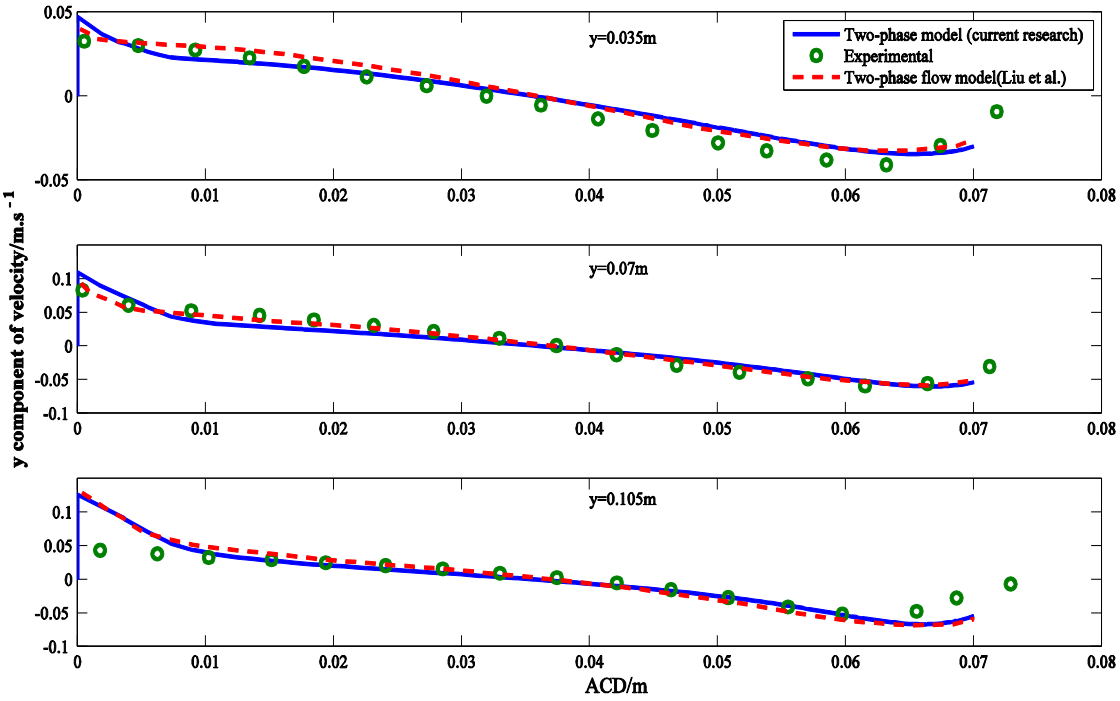

Fig 4-2 Resulting velocity field from a magnesium production cell: comparison between experimental, current two-phase flow model and two-phase flow model of Liu et al., at differentlevels from the bottom of the cell

4.4 Results and Discussion

The results are presented in four sections. In the first two sections, the effects of the diaphragm length and position on the electric and flow fields are shown, the diaphragm being considered as a non-porous wall. In the third section, the effect of the diaphragm porosity on the electric field is presented. Finally, building on the new knowledge generated by these analyses, a best-simulated case is introduced in the last section, with the objective to minimize the cell voltage, i.e. energy consumption.

In some of the figures presented in the next sections, the y-axis either presents the anode or cathode length, the origin of the anode being considered to be at the bottom corner and while the origin of the cathode is considered to be at its bottom.

4.4.1 Effects of the Diaphragm Length on the Velocity and Electric Fields

In an electrolysis cell, the total cell voltage is the sum of the equilibrium potential (approx. 3.6 V in the Li electrolysis cell), ohmic, kinetic and transport overpotentials[68]. In the concentrated LiCl-KCl electrolyte, the transport overpotential is negligible because the concentration of all species at the electrodes are close to their bulk concentration. The ohmic overpotential is the sum of the electrolyte ohmic drop and the bubble layer overpotential [9]. Fig 4-3 presents the effect of the diaphragm length on the cell voltage, ohmic and anodic kinetic overpotentials. The cathodic kinetic overpotential, which is less than -50 mV for all simulated cases, can be ignored when compared to other potential drops. According to Fig 4-3, the total cell voltage, i.e. energy consumption, and ohmic overpotential are higher when the diaphragm is longer while the kinetic overpotential is almost constant over the whole range considered. This behavior is due to the effect of the diaphragm, which is not permeable vis-a-vis ions mass transfer. In fact, the diaphragm blocks the passage of all ions, as a result, the ions should bypass the diaphragm to transfer from the anode to the cathode or vice versa, see the vectors in Fig 4-4. The longer is the diaphragm, the larger is the distance traveled by the ions to reach the electrodes. In other words, the diaphragm introduces an extra ohmic voltage drop, which is closely linked to

the diaphragm length, as one should expect. The former result can be concluded from the voltage contours, presented in Fig 4-4.

Furthermore, the velocity distribution inside the cell without a diaphragm shows that the electrolyte circulation lead the chlorine bubbles directly to the cathode, increasing the risk of back reaction between the chlorine and produced lithium, see Fig 4-5. On the other side, when a diaphragm is used, this circulation pattern is limited to the region between the anode and the diaphragm, even when a short diaphragm is used.

It is worth to mention that the maximum electrolyte velocity presented in Fig 4-5 is more than twice of that presented in the chapter three. However, it is close to the calculated bubbles terminal velocity, 0.29 m/s. In fact, Fig 4-5 shows the result for two-phase flow while in the previous chapter, a one-phase flow with a moving wall anode was used to represent the influence of the upward movement of the bubbles. If the drag force is neglected in the two-phase flow model, the results for the velocity distribution become similar to that of one-phase flow [9]. Their simplification would have been more realistic if the drag force between the moving wall and electrolyte would have been added to the equations representing the one-phase flow model.

The part of the anode and cathode facing the diaphragm is less accessible to the ions; consequently, less current is transferred from the top parts of the electrodes, see Fig 4-6 and Fig 4-7. It is then logical to find the highest current density at the bottom corner of the anode and at the cathode where it is facing the diaphragm bottom. It can be concluded from Fig 4-6 and Fig 4-7 that the diaphragm deteriorates the current density distribution along the electrodes, which can have short and long term consequences. As a matter of fact, the performance and lifetime of the cell is often improved by a uniform current density distribution along the electrodes.

Finally, by comparing the energy consumption of the cell with different diaphragm lengths, it is possible to conclude that a smaller diaphragm design is more suitable because it keeps its blocking effect and reduces the risk of back reaction while minimizing the energy consumption. Fig 4-8 shows that even with the use of a short diaphragm, 1 cm in

the case illustrated, the volume fraction of the bubbles at the surface of the cathode approaches zero.

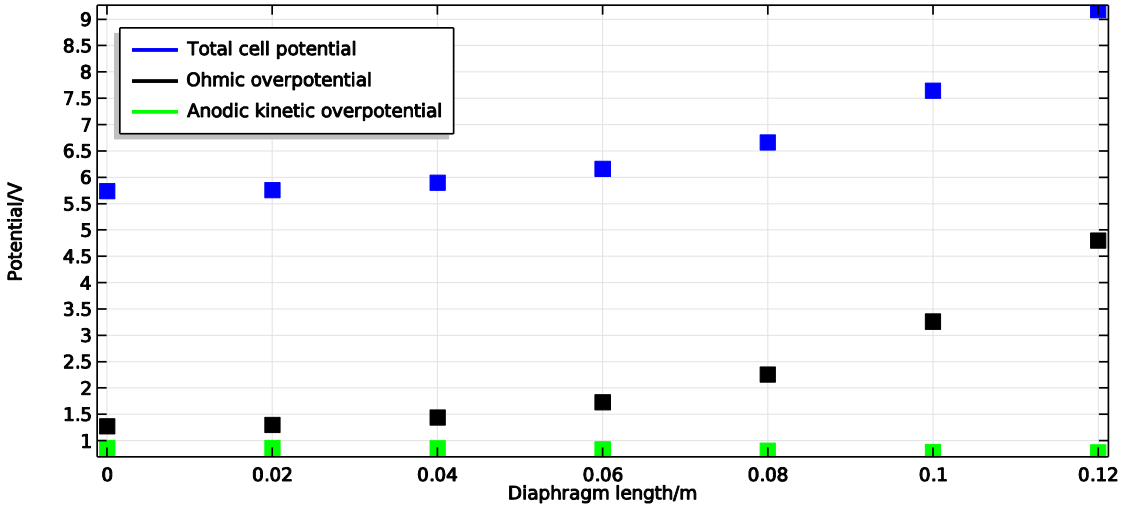

Fig 4-3 Total cell potential, ohmic and kinetic overpotential for the simulation with different diaphragm lengths

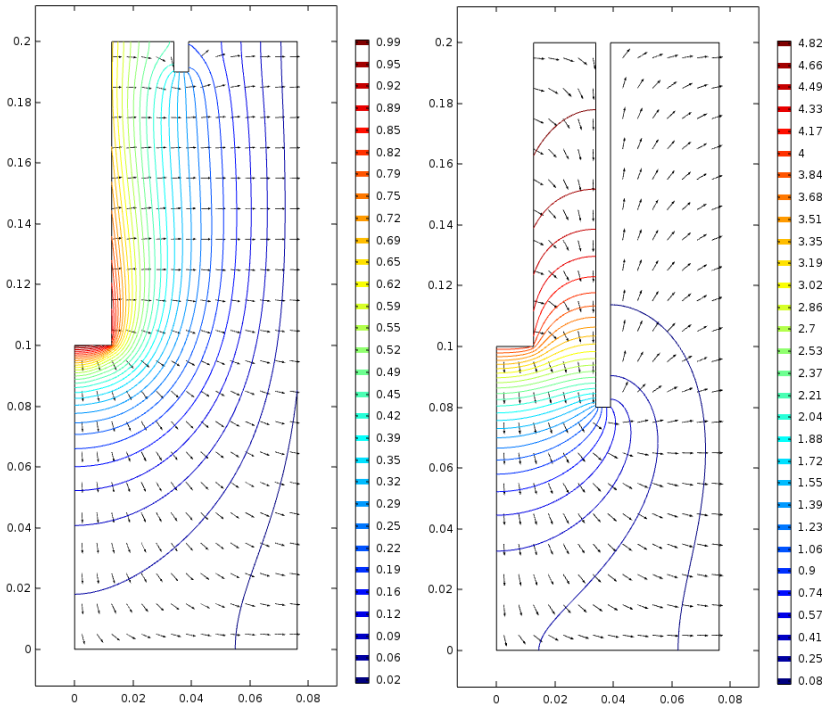

Fig 4-4 Voltage contours and normalized current density vectors inside the electrolyte: a) with a diaphragm length of 0.01m b) with a diaphragm length of 0.12m

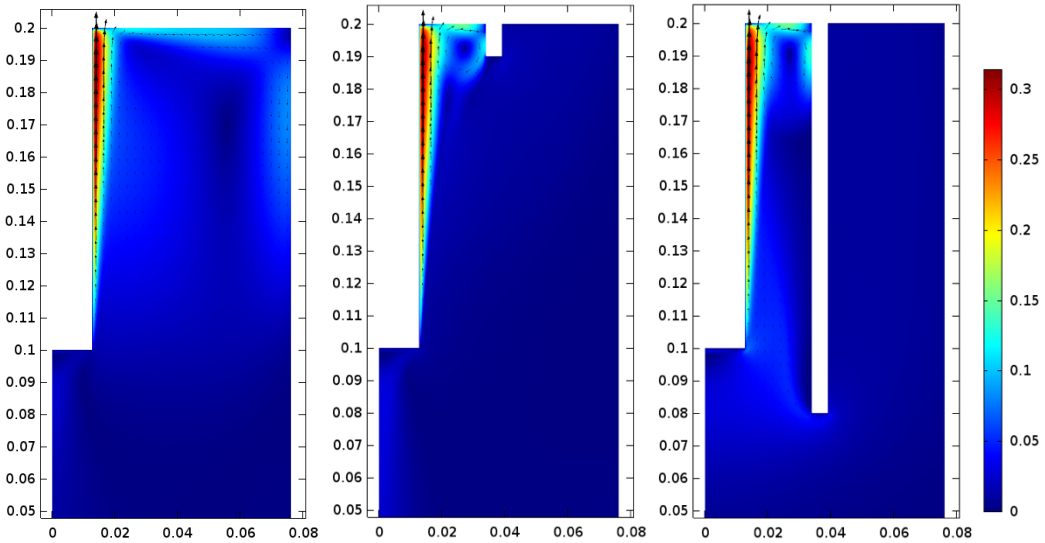

a b c

Fig 4-5 Velocity distribution/m s^{-1} of the liquid phase inside the electrochemical cell: a) without diaphragm, b) with a diaphragm length of 0.01m, c) with a diaphragm length of 0.12m

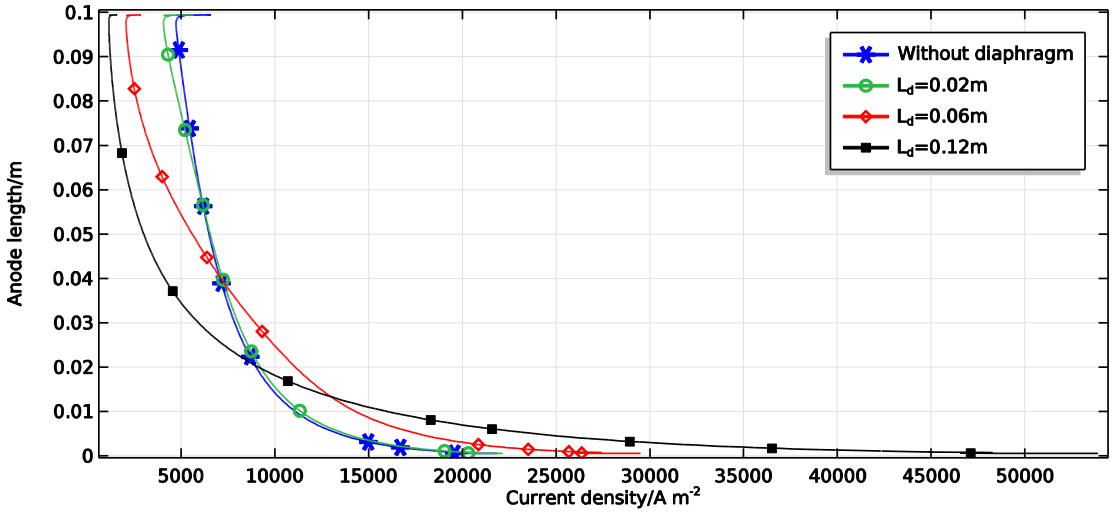

Fig 4-6 Electrolyte current density magnitude along the anode for simulations with different diaphragm lengths

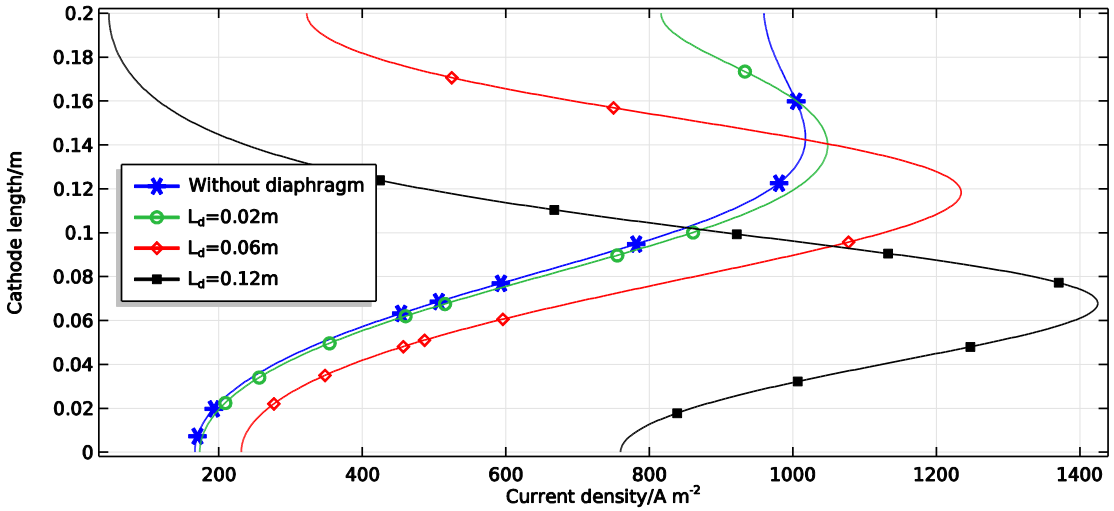

Fig 4-7 Electrolyte current density along the cathode for simulations with different diaphragm lengths

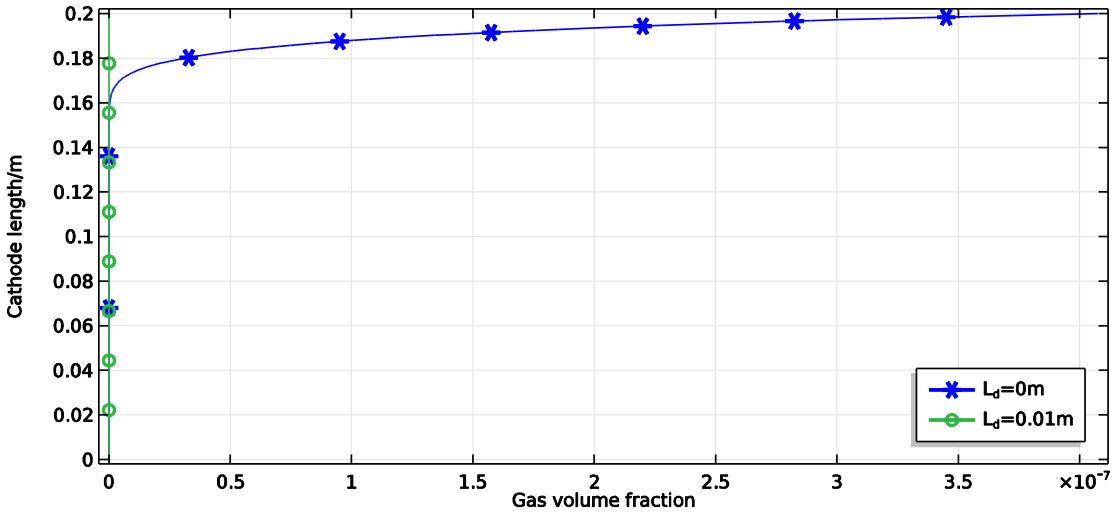

Fig 4-8 Gas volume fraction distribution along the cathode for the cells: in blue without diaphragm and in green with a diaphragm length of 0.01 m

4.4.2 Effects of the Diaphragm Position on the Velocity and Electric Fields

For this section, four cases with different diaphragm positions have been considered, with two cases having bigger anode to diaphragm distance (ADD) than the base case and one with a smaller ADD. ADD has noticeable effects on the cell voltage and current distributions due to the influence of ADD on the velocity and concentration fields. In fact, the diaphragm separates the cell into two regions. The first region, located between the anode and diaphragm, is turbulent due to the entrainment of the electrolyte by the chlorine bubbles. The second region, located between the diaphragm and cathode, is a much quieter region characterized by a laminar regime. The electrolyte circulation in the turbulent region is at the origin of a pumping effect syphoning the electrolyte from the laminar region at the bottom of the diaphragm. The pumping intensity is higher when the diaphragm is closer to the anode, see Fig 4-9. On the other side, the farther the diaphragm is from the anode, the larger is the turbulent region. The ions mass transfer in the turbulent region is faster due to the eddy diffusivity. According to the charge conservation, considering the effect of both diffusion and migration, the electrolyte overpotential decreases when the diffusivity increases. As a result, the bigger ADD gives a lower total cell voltage and ohmic overpotential, see Fig 4-10. Moreover, the diaphragm position changes the current distribution at the surface of the electrodes, see Fig 4-11 and Fig 4-12. The maximum local current density is higher at the anode and lower at the cathode when ADD is smaller. In fact, when the diaphragm is closer to one of the electrodes, less ions can reach the upper part of the electrode due to the blocking effect of the diaphragm. Therefore, at a smaller ADD, more current needs to pass close to the bottom corner of the anode, see Fig 4-11. On the contrary, for a bigger ADD, when the diaphragm is closer to the cathode, more current need to pass from the surface of the cathode facing the bottom of the diaphragm, see Fig 4-12.

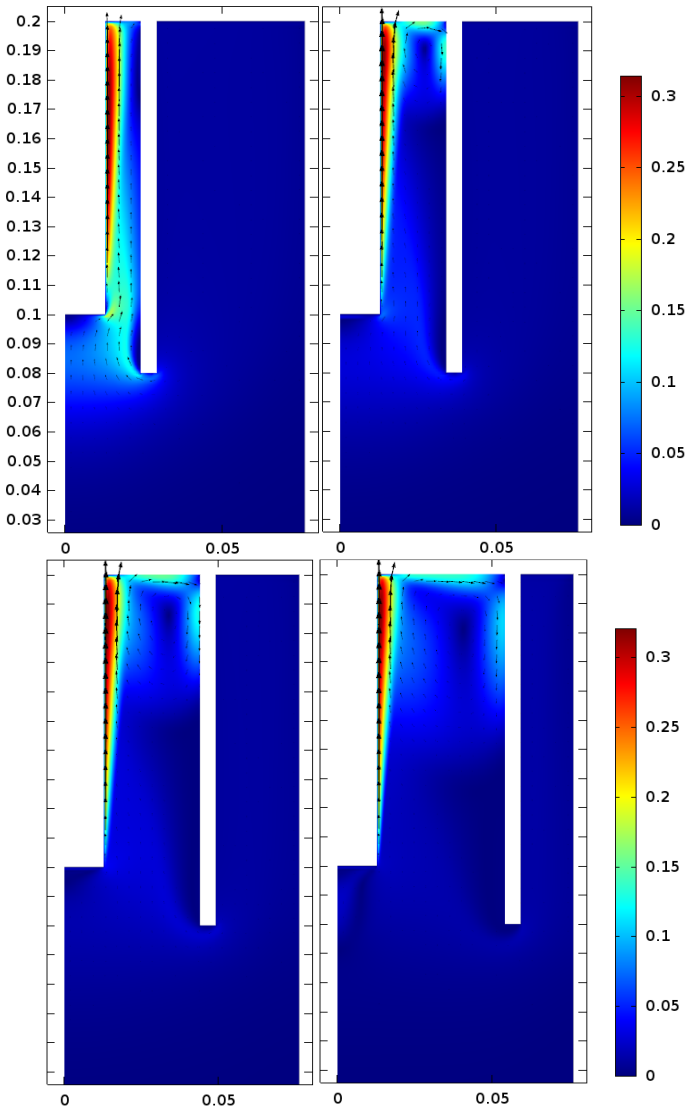

Fig 4-9 Velocity distribution/m s^{-1} of the liquid phase for cells with different ADD

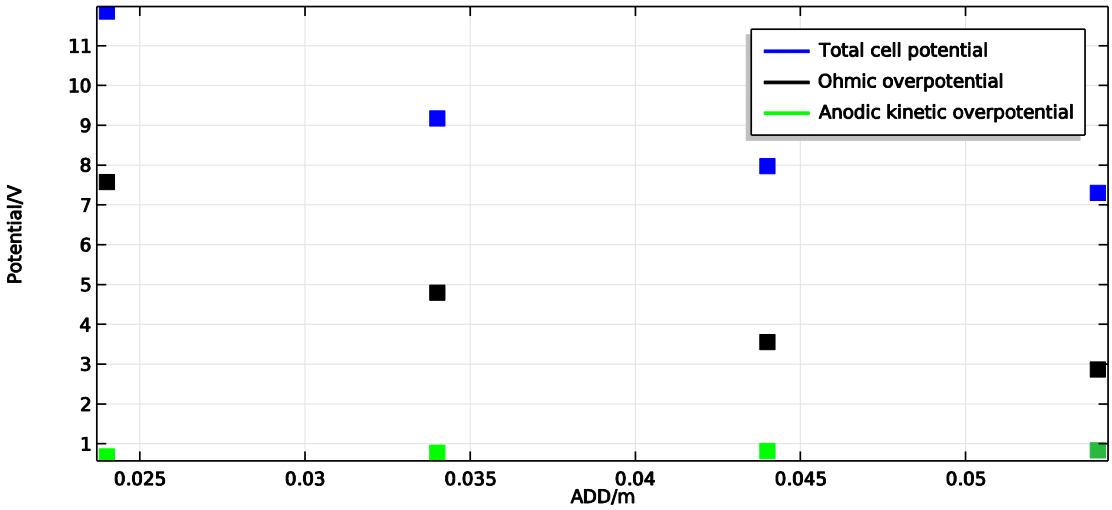

Fig 4-10 Total cell potential, ohmic and kinetic overpotential for simulations with different ADD

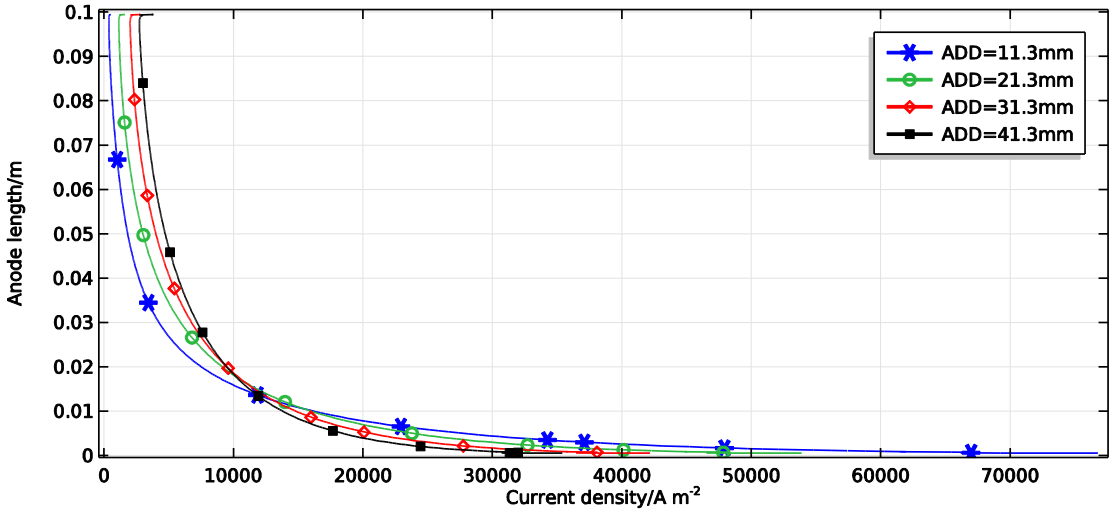

Fig 4-11 Electrolyte current distribution at the surface of the anode for simulations with different ADD

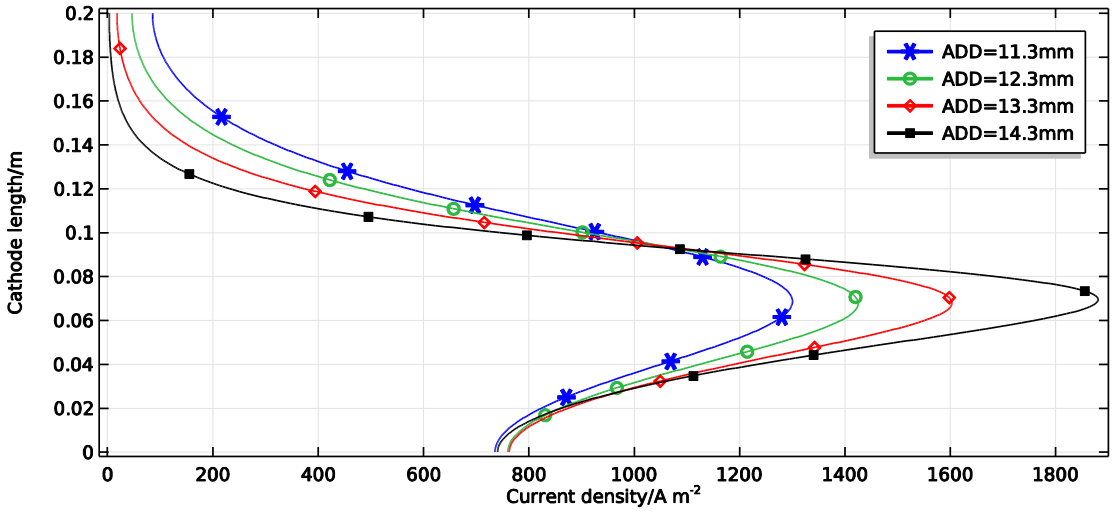

Fig 4-12 Electrolyte current distribution at the surface of the cathode for simulations with different ADD

4.4.3 Effect of the Porosity on the Electric Fields

In Fig 4-13, the effect of the diaphragm porosity on the total cell voltage is presented. In these cases, the length of the diaphragm and its distance from the anode (ADD) are kept the same as those of base case. As expected, the total potential, i.e. energy consumption, decreases when the porosity of the diaphragm increases. In fact, the larger the porosity, the higher the ions mass transfer through the diaphragm. However, a very porous material is intrinsically more fragile and sensitive to cracking problems. The design of such a component might thus be constrained by a compromise between strength and ions diffusivities.

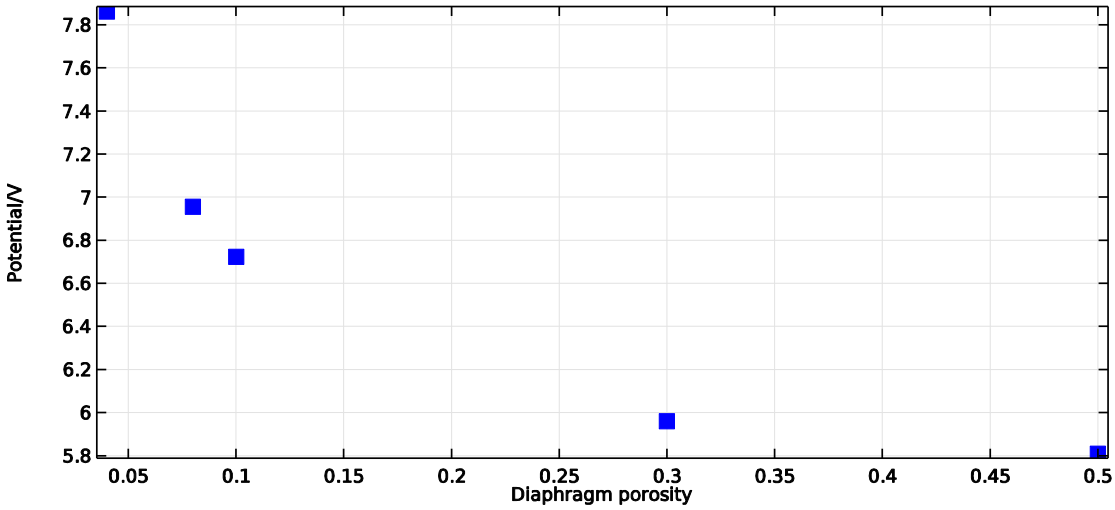

Fig 4-13 Total cell potential for simulations with different diaphragm porosities

4.4.4 Best Case

According to the modeling results, the best position for the diaphragm is at large ADD and its optimum length is as short as possible, long enough to prevent the circulation of chlorine gas from the anode to the cathode. The diaphragm for the best simulated case is according to the following:

- the diaphragm is 1 cm long,
- its position is at 1/3 of the anode-cathode distance, from the cathode,
- and its porosity equals to 0.5.

The total cell voltage for such a case is 5.7 V, a value that is remarkably lower than the voltage drop estimated from the base case (9.5 V). Base on the equations below, the energy consumption of the best simulated case becomes 20 kWh/kg Li.

$$\text{Energy consuption } \left(\frac{\text{kWh}}{\text{kg Li}}\right) = [\text{total cell voltage} \times \text{Current}]\ (\text{W}) \times \left(\frac{\text{Kg Li}}{\text{hour}}\right)^{-1} \times 10^{-3}\left(\frac{\text{KW}}{\text{W}}\right) \quad (4\text{-}18)$$

Where:

$$\frac{\text{Kg Li}}{\text{hour}} = \frac{\text{I}}{\text{F}}\left(\frac{\text{mol}}{\text{s}}\right) \times \text{M}_{\text{Li}}\left(\frac{\text{g}}{\text{mol}}\right) \times 3600\ \left(\frac{\text{s}}{\text{hr}}\right) \times 10^{-3}\left(\frac{\text{Kg}}{\text{g}}\right) \quad (4\text{-}19)$$

In other words, 40% of the energy consumed in a lithium production cell can be saved by optimizing the diaphragm position, length and porosity.

4.5 Conclusions

A new finite element multiphysic model has been developed and used to simulate a lithium production cell and assess the influence of some important design parameters like the length and position of the diaphragm on the energetic performance of the cell. The necessity of having a diaphragm in the cell is important to prevent the back reaction between chlorine and liquid lithium, by blocking the path of Cl_2 bubbles from the anode to cathode. However, it introduces an additional ohmic drop in the cell.

The cell is simulated with the help of two different models: one-phase and two-phase models. The one-phase flow model is coupled with a tertiary current distribution to study the effect of the aforementioned design parameters on the potential field and current distributions along the electrodes. The total cell voltage, or cell energy consumption, is lower when the diaphragm is shorter, located farther from the anode, and with an optimum porosity. Moreover, in these conditions, the current distribution at the anode gets more uniform, possibly resulting in longer life time.

The results of the two-phase flow model showed that even when a short diaphragm is used, for instance 0.1 cm long, it can block the path of Cl_2 gas bubbles from the anode to the cathode. Lastly, a best-case scenario, comprising a short porous diaphragm located far from the anode, has been simulated. The energy consumption of this best case is 40% lower than that of the base case.

Finally, the results of this research are not only useful for improving the design of lithium production cells, they can also be extended and applied to the study of other molten salts electrochemical cells equipped with diaphragms.

4.6 Nomenclature

A	Area (m^2)
C_D	Drag coefficient
c	Concentration (mol m^{-3})
D_{eff}	Effective diffusion coefficient ($m^2\ s^{-1}$)
d_b	Bubble diameter (m)
F	Faraday's constant ($A\ s\ mol^{-1}$)
F_b	Volume force (kg m s^{-2})
F_D	Drag force (kg m s^{-2})
g	Gravity acceleration constant (m s^{-2})
i	Local current density (A m^{-2})
i_0	Exchange current density (A m^{-2})
k	turbulent kinetic energy (m^2 s^{-2})
L	Length (m)
M	Molecular weight (kg mol^{-1})
N	Ions flux (mol m^{-2} s^{-1})
n	Normal vector
p	Pressure (kg m^{-1} s^{-2})
R	Gas constant (J K^{-1} mol^{-1})
Re	Reynolds number
T	Temperature (K)
T_k^{turb}	Stress tensor (kg m^{-1} s^{-2})
t	Time (s)
u	Velocity magnitude (m s^{-1})
u_m	Mobility (m^2 s^{-1} V^{-1})
u_t	Bubbles terminal velocity (m s^{-1})
V	Velocity vector (m s^{-1})
x	Mole fraction
z	Charge number

Greek letters

α_0	Transfer coefficient
σ	Electrolyte conductivity (S m^{-1})
ϵ	Rate of dissipation of kinetic energy (m^2 s^{-3})
ε	Porosity
η	Activation overpotential (V)
μ	Viscosity (kg m^{-1} s^{-1})
ρ	Density (kg m^{-3})
τ	Tortuosity
φ	Volume fraction
$\emptyset_g$	Bubble coverage

Subscripts and Superscripts

a	Anode
c	Continuous phase
d	Disperse phase
dia	Diaphragm
i	Species i
in	Inlet
h	Hyperpolarization
mean	Mean
mix	Resistive layer
T	Turbulent

CHAPITRE 5 : AVANT-PROPOS

Auteurs et affiliation:

- Elaheh Oliaii: étudiante au doctorat, Université de Sherbrooke, Faculté de génie, Département de génie chimique et de génie biotechnologique.
- Giuliana Litrico : étudiante au doctorat, Université de Sherbrooke, Faculté de génie, Département de génie chimique et de génie biotechnologique.
- Martin Désilets: professeur, Université de Sherbrooke, Faculté de génie, Département de génie chimique et de génie biotechnologique.
- Gaétan Lantagne: Directeur - Recherche et innovation, Hydro-Québec, Varennes, QC J3X-1S1, Canada

Date d'acceptation: À venir
État de l'acceptation: Soumis à l'éditeur du journal
Revue: Electrochimica Acta
Référence: [12]

Titre français: Transport de masse et consommation d'énergie dans une cellule d'électrolyse du lithium

Contribution au document:

Ce travail présente les résultats de la simulation du transfert de masse et de la consommation d'énergie dans une cellule électrolytique de production de lithium sans diaphragme. Un nouvel algorithme de résolution a été développé avec un logiciel de plate-forme ouverte OpenFOAM. Le modèle résultant a été utilisé pour étudier l'impact de la longueur de l'anode sur le comportement de la cellule et en particulier sur les champs de concentration, de potentiel électrique et sur la vitesse.

Résumé français:

Le transfert de masse et la consommation d'énergie dans une cellule d'électrolyse du lithium, appelée cellule à emportement gazeux, ont été étudiés à l'aide d'un nouveau solveur développé avec le logiciel de plate-forme ouverte OpenFOAM. La distribution de vitesse créée par les bulles a été résolue avec un modèle d'écoulement à 2 phases de type Euler-Euler, alors qu'une approche basée sur le modèle k-ε a été utilisée pour résoudre l'écoulement turbulent dans l'électrolyte. La distribution non uniforme des bulles et le recouvrement gazeux à l'anode sont influencés par la distribution de la densité de courant anodique. La forte dépendance entre le champ de potentiel, la distribution de courant et la concentration des ions a été prise en compte dans le modèle. Le nouveau solveur a été développé et validé en prenant en compte les fortes interactions entre les différents phénomènes physico-chimiques à l'intérieur de la cellule tout comme à ses frontières. Ce nouveau modèle est général et peut être utilisé pour la simulation des champs électriques et de concentration à l'intérieur de la plupart des cellules d'électrolyse.

La comparaison entre les résultats de simulation d'une cellule à emportement gazeux avec deux longueurs d'anode montre d'importants avantages à faire correspondre la position et la taille de l'anode avec celles de la cathode. La circulation de l'électrolyte devient plus importante ce qui réduit le temps de résidence du lithium métallique dans la cellule. De plus, la distribution de courant devient plus uniforme et la consommation d'énergie en est réduite.

5 Mass transport and energy consumption inside a lithium electrolysis cell

Abstract

Mass transfer and energy consumption of a lithium electrolysis cell, called gas-lift cell, is investigated with a newly developed solver in open source package, OpenFOAM. The velocity distribution introduced by the bubbles, is solved by an Euler-Euler two-phase flow model, while the k-epsilon approach is used to solve the electrolyte turbulent flow. The non-uniform distribution of the bubbles and the gas coverage at the anode are influenced by the current density distribution. The strong dependence between the potential field, current distribution, and ions concentration is taken into account. The new solver is developed and validated, considering the strong coupling between different phenomena inside of the cell and at its boundaries. This new model is general and can be used for the simulation of the concentration and electric fields inside any electrolysis cell.
Furthermore, the comparison between the simulation results of the gas-lift cell with two different anode lengths shows important advantages to match the position and size of anode and cathode. In such a configuration, the electrolyte circulation gets stronger; therefore, the residence time of metallic lithium is shorter. Moreover, the current distribution is uniform and the energy consumption is reduced.

5.1 Introduction

Lithium has the lowest density among all metals in the standard conditions. This property make it very popular for different industrial applications, the most important being the fabrication of the electrodes of rechargeable batteries. Sharp growth of lithium applications in last decades shows the importance of the production process and the need to develop new tools for its analysis and optimization in terms of purification, efficiency and energy consumption.

Lithium is commercially produced by the electrolysis of lithium chloride [51,69], mixed with potassium chloride to decrease the melting point of the electrolyte [70]. More

precisely, the electrolyte of the lithium electrolysis cell contains 60% LiCl and 40 % KCl, its temperature is kept around 450 °C [71]. In such a cell, lithium and chlorine are produced respectively at the cathode and anode through the following reactions:

$$Li^+ + e^- \rightarrow Li\ (liquid)$$

$$2Cl^- \rightarrow Cl_2(gas) + 2e^-$$

Both products are lighter than the electrolyte and escape toward the free surface. Therefore, they can react back if the contact time is long enough. Back reaction can be prevented in two ways:

1. By using a diaphragm to separate the anodic and cathodic parts and prevent the direct contact between Li and Cl_2,
2. By decreasing the residence time of the liquid lithium in the cell

Some patents present cell designs with diaphragms [36,40,57] but none of these patents investigate the impact of their presence on the cell energy consumption, which was done recently by Oliaii et al. [9,10]. These authors analyzed the mass transport and energy consumption inside a lithium electrolysis using a commercial software. For the simulation of electric and concentration fields, Oliaii et al. used a one-phase flow model. While the circulation of electrolyte results from the upward movement of the anode with the same velocity as terminal velocity of the bubbles [9,10]. They concluded that the diaphragm prevents the back reaction by blocking the passage of chlorine from the anode to the cathode but it increases noticeably the energy consumption of the cell.

Additionally, some patents exploited the second solution where a modified cell geometry is helping to prevent the back reaction. For example, in the cell designed by Muller et al., the metallic lithium is withdrawn from the cell through a siphon pipe [72]. Unfortunately, very scarce information can be found in these patents and it is difficult to assess the impact of these concepts on energy consumption.

The numerical simulation of the lithium cell can help to overcome the lack of knowledge in this field. However, two main obstacles make the simulation very challenging

- The lack of experimental data: the measurement environment is extremely harsh due to high temperatures and corrosiveness of materials used, which makes it particularly difficult for experiment analysis,
- The strong coupling between concentration, electric and two phase flow fields

According to authors' knowledge, no study has been published that investigates mass transfer and energy consumption inside a diaphragmless electrolysis cell while considering the coupling between the aforementioned fields. This work is presenting original results showing the impact of the design and flow conditions on the energetic performance of the cell.

In the present work, a diaphragmless lithium electrolysis cell, named gas-lift cell, is modeled by developing an open access C++ toolbox called OpenFOAM. In addition, the effect of the anode length on the velocity and cell energy consumption has been investigated. The solver, called POTisoFOAM had been previously used and validated for the mass transfer analysis inside a copper electroplating cell by some of the authors [73]. Then it has been developed for the simulation of electric and concentration fields in a molten salt electrolysis cell through the present work. The new developed solver can be used for the analysis of concentration, electric and velocity fields in many different electrolysis cells with different geometries, electrolyte and operating conditions. Moreover, the results of this paper can be generalized to other designs of lithium electrolysis cells, such as lithium electrolysis cell proposed by Muller [72], Verdier [39] and Grosbois [37].

5.2 Physical Model

An experimental setup representing the lithium electrolysis cell had been designed and tested at Hydro-Quebec by K. Amouzegar and S. Harrison in 1996. The schematic of the experimental setup, known as gas-lift cell, is shown in Fig 5-1a. It has a relatively small anode to cathode distance (ACD), 6 mm. The idea behind this cell design is to make sure that the electrolyte velocity, entrained by the bubbles, is sufficient to pump the metallic

lithium droplets, produced at the cathode, out of the electrolysis zone, before the chlorine bubbles reach them. In the gas-lift configuration, the diaphragm is placed outside of the interpolar area, behind the cathode and above, to facilitate the collection of the chlorine gas.

To melt the electrolyte, the cell was placed in a tube furnace equipped with a temperature controller. Therefore, for the simulation, the assumption of isothermal is not far from the reality of the experimental cell. Moreover, the cell pressure was kept negative to prevent any chlorine leakage and a water jet pump evacuated the chlorine gas from the cell to an absorber.

The cell is divided in two parts: the bottom part contains the electrolyte and the top is filled with an inert gas. The latter does not have any effect on the mass transfer and energy consumption of the cell; therefore, it is not taken into consideration. Moreover, due to the cylindrical shape of the cell, the simulation is applied to a 2D-axisymetric wedge with a central angle of 5° inside the electrolyte. A side view of the numerical domain is shown in the Fig 5-1b. Based on the axis system shown, the right and the upper directions are taken as the positive directions for the x and y axis respectively. This detail will have an impact on the direction of the mass fluxes presented later in the analysis of results.

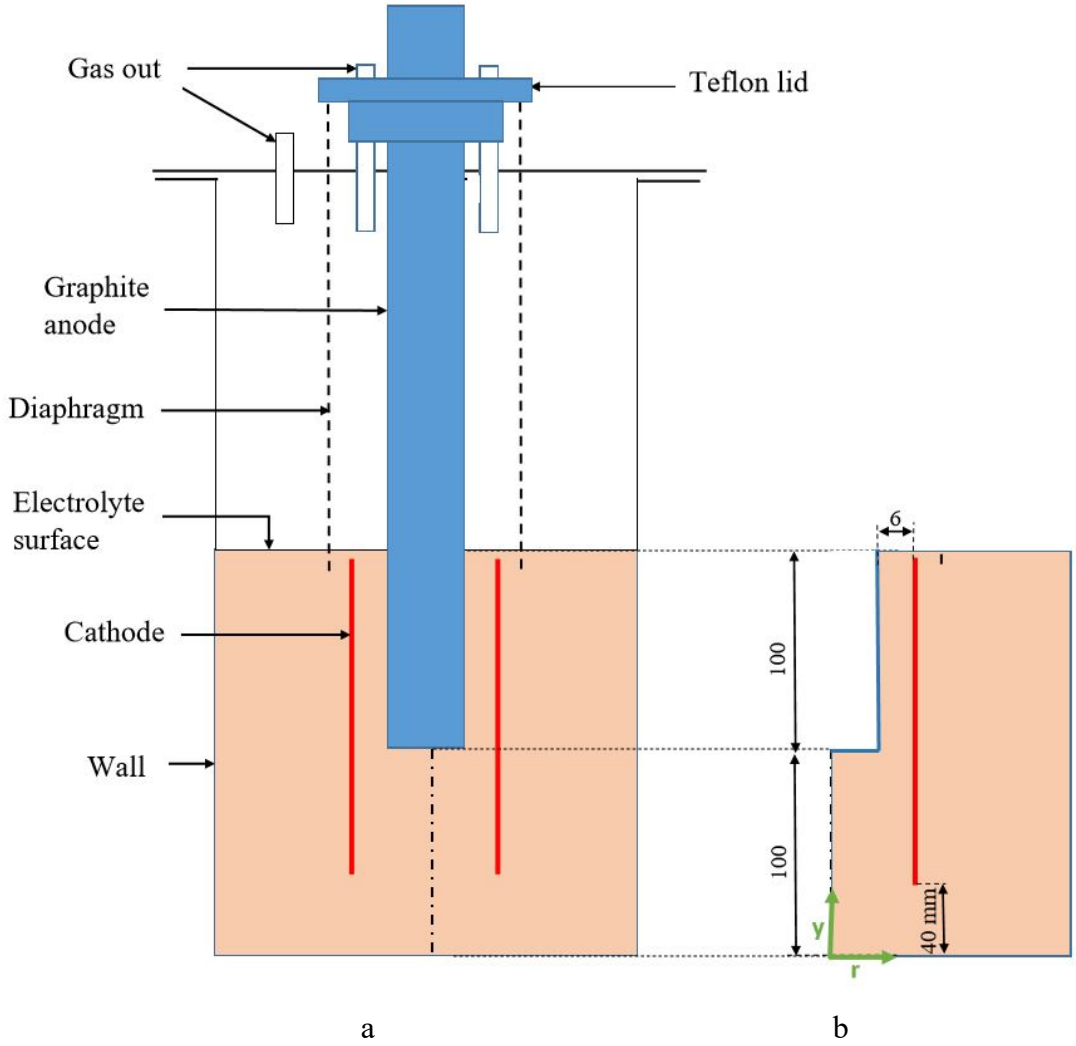

Fig 5-1. Schematic illustration of a) experimental Gas-lift cell b) simulated part

The material properties and kinetic parameters can be found in the work of Oliaii et al.[9]. The operating parameters are given in Table 5-1. The high current density, as used in the present cell, is typical for many molten salt electrolysis cell such as magnesium [33] , cerium [74] and aluminum cells [14].

Table 5-1 Operating parameters used in simulation

Initial concentration of K^+/kmol m^{-3}	10.8	Initial concentration of Li^+ /kmol m^{-3}	19.2
Initial concentration of Cl^- /kmol m^{-3}	30	Temperature/K	723
Current/A	120	Anodic current density/A m^{-2}	13800

5.3 Mathematical model

As mentioned before, there is a strong coupling between the electric, velocity and concentration fields. In fact, the electrolyte velocity depends on the bubbles distribution at the surface of the anode, which is related to the anodic current distribution. All of which affect the concentration of the ions.

The diagram in Fig 5-2 shows the solving steps adopted in this work. The parameters, shown in hexagons, are the results of each simulation step, presented with more details in the results and discussion section. The equations, used to solve the problem are explained in the following sections. The cell is considered as a batch reactor within which the electrolyte is confined. The simulation of two-phase flow reaches steady state after 60 s.

The model starts by solving the electric field through a secondary current distribution. The resulting anodic current density rules the bubbles distribution at the surface of the anode in the solution of the two-phase flow model.

The obtained electrolyte velocity is used in the convection term of Nernst-Planck equation.

The potential distribution results from the charge conservation equation. Then the gradient of potential is multiplied by the electrolyte conductivity to give the migration component of the Nernst-Planck equation. The electrolyte conductivity depending on the ions concentration, changes over time.

At the end, the internal loop at the bottom of Fig 5-2, in the green dash line frame, which expresses the intimate coupling between concentration and electric fields, is repeated for each time step until a tolerance of 10e-7 is reached for the resolution of each variable. Then the results of are used for the next time step iteration.

The two-phase flow model simulation is not included in the correction loop because at the anode, the current density is fixed, therefore its distribution does not change with time, i.e. the bubbles distribution is fixed.

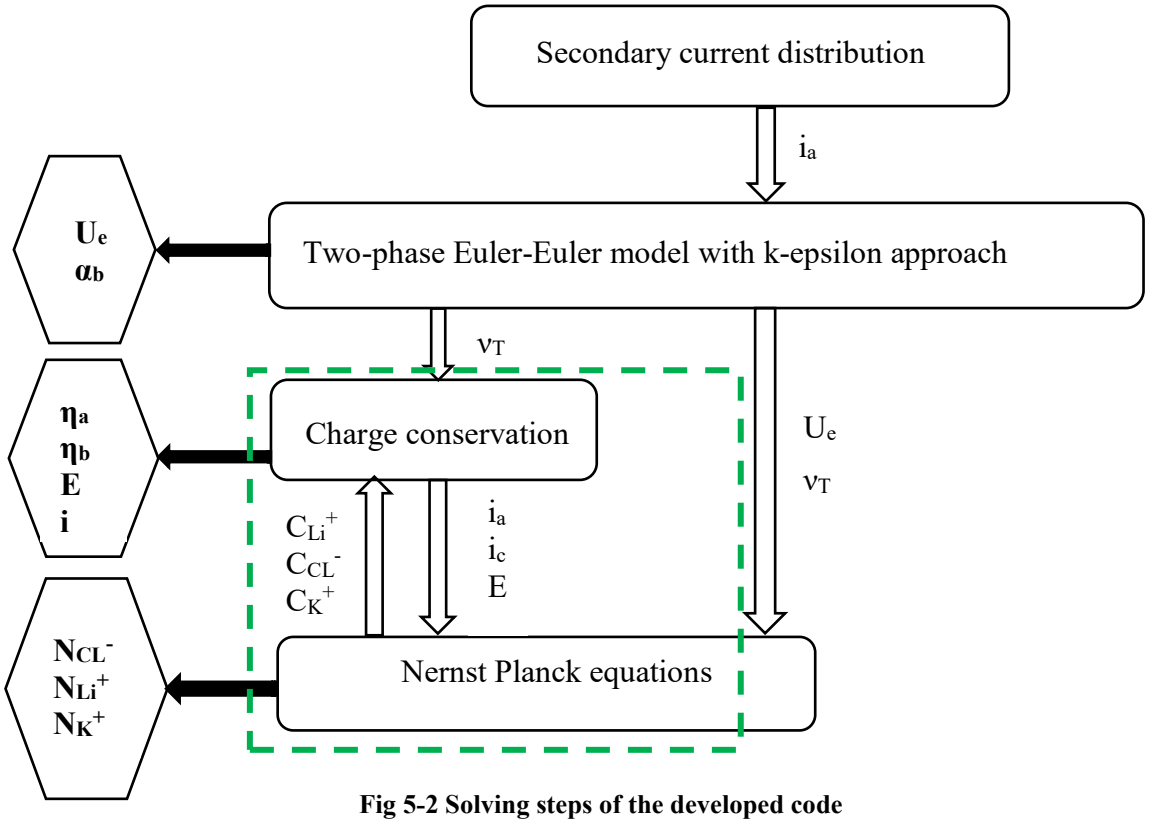

Fig 5-2 Solving steps of the developed code

The equations have been solved making use of OpenFOAM 2.3.1 with a processor Intel® Core TM i7-4900MQ CPU @ 2.80GHz × 8. The simulation of two-phase flow takes approximately two days to reach the steady state. Then, three days are needed to have the solution of tertiary current distribution for 1 h of simulation time.

Two different mesh sizes have been used for the simulation of flow and concentration fields:

- Coarse mesh: the two-phase flow has been simulated with the use of k-epsilon turbulent model and wall functions have been applied at the walls [75,76], see Fig 5-3 A and C.
- Fine mesh: the simulation of tertiary current density strongly depends on the concentration and potential gradient, as a result, a smaller mesh is needed to

maintain a good accuracy and facilitate the convergence of the solution. After amesh independency analysis on the current density and potential distribution, the mesh presented in Table 5-2 has the best tradeoff between number of cells and accuracy, see Fig 5-3 B.

Therefore, the electrolyte velocity and turbulent kinematic viscosity, obtained from two-phase flow simulation, are mapped from the courser mesh to the finer mesh, before being used in the tertiary current distribution.

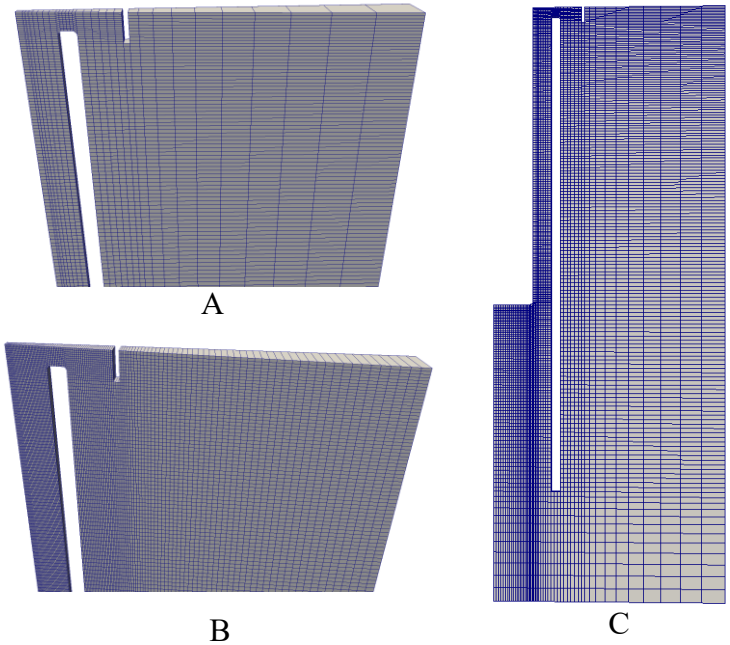

Fig 5-3 2D axi-symmetric meshes A) top part of course mesh B) top part of fine mesh C) mesh for complete geometry

Table 5-2 shows the properties of the two aforementioned meshes.

Table 5-2 Meshes properties

	Numerical domain dimensions/mm	Hexahedra cells	Prisms cells	Max skewness	Max aspect ratio
Course mesh	76x200x6.6	7015	83	0.97	14.5
Fin mesh	76x200x6.6	24649	96	0.85	13.7

5.3.1 Flow field

A two-phase flow model is developed to investigate the velocity distribution and bubble volume fraction in the cell. The two-phase flow can be predicted with two different approaches: lagrangian or eulerian models. In the former, the bubbles are treated as discrete particles while in the latter one they are considered as a continuum. Lagrangian method is suited when the bubbles are clearly a dispersed phase. On the other hand, the eulerian model is more suitable if the gas volume fraction is high (more than 10%) and the bubbles can be treated as a continuous phase [77,78].

In the present lithium electrolysis cell, the two vertical electrodes delimit a zone with high gas volume fraction, as a result of the chlorine gas produced at the anode. Therefore, the Euler-Euler model has been chosen for the simulation, an approach already validated for another lithium cell [10] and a simplified magnesium cell [8,20,22]. In this model, the Navier-Stokes equations are solved for each phase:

Average continuity and momentum equations:

$$\partial \alpha_i / \partial t + \nabla . (\alpha_i \boldsymbol{U}_i) = 0 \qquad \text{i=e (electrolyte, i.e. liquid); b (bubble; i.e. gas)} \tag{5-1}$$

$$\partial (\alpha_i \boldsymbol{U}_i) / \partial t \ + \nabla . (\alpha_i \boldsymbol{U_i U_i}) = -\alpha_i / \rho_i \ \nabla p + \nabla . (\alpha_i \boldsymbol{R}_i^T) + \alpha_i \boldsymbol{g} + \boldsymbol{F}_b / \ \rho_i \tag{5-2}$$

$$\alpha_e = 1 - \alpha_b \tag{5-3}$$

Where $\boldsymbol{R}_i^T$, the turbulent Reynolds stress, is defined as follow:

$$\boldsymbol{R}_i^T = (\nu_i + \nu_{T,i})(\nabla \boldsymbol{U_i} + (\nabla \boldsymbol{U_i})^T - 2/3 \ (\nabla . \boldsymbol{U_i})^T \boldsymbol{I}) \tag{5-4}$$

And $\mathbf{F}_b$, body force is defined by three contributions: lift, drag and virtual mass forces. The lift force is perpendicular to the bubbles motion and has an effect on radial distribution of bubbles. The virtual mass force is resulting from the acceleration or deceleration of the bubbles on the electrolyte. It is important in the transient evolution but not at the steady state. However it has a positive effect on the stability of the solution [79] . The drag force is a force in the opposite direction of the bubbles movement. Among these three forces, only the lift force is not taken into account, as its effect in the model has shown to be negligible. As a matter of fact, the authors ran the same simulation with and without this

contribution and did not notice any remarkable effects on the main flow. The same conclusion was obtained by the authors Li et al. in the simulation of Down cell [30].

The drag force, $\mathbf{F}_D$, is expressed as:

$$\boldsymbol{F}_D = 3\, C_D \alpha_b \rho_e |\boldsymbol{U}_b - \boldsymbol{U}_e|(\boldsymbol{U}_b - \boldsymbol{U}_e)/(4\, d_b) \quad (5\text{-}5)$$

The bubbles are assumed to have a fixed diameter of 1.5 mm , this value is chosen based on an experimental work on the magnesium cell, where the same environmental conditions as a lithium cell are present [8,10,80]. Since bubbles are considered as rigid spheres, the Schiller-Naumman correlation has been chosen for the calculation of the drag coefficient [54,81]:

$$C_D = \begin{cases} 24\,(1 + 0.15Re^{0.687})/Re & Re \le 1000 \\ 0.44 & Re > 1000 \end{cases} \qquad Re = d_b \rho_e |\boldsymbol{U}_e - \boldsymbol{U}_b|/\mu_e \quad (5\text{-}6)$$

Virtual mass force, F_{vm}, is solve through the model below:

$$F_{vm} = -C_{vm} \rho_b \alpha_e (D\boldsymbol{U}_e/Dt - D\boldsymbol{U}_b/Dt) \quad (5\text{-}7)$$

Where C_{vm}, the virtual mass coefficient is 0.5.

Furthermore, the k-epsilon approach is used to solve the turbulent flow in the electrolyte, which has been widely used for the simulation of many bubbly turbulent flows [76,82–88]. The turbulence of the gas phase is neglected and no particle-particle interaction is considered [89]. The turbulent kinetic energy, k, and the turbulent dissipation rate, ϵ, are given by Eqs. 8 and 9 respectively:

$$\partial(\alpha_e k)/\partial t + \nabla(\alpha_e \boldsymbol{U} k) = \nabla.[\alpha_e(\nu + \nu_T/\delta_k)\nabla k] + \alpha_e P_k - \alpha_e \epsilon \quad (5\text{-}8)$$

$$\partial(\alpha_e \epsilon)/\partial t + \nabla.(\alpha_e \boldsymbol{U} \epsilon) = \nabla.[\alpha_e(\nu + \nu_T/\delta_\epsilon)\nabla \epsilon] + \alpha_e C_{\epsilon 1} P_k\, \epsilon/k - \alpha_e C_{\epsilon 2} \epsilon^2/\, k \quad (5\text{-}9)$$

Where:

$$\nu_T = C_\mu\, k^2/\epsilon \qquad , \qquad P_k = 2\nu_{sum}[\nabla \boldsymbol{U} : (\nabla \boldsymbol{U} + (\nabla \boldsymbol{U})^T)] \quad (5\text{-}10)$$

Where ν_{sum} is the sum of turbulent and laminar viscosities. The constants, $C_{\epsilon 1}$, $C_{\epsilon 2}$, C_μ, δ_k, δ_ϵ are 1.44, 1.94, 0.09, 1, 1.3 respectively. More information about the turbulent model can be found in the books of Mathieu, Pope and Wilcox [90–92].

The properties of all materials are assumed to be constant. Moreover, there is no mass exchange between the two phases. The boundary conditions for the two-phase flow are expressed as below:

Anode: This boundary is an inlet for the gas phase. In fact, the bubbles are the product of the anodic reaction. Their inlet velocity and volume fraction are related to the local current density through Faraday's law and the correlation proposed by Vogt, [10,53,59,67]:

$$U_b = i_a M_{Cl_2} / \left(n\, F\, \rho_{Cl_2} \alpha_{b_a}\right) \tag{5-11}$$

$$\alpha_{b_a} = 0.023\, {i_a}^{0.3} \tag{5-12}$$

Furthermore, the algebraic wall functions relations, used as boundary conditions for the turbulent variables, k, ϵ and ν_T can be found in the books of Lesieur [93], Libby [94], Tennekes and Lumley[95].

Cathode: This boundary is a wall for both phases. Therefore, no slip conditions and wall functions are imposed for the velocity and the turbulent variables [96].

Outlet: This is the interface between the electrolyte and inert gas, where the bubbles go out of the simulated domain. A mixed boundary condition called inletOutlet is imposed for the gas velocity and volume fraction. Such a condition imposes a zero gradient when the flow goes up and a Dirichlet zero value when the flow goes down, thus avoiding reverted flow. A slip boundary condition is considered for the electrolyte velocity at this location.

5.3.2 Concentration Field

Three species are present in the lithium electrolysis cell: lithium, potassium and chloride ions. The concentration of two species is calculated through the mass conservation law, without any homogeneous reactions:

$$\partial c_i / \partial t = \boldsymbol{\nabla}.\mathbf{N_i} \tag{5-13}$$

The Nernst-Planck equation has been considered to represent the ions fluxes, N_i [97]:

$$\mathbf{N}_\mathrm{i} = c_i \mathbf{U} - D^{\mathrm{t}}_{i,eff} \boldsymbol{\nabla} c_i - \mathrm{z_i} F u_i c_i \boldsymbol{\nabla} E_l \tag{5-14}$$

$$D^{t}_{i,eff} = D_{i,eff} + D^{T} \quad (5\text{-}15)$$

Where u_i is the ions mobility, related to the effective diffusivity through Nernst-Einstein equation:

$$u_i = D_{i,eff} / R\,T \quad (5\text{-}16)$$

The eddy diffusivity, D^T, can be considered equal to the turbulent kinematic viscosity when the turbulent Schmitt number is one [9,60–62,97,98]. To take into account the multicomponent nature of the solution, an effective diffusivity, $D_{i,eff}$, is calculated based on the Wilke's correlation[50]:

$$D_{i,eff} = (1 - y_i) / \sum_{\substack{i=1 \\ i \neq j}} \frac{y_j}{D_{ij}} \quad (5\text{-}17)$$

Where D_{ij} is the binary diffusivity, y_i and y_j are the mole fractions of species i and j. As it will be shown in the results section, the mass transfer is dominated by convection in the bulk. As a consequence, the multicomponent diffusion is only playing a minor role and the suggested approach is reasonable.

It might be argued that in such a concentrated solution, the Nernst-Planck equation would not be appropriate. However, the use of the Nernst-Planck equation gives valuable information about the physical process of the electrochemical cell [97]. In the diffusion term, the effect of ions concentration on each ions diffusion coefficient has been considered through an effective diffusion coefficient, solved by the use of Wilke's correlation [9,27]. Moreover, the effect of eddy diffusivity on the diffusion is considered through a total effective diffusion coefficient, which affects the mass transfer and charge conservation equations.

Finally, the concentration of last species is calculated through the electroneutrality:

$$\sum_i z_i c_i = 0 \quad (5\text{-}18)$$

The boundary conditions for the concentration field are as follow:

Anode and cathode: at the electrodes, the total flux of ions for the active species, chloride at the anode and lithium at the cathode, are related to the current density as follow:

At the anode: $N_{Cl^-} = i_a/F$

At the cathode: $N_{Li^+}=i_c/F$

While, the total flux is zero for all inactive species:

At the anode: $N_{Li^+}=0$, $N_{K^+}=0$

At the cathode: $N_{Cl^-} =0$, $N_{K^+}=0$

Outlet and walls: For these boundaries, all species are inactive and consequently the flux of all species is zero.

$N_{Li^+}=0$, $N_{K^+}=0$, $N_{Cl^-} =0$

5.3.3 Electric Field

The electrolyte potential distribution, E_l is solved through the charge conservation equation:

$$\nabla.\left(\left(-F\,\nabla\sum_i z_i D_{i,eff} c_i\right) - F^2\sum_i z_i^2 u_i c_i\,\nabla E_l\right) = 0 \qquad (5\text{-}19)$$

In the Eq. 19, the first and second term describing the current density through diffusion and migration, respectively. In the secondary current distribution approach, used in the first step of simulation, only the current density through migration has been considered, while the concentration of species is assumed to be uniform in the bulk.

The current density in the bulk is obtained from the equation below:

$$i = \left(-F\,\nabla\sum_i z_i D_{i,eff} c_i\right) - F^2\sum_i z_i^2 u_i c_i\,\nabla E_l \qquad (5\text{-}20)$$

The boundary conditions for the electrolyte potential are as follow:

Anode: fixed average current density: i= 13800 A m^{-2}

Cathode: electrode potential , E_s, and equilibrium potential, E_{eq_c} are zero. Therefore, the electrolyte potential is equal to the absolute value of cathodic overpotential through following equation:

$$E_{l_c} = E_{s_c} - E_{eq_c} - \eta_c \qquad (5\text{-}21)$$

Outlet and walls: at these boundaries, the gradient of electrolyte potential is zero.

Additionally, reactions and resistive layer overpotentials, the anodic and cahodic current density distribution results as follow:

- Reactions overpotential

The reaction overpotential has been obtain from the simplified forms of general Butler-Volmer equation. In fact, the concentration overpotential, η_{cons}, presented by Eq. 22 [51,68], is negligible in both anode and cathode because the electrolyte is highly concentrated and the anodic and cathodic current density are about 1000 times smaller that their limiting current densities, i_l.

$$\frac{F\eta_{cons}}{RT} = ln\{c^s/c^b\} = ln\left\{1 - \frac{i}{i_l}\right\} \quad (5\text{-}22)$$

The cathodic reaction is a rapid reaction, with low overpotential, of less than 50 mV; therefore, the linearized Butler-Volmer (B.V.) equation is used to relate the cathodic current density to the reaction overpotential [51]:

$$i_c = i_{0_c} F\eta_c/RT \quad (5\text{-}23)$$

On the other side, the high anodic overpotential is expressed by the Tafel equation. Moreover, a part of the surface is covered by the bubbles, a situation taken into account by the bubble coverage parameter ($\emptyset_b$). Therefore, on this boundary, only (1- $\emptyset_b$) of the surface is available for the heterogeneous reaction [99,100]. The bubble coverage parameter is equal to the bubble volume fraction at the surface of the anode (α_{b_a}), calculated through Eq. 12. Adding the bubbles hyperpolarization [58] to the Tafel equation, the relation between the anodic current density and anodic overpotential becomes:

$$i_a = i_{0a}\left(1 - \alpha_{b_a}\right) exp\{\alpha_{O_a} F\eta_a/RT\} \quad (5\text{-}24)$$

To solve the Eqs. 22 ,23 , the exchange current densities , i_{0a} and i_{0c} should be specified. The exchange current densities depends on anodic and cathodic reaction rates and also the ions concentrations according to the equation below [51]:

$$i_0 = k_r Fc \quad (5\text{-}25)$$

Where c is the concentration of active ions inside the cell and close to the surface of relative electrode. k_r is the reaction rate constant. The specific value of k_r for the heterogeneous reactions of lithium cell has not published yet. Therefore, it is estimated for each reaction as follow:

- At the anode: the chloride oxidation is slow. Therefore reaction rate should be between 10^{-9} m s^{-1} and 10^{-11}m s^{-1} [9,51].
- At the cathode: k_r has been approximated at a value high enough so to satisfy the condition for the use of linearized B.V. equation (η_c<50 mV) [9,51].

➢ Resistive layer overpotential

The layer of fluid close to the anode, which is a mixture of electrolyte and chlorine bubbles, has a lower conductivity than the rest of the electrolyte. The bubbles are thus responsible for an additional overpotential in the cell, presented as a resistive layer overpotential, η_b. It is defined at the anode, through equation bellow:

$$\eta_b = {}^{l}/_{\sigma_{mix}}\ i_a \tag{5-26}$$

$$\sigma_{mix} = \sigma_l\left(1 - \alpha_{b_a}\right)^{1.5} \tag{5-27}$$

Where σ_{mix} is the conductivity of the two-phase mixture and l is the resistive layer thickness, which changes linearly with the anode length, from zero at the bottom corner of the anode to 0.3 mm at the top. These values are obtained from the bubbles distribution resulting from the two-phase model.

➢ Anodic and cathodic current density distribution:

As mentioned before, the anodic current density is fixed and the anodic current distribution is solved through the tertiary current distribution.

On the other side of the cell, cathodic current density distribution depends on the anodic current density through following equation.

$$i_c = i_a \times A_a/A_c \tag{5-28}$$

In this way, the total current is the equal for both electrode

5.4 Validation of the new solver

The validation of the newly developed code has been done in three steps:

1. Some general results such as the cell potential and current density are compared to the experimental data from the aforementioned physical model, see Table 5-3.

Table 5-3 Comparison between the experiment and simulation of cell potential for the two different current densities

Current density/A m^{-2}	13800	18500
Cell potential from Experimental /V	5.8	7.25
Cell potential from Simulation /V	5.7	6.5

   The difference between the experimental and simulation potential results from the non ideality of the experimental cell and loss of energy and current.
2. The presented two-phase flow model has been used for the simulation of the flow field in a magnesium cell and compared with the velocity distribution obtained from experimental and numerical simulation performed by Liu [8] for the gas inlet of 1.5 litter per min, see Fig 5-4.
3. The validation is also pursued by comparing the results obtained from presented OpenFOAM solver with previously published results of a lithium experimental cell [9], a work done by the authors using a commercial software, COMSOL®, which has been already validated by some other experiments. In the present work, a result of this comparison can be seen in Fig 5-5. That shows the magnitude of the current density in three horizontal cutting lines that go through ACD.

In Fig 5-5, the difference in current densities close to the anode comes from the fact that in the simulation with OpenFOAM, the electrolyte velocity and the shape of bubbles resistive layer, used for the simulation of tertiary current distribution, has been obtained from two-phase flow model. All of which is not the same for the COMSOL solver, used for the validation. More description about the COMSOL model can be found in the authers previous works [9,12].

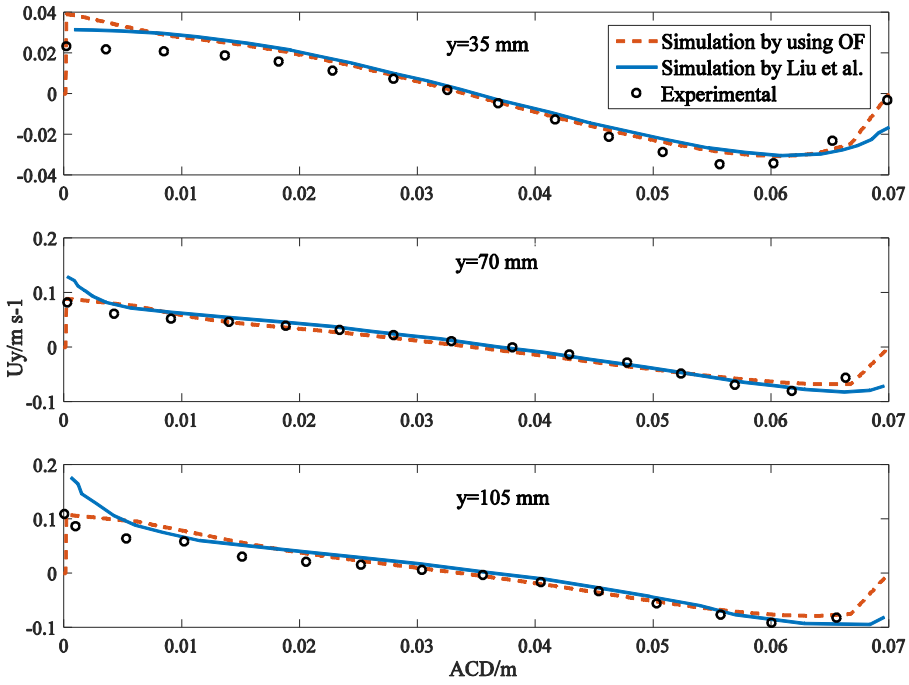

Fig 5-4 Vertical component of the electrolyte velocity from a magnesium production cell with a gas inlet rate of 1.5L min-1: comparison between experiments, two-phase flow model by Liu et al., and OpenFoam simulation

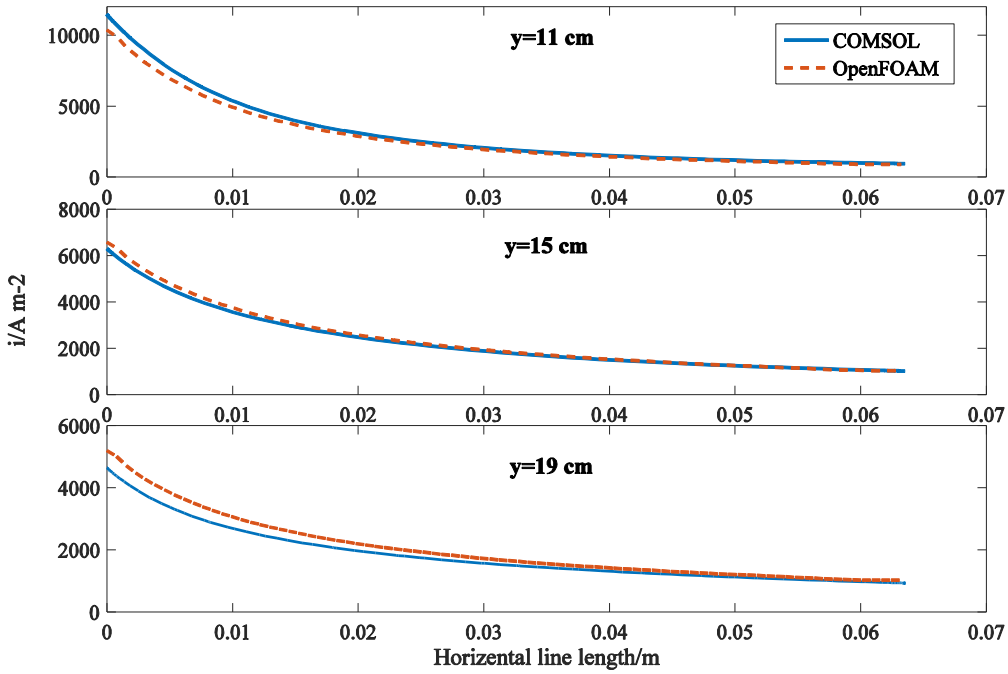

Fig 5-5. Resulting current density magnitude from a lithium production cell: comparison between OpenFOAM and COMSOL simulations at different levels from the bottom of the anode to the top of the cell

5.5 Results and Discussion

The electric and velocity fields and the flux of ions for a gas-lift lithium electrolysis cell are presented in this section. Firstly, a base case, with the geometry shown in Fig 5-1b, is defined, simulated and validated. Then, the solver is used for the simulation of a longer anode to investigate the effects of the anode length on the electric and velocity fields.

5.5.1 Electric Field

From the current density distribution shown in Fig 5-6, one can see that the current density is maximum at the bottom corner of the anode and at the top corner of the cathode. Except at their corners, the current density distribution at the electrodes is constant and equal to 13850 A m^{-2} at the anode and 10000 A m^{-2} at the cathode. The cathodic current density is smaller than the anodic current density because the cathode has a bigger area, and the total current has to be conserved.

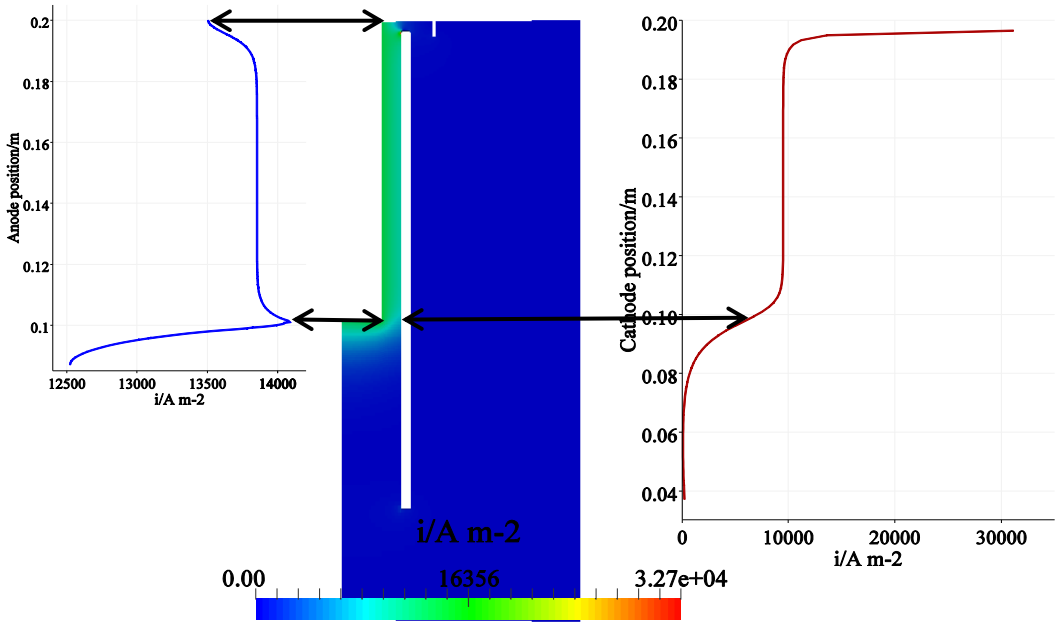

a b c

Fig 5-6. Current density distribution a) along the anode, b) in the bulk, c) along the cathode

Furthermore, the only active area in this cell is located inside the interpolar region and the current density is approximately zero for the rest of the cell. In the perspective to increase the productivity of the electrolysis process, it is better to increase the size of the active area

by increasing the length of the anode. The current distribution inside a cell with matching electrodes lengths is shown in the Fig 5-7. The same boundary conditions as the base case are kept for this new case. Therefore, in order to keep the current at its nominal target of 120 A, the anodic current density of the case with longer anode is reduced to 9000 A m^{-2}. Moreover, in this case, except at the corner of the electrodes, the current density distribution gets uniform all over their surface. The more uniform is the current distribution at the electrodes, the longer is their life time [10].

As it can be seen in Fig 5-7, the current density sharply increases at the corners of the cathode. Along these small areas, the electric field is stronger than the rest of the cathode due to the design of the cell while the anode is still longer than cathode, on both ends. Such an effect could also be seen on Fig 5-5, at the top of the cathode.

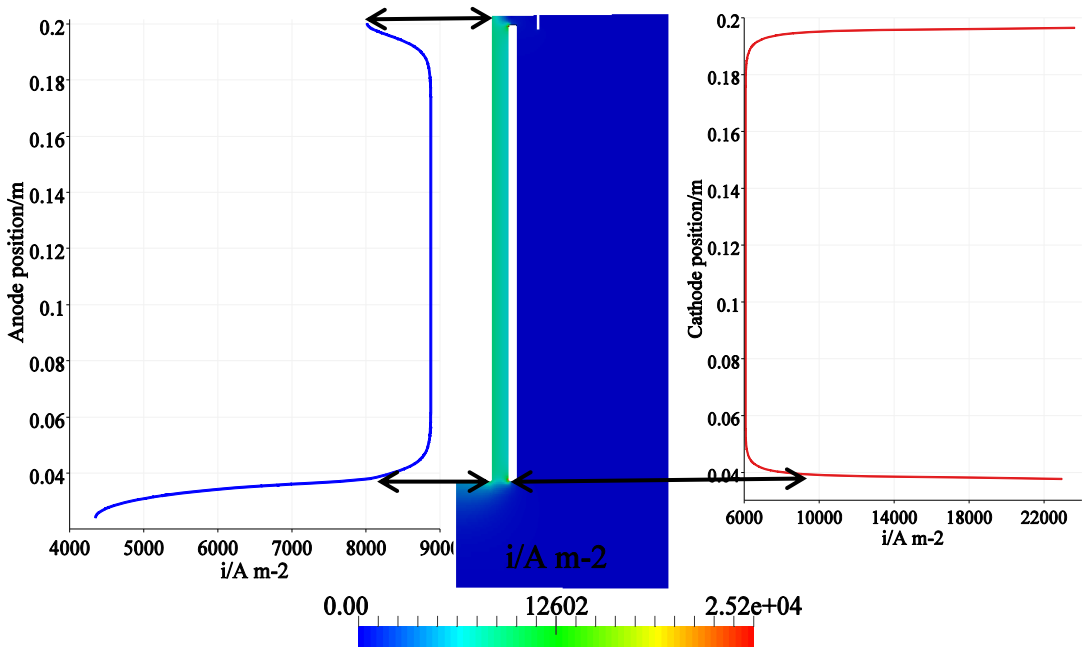

a b c

Fig 5-7. Current distribution for the cell with longer anode a) along the anode, b) it the bulk, c) along the cathode

As illustrated in Fig 5-8, the total cell potential can be divided into three parts:

1. The equilibrium potential, 3.6 V, assumed to be fixed because the cell is isothermal [10,80].
2. The reaction overpotential or anodic overpotential (the cathodic overpotential is lower than 50 mV and is not shown in this figure)
3. The ohmic overpotential comprising of:
   - The resistive layer or bubble layer overpotential
   - The electrolyte (ohmic) overpotential

In Fig 5-8, the equilibrium potential and average anodic, ohmic and resistive layer overpotentials have been presented for two simulations with different anode lengths. The total cell potential, i.e. energy consumption, is reduced when the anode gets longer, see Fig 5-8. The comparison between the total cell potential calculated for the base case (5.7 V) with the measured total potential obtained from the experimental cell (5.8 V) confirms the validity of the simulated electric field. As mentioned before, the reaction and resistive layer overpotentials depend on the current density distribution. It is concluded that the longer anode has uniform and lower current density that caused lower overpotentials specially the resistive layer overpotential, which is 60 % lower in the case with longer anode. Moreover, the lower is the current density, the lower is the electrolyte overpotential [9]. As a result, the electrolyte potential for the case with longer anode (case b) is just 65 % of that of base case (case a). Overall, the total cell potential for the case b is 0.6 V lower than that of case a, which represents a 10 % decrease in the global energy consumption.

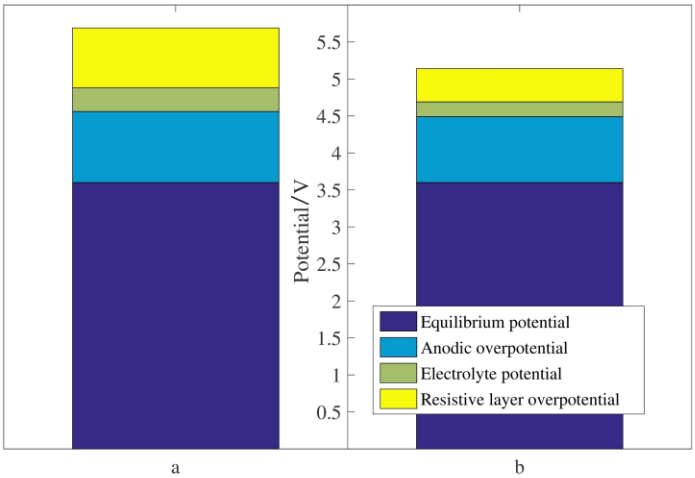

Fig 5-8. Average potential and overpotential for a) base case b) case with longer anode

Fig 5-9 shows that the cell potential of base case and the case with longer anode almost linearly increases with an increase of current density. The graphs are approximately linear because except within the diffusion boundary layer, the effect of diffusion on electric field can be omitted. Therefore, the ohm law governs the relation between ohmic overpotential and current density. It is the same also for the resistive layer overpotential. Therefore, the only non-linear part of cell potential versus current comes from the anodic overpotential which is about one-fifth of cell potential, as can be seen in Fig 5-8.

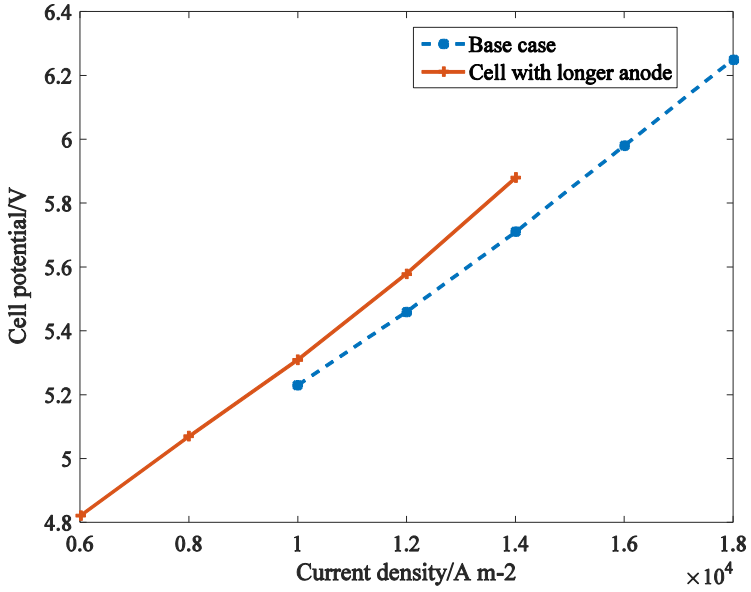

Fig 5-9. Total polarization curve for the base case and the case with longer anode

Furthermore, when the current density is the same for both cases, the cell potential is higher for the cell with longer anode which has roots on the resistive layer overpotential. In fact, in the case with longer anode more bubbles are produced, i. e. the resistive layer is ticker and longer.

5.5.2 Flow field

Bubbles introduce a drag force to the fluid that pushes the electrolyte upward in the interpolar region, which is replaced with fresh electrolyte coming from the bottom of the cell, see Fig 5-10. The diaphragm at the top of the cell blocks the way to the electrolyte and acts as a baffle. As a result, the electrolyte moves down and circulates around the cathode. The velocity is negligible in the rest of the cell. A comparison between Fig 5-10a

and b shows that the maximum velocity for the cell with longer anode is higher than that for the base case. As a matter of fact, in case b, the bubbles produced at the lower part of the anode have more time for acceleration and so they get out with higher velocity. The electrolyte circulation gets stronger around the cathode, which translates into a higher eddy diffusivity and ions fluxes and results to a lower electrolyte overpotential.

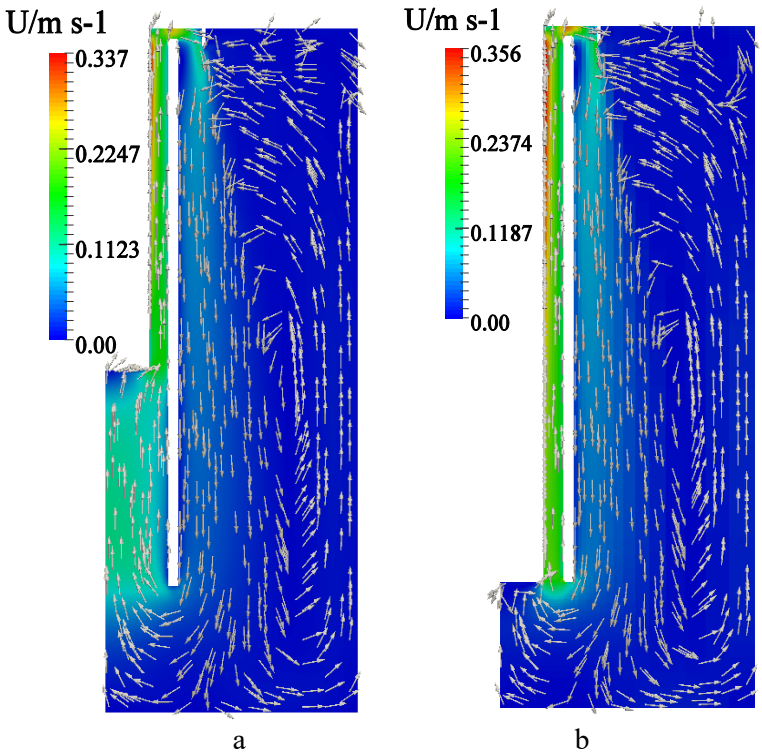

Fig 5-10. Scaled off electrolyte velocity vectors on the top of electrolyte for a) base case b) case with longer anode

The bubble volume fraction increases from bottom to top in a thin layer close to the anode (see Fig 5-11). At the bottom corner of the anode, the thickness of this layer is almost zero and at the top, where the anode faces the top of cathode, it is 3 mm. Close to the free surface, at the top of the cell, the thickness of this layer sharply increases, but is still limited by the diaphragm at the right of the cathode, and, since the position of the cathode is below the free surface, chlorine bubbles cannot reach the cathode. The maximum bubbles volume fraction is 65.8% for the base case. For the cell with a longer anode, the bubbles follow the same trend however, the accumulation of the bubbles is higher, and the bubble volume fraction goes to 0.83 close to the free surface.

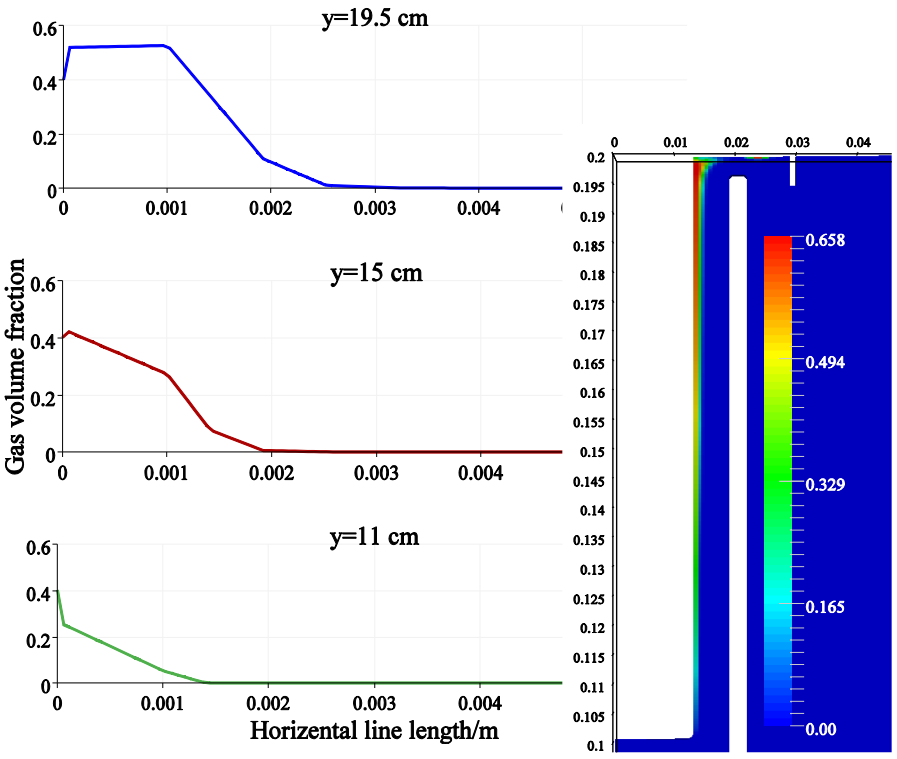

a b

Fig 5-11. Chlorine volume fraction in interpolar distance a) for different horizontal elevations b) on 2D graph

The simulated velocity field and bubbles volume fraction confirm the validity of aforementioned idea behind the gas lift cell design: even though no diaphragm is used to separate anodic and cathodic parts, the circulation of electrolyte is strong enough that no bubbles can catch the cathode.

5.5.3 Ions transfer

Fig 5-12 presents the migration and diffusion fluxes of lithium ions along a horizontal line between the anode and cathode at y=0.15 m. As expected, the diffusion of ions is significant only inside the boundary layer close to the electrodes while the migration is important all over ACD. The migration flux decreases from the anode to cathode; this is due to the increase of the surface area perpendicular to the migration flux.

In the bulk, anions and cations move to the anode and cathode respectively due to the migration force, while their global movement is driven by convection. As a matter of fact,

the convection flux dominates all mass transfer mechanisms in the bulk as it is approximately 6 orders of magnitude higher than both diffusion and migration.

It is worth to mention that the convection is mainly affected by the velocity distribution. Therefore, all ions in the bulk are moving along the streamlines of the flow. As explained earlier in the mathematical model section, this allows to use a simple correlation for the multicomponent diffusion coefficient.

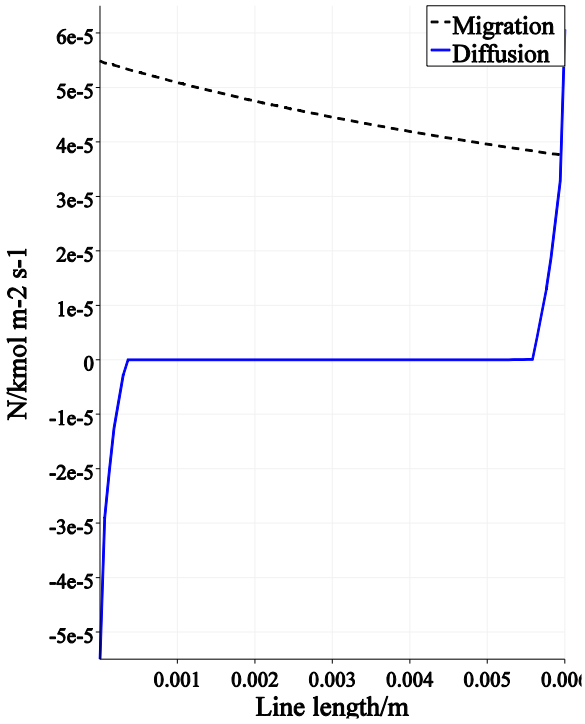

Fig 5-12. Diffusion and migration flux of lithium ions at y=0.15m

Fig 5-13 presents the ions migration and diffusion fluxes at the surface of electrodes. The chloride and lithium ions are the active ions at the anode and cathode, respectively. Both migration and diffusion fluxes for the active ions are in the same direction, toward their respective electroactive area. Initially, the ions move to the electrodes through migration and then active ions get consumed through heterogeneous reactions so their concentration decreases from the bulk to the electrodes.

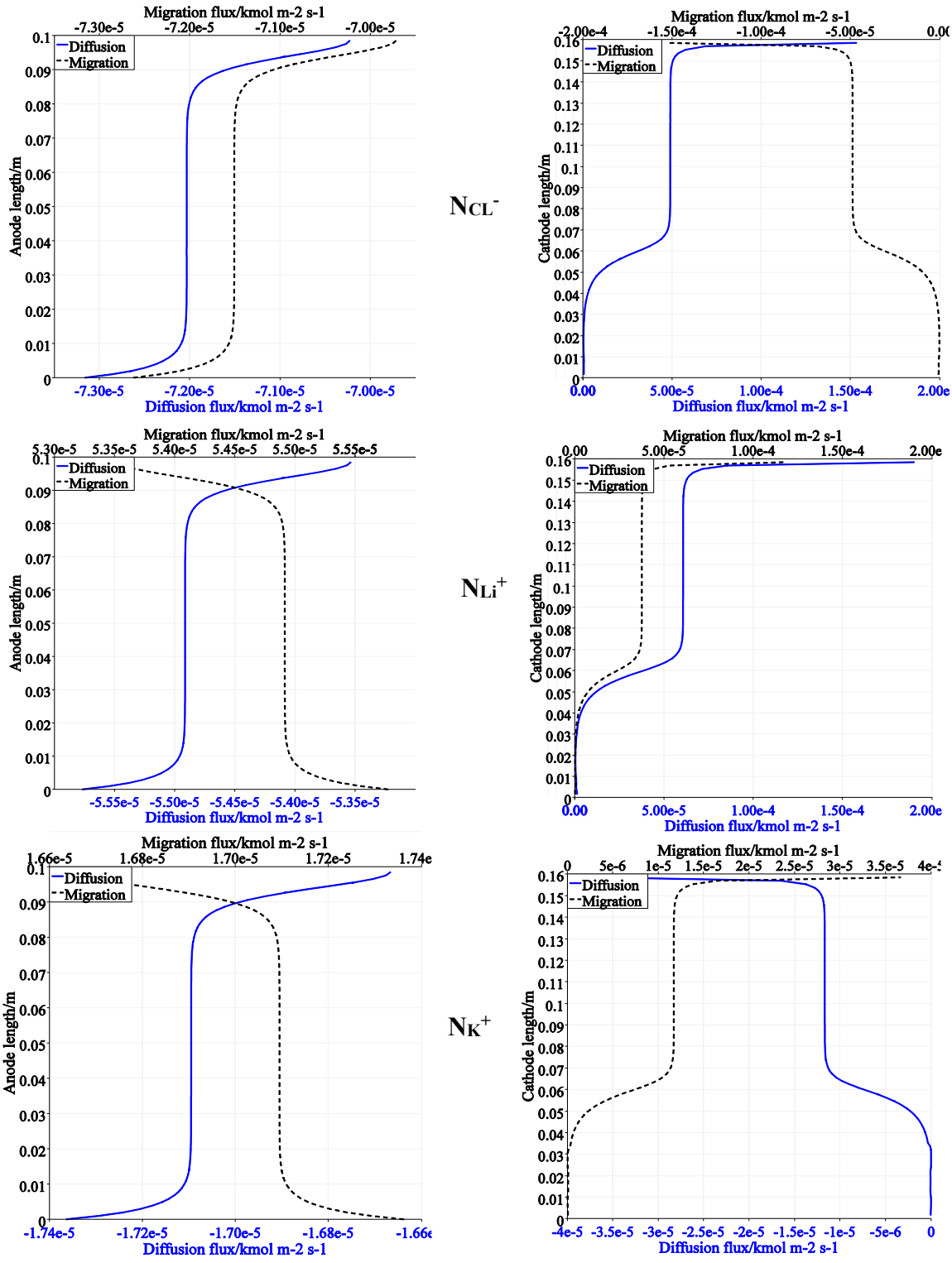

Fig 5-13. Chloride, lithium and potassium ions migration (black dash line) and diffusion (continuous blue line) fluxes a) at the anode b) at the cathode

On the other side, lithium and potassium are electro-inactive at the anode; chloride and potassium are electro-inactive at the cathode. The total flux of electro-inactive ions should be zero at the aforementioned electrode. As can be seen in Fig 5-13, the migration and diffusion fluxes are equal but in opposite directions for the electro-inactive ions. Migration pushes the anions to the anode and cations to the cathode, while the diffusion balance the total flux back to zero. At the anode, when chloride is consumed, the concentration of positive ions decreases due to the electroneutrality. This is why the direction of diffusion is always toward the anode. At the cathode, chloride and lithium ions diffuse to the electrode but the diffusion of the potassium goes from the surface to the bulk, again to keep the electroneutrality.

5.6 Conclusion

A new solver in OpenFOAM has been developed and used to investigate the concentration, electric and velocity fields inside a new design of lithium electrolysis cell called the gas-lift cell. In this new model, the two-phase flow is linked to the electric field at the anode, where the bubble distribution is closely linked to the current density. The tertiary current distribution represents the ions transfer, which truly considers the intimate coupling between the concentration, velocity, and potential fields, and also with the current distribution. The accuracy of the solver has been validated, based on some experimental data and simulation results published recently. The validated models has been used for the simulation of the gas-lift design, a diaphragmless cell operated with a deliberately small ACD. The bubbles distribution obtained from the model showed that the electrolyte circulation is high enough to remove adequately the produced lithium from the ACD before the chlorine bubbles reach and react with it. Moreover, by comparing migration, diffusion and convection fluxes, it can be concluded that the latter is dominating in the bulk. In addition, migration ions transfer is a contributing mechanism in ACD while the diffusion is playing a significant role only in the boundary layer close to the surface.

Since the active area is located inside ACD, the increase of the anode length shows significant improvements in the cell energy consumption and current distribution. Finally, the use of the new solver can be extended for the simulation of any electrolysis cell due to the generality of the equation and algorithms developed in this work.

Acknowledgments

The authors wish to thank Dr. Kamyab Amouzegar for his useful suggestions. We also appreciate Hydro-Québec for their financial support, for providing us with the experimental results and giving us the opportunity to publish this work. The authors are also grateful to the Natural Sciences and Engineering Council of Canada (NSERC) for its financial support.

5.7 Nomenclature

c	Concentration, kmol m^{-3}
D	Diffusion coefficient, m^2 s^{-1}
d	Diameter, m
E	Potential, V
F	Faraday's constant, A s $kmol^{-1}$
g	Earth gravitational acceleration, m s^{-2}
i	Current density, A m^{-2}
i_0	Exchange current density, A m^{-2}
k	Turbulent kinetic energy, m^2 s^{-2}
l	Resistive layer thickness, m
M	Molecular weight, kg $kmol^{-1}$
n	Number of electrons
N	Molar flux, kmol m^{-2} s^{-1}
p	Pressure, kg m^{-1} s^{-2}
R	Gas constant, J $kmol^{-1}$ K^{-1}
Re	Reynolds number
R^T	Turbulent Reynolds stress, m^2 s^{-2}
t	Time, s
T	Temperature, K
u	Ions mobility, m^2 s^{-1} V^{-1}
U	Velocity vector, m s^{-1}
y	Mole fraction
z	Valence

Greek letters

α	Volume fraction
ϵ	Rate of dissipation of kinetic energy, $m^2\ s^{-3}$
σ	Conductivity, $S\ m^{-1}$
ρ	Density, $kg\ m^{-3}$
μ	Viscosity, $kg\ s^{-1}\ m^{-1}$
ν	Kinematic viscosity, $m^2\ s^{-1}$
$\emptyset_b$	Bubble coverage
η	Overpotential, V

Subscript/ Superscripts

a, c	Anode/ Cathode
b	Bubble
e	Electrolyte
i	Species i
j	Species j
mix	Mixture
T	Turbulent
t	Total
cons	Concentration
vm	virtual mass
s	Surface
b	Bulk
mig	Migration

6 Conclusion

6.1 Conclusion en Français

La croissance des applications à base de lithium dans des industries telles que les batteries aux ions lithium provoque l'explosion de la demande mondiale de lithium au fil du temps. La voie la plus commune pour la production de lithium métallique est l'électrolyse du chlorure de lithium. Pour satisfaire la demande du marché industriel avec des cellules à haute efficacité, une investigation scientifique rigoureuse est nécessaire. Bien que l'environnement de production de la cellule soit difficile, y compris la haute température et la corrosivité de l'électrolyte, ce qui limite les études expérimentales menées avec de telles cellules, la simulation numérique peut fournir suffisamment d'informations sur les aspects saillants de la conception. Dans le présent travail, deux modèles ont été développés pour prédire le transfert d'ions dans une cellule d'électrolyse à haute température utilisant un mélange eutectique de LiCl-KCl comme électrolyte en utilisant un logiciel commercial, COMSOL et une boîte à outils à accès libre, OpenFOAM. Les modèles ont été mis en œuvre pour étudier deux types de cellules de production de lithium: cellule avec diaphragme et cellule sans diaphragme. La validité des résultats a été vérifiée en comparant les résultats simulés avec des résultats simulés expérimentaux ou publiés. Ensuite, l'effet de différents paramètres sur la consommation d'énergie de la cellule a été étudié et finalement le meilleur cas simulé, celui qui réduit le plus la consommation d'énergie de la cellule, a été introduit.

Les principaux effets des bulles de chlore produites à l'anode sur le flux, les champs électriques et de concentration ont été pris en compte. Pour la cellule à diaphragme, un modèle d'écoulement à une phase a été couplé aux équations de transport d'ions. Le mouvement ascendant de l'anode est utilisé pour représenter le mouvement des bulles. La distribution de la vitesse de l'électrolyte est simulée par un modèle de flux diphasique dans OpenFOAM pour la cellule sans diaphragme. De nombreux phénomènes sont représentés comme les bulles bloquant le chemin des ions à l'anode et dans le volume, un phénomène à l’origine de deux surpotentiels: l'hyperpolarisation et la surtension de la couche résistive.

De plus, les modèles développés dans cette thèse prennent en compte les effets des réactions hétérogènes, de la diffusivité/diffusion turbulente et des paramètres de transport multicomposante sur le transfert d'ions. Les paramètres de transport dépendent des concentrations d'ions. En conséquence, les modèles présentent un fort couplage entre les champs de concentration, de potentiel et d'écoulement.

Enfin, cette recherche propose:

- Les premières publications examinant le transfert de masse à l'intérieur de la cellule au lithium.
- Le premier modèle d'écoulement diphasique pour une cellule au lithium avec une distribution de bulles non uniforme à l'électrode.
- Un premier travail de recherche simulant le couplage intime entre les champs électriques et de concentration à l'intérieur d'une cellule d'électrolyse au lithium.
- Le développement d'un nouveau solveur à accès ouvert pouvant être utilisé pour la simulation de transfert de masse à l'intérieur d'une cellule d'électrolyse incluant des écoulements monophasés ou diphasiques, avec ou sans diaphragme et avec des électrodes verticales ou horizontales.

Le modèle peut être amélioré en mettant en œuvre les suggestions suivantes:

- Ajout d'un modèle de bilan de population au nouveau solveur OpenFOAM développé. Comme présenté dans la thèse, les bulles ont des effets énormes sur différents aspects de la cellule. Par conséquent, la simulation des bulles avec plus de détails peut donner une meilleure connaissance de ces effets.
- Une analyse numérique du taux de séparation primaire des gouttes de lithium, comme ce que Liu et al. ont fait pour la cellule de magnésium, fournira des informations précieuses sur la possibilité de réaction rétroactive.

Ensuite, la géométrie de la cellule peut être améliorée en optimisant à la fois l'efficacité du courant et la consommation d'énergie. Enfin, la conception optimale peut être construite comme une configuration expérimentale pour vérifier la validité du modèle. Après la mise en œuvre des suggestions, je crois que le travail a le potentiel de mener à au moins un brevet.

6.2 Conclusion in English

The growth of lithium applications in industries such as lithium ion batteries causes the explosion of the lithium world's demand over the time. The most common path for the production of lithium is the electrolysis of lithium chloride. A rigorous scientific investigation is needed to satisfy the industrial market demand with high energy efficient cells. Although the harsh environment of the cell, including the high temperature and corrosiveness of the electrolyte, limits the experimental studies conducted with such cells, the numerical simulation could provide enough information about the salient aspects of the design. In the present work, two models to predict the transfer of ions in a high temperature electrolysis cell using an eutectic mixture of LiCl-KCl as the electrolyte have been developed using a commercial software, COMSOL, and an open access toolbox, OpenFOAM. The models have been implemented to study two types of lithium production cells: cell with diaphragm and diaphragmless cell. The validity of the results has been checked by comparing the simulated results with some experimental or published simulated results. Then, the effect of different parameters on the energy consumption of the cell has been investigated and finally the best-simulated case, which lowers the cell energy consumption, has been introduced.

The main effects of chlorine bubbles produced at the anode on the flow, electric and concentration fields have been taken into account. For the diaphragm cell, a one-phase flow model is coupled to the ions transport equations. The upward movement of the anode is used to represent the bubbles movement. The electrolyte velocity distribution is simulated by a two-phase flow model in OpenFOAM for the diaphragmless cell. Many phenomena are represented like the bubbles blocking the path of the ions at the anode and in the bulk, which are the causes of two overpotentials: the hyperpolarization and the resistive layer overpotential. Moreover, the developed models in this thesis take into consideration the effects of heterogeneous reactions, eddy diffusivity and multicomponent transport on the ions transfer. The transport parameters depend on ions concentration. Accordingly, the models present strong coupling between concentration, electric and flow fields.

Finally, this research offers:

- The first publications investigating the mass transfer inside lithium production cell.
- The first two-phase flow model for the lithium cell with non-uniform bubble distribution at the electrode.
- The first research work simulating the intimate coupling between electric and concentration fields inside lithium electrolysis cell.
- The development of a new open access solver that can be used for the simulation of mass transfer inside an electrolysis cell including one or two-phase flows, with or without diaphragm and with vertical or horizontal electrodes.

The model can be improved through implementing the following suggestions:

- Adding a population balance model to the new developed OpenFOAM solver. As presented in the thesis, the bubbles have enormous effects on different aspects of the cell. Therefore, the simulation of the bubbles with more details can give a better knowledge about those effects.
- Considering a numerical analysis of primary separation rate of lithium drops, like what Liu et al. did for the magnesium cell, will provide valuable information about the possibility of back reaction.

Then, the cell geometry can be improved by optimizing both current efficiency and energy consumption.

Finally, the optimum design can be built as an experimental setup to check the validity of the model.

After implementing the suggestions, I believe that the work has the potential to lead to at least one patent.

References

[1] Roskill, Lithium Global Industry, Markets & Outlook, 2017.

[2] U. Wietelmann, R.J. Bauer, Lithium and lithium compounds, in: Ullmann's Encycl. Ind. Chem., Wiley, Weinheim, 2012: pp. 339–366. doi:10.1002/14356007.a15_393.

[3] J.A. Ober, Mineral commodity summaries 2017, US Geological Survey, 2017.

[4] T. Tran, V.T. Luong, Lithium Production Processes, in: J.B.T.-L.P.C. Światowska (Ed.), Lithium Process Chem. Resour. Extr. Batter. Recycl., Elsevier, Amsterdam, 2015: pp. 81–124. doi: 10.1016/B978-0-12-801417-2.00003-7.

[5] E.R. Van Artsdalen, I.S. Yaffe, Electrical conductance and density of molten salt systems: KCl--LiCl, KCl--NaCl and KCl--KI, J. Phys. Chem. 59 (1955) 118–127.

[6] A. Cox, J.W.A. Morris, D.J. Fray, Improving the energy efficiency of electrowinning of lithium, Light Met. Proc. Sess. TMS Annu. Meet. (Warrendale, Pennsylvania). (1998) 1295–1298.

[7] K. Amouzegar, S. Harrison, Electrolytic production of lithium metal, Shawinigan (Québec), 1996.

[8] C.-L. Liu, Z. Sun, G.-M. Lu, X.-F. Song, J.-G. Yu, Experimental and numerical investigation of two-phase flow patterns in magnesium electrolysis cell with non-uniform current density distribution, Can. J. Chem. Eng. 93 (2015) 565–579. doi:10.1002/cjce.22135.

[9] E. Oliaii, M. Désilets, G. Lantagne, Numerical analysis of the effect of structural and operational parameters on electric and concentration fields of a lithium electrolysis cell, J. Appl. Electrochem. 47 (2017) 711–726. doi:10.1007/s10800-017-1073-2.

[10] E. Oliaii, M. Désilets, G. Lantagne, Effect of the design parameters on mass transfer and energy consumption inside a lithium electrolysis cell, J. Appl. Electrochem. (2018) 1–13. doi: 10.1007/s10800-018-1179-1.

[11] G. Litrico, E. Oliaii, C.B. Vieira, M. Désilets, P. Proulx, Mass transfer study inside a Li production electrolysis cell based on a rigorous CFD analysis, J. Fluid Flow, Heat Mass Transf. (2018). doi:10.11159/jffhmt.2018.003.

[12] E. Oliaii, G. Litrico, M. Désilets, G. Lantagne, Mass transport and energy consumption inside a lithium electrolysis cell, Electrochim. Acta. (2018).

[13] Z. Sun, C. Liu, G. Lu, X. Song, J. Yu, Effects of operational and structural parameters on cell voltage of industrial magnesium electrolysis cells, Front. Chem. Sci. Eng. 9 (2015) 522–531. doi:10.1007/s11705-015-1539-x.

[14] M. Dupuis, V. Bojarevics, J. Freilbergs, Demonstration thermo-electric and MHD mathematical models of a 500 kA aluminum electrolysis cell: Part 2, in: Light Met., TMS, 2004: pp. 453–460.

[15] M. Dupuis, V. Bojarevics, Weakly coupled thermo-electric and MHD mathematical models of an aluminium electrolysis cell, Light Met. 1 (2005) 449–454.

[16] D.S. Severo, A.F. Schneider, E.C. V Pinto, V. Gusberti, V. Potocnik, Modeling magnetohydrodynamics of aluminum electrolysis cells with ANSYS and CFX, Light Met. 2005 (2005) 475–480.

[17] Y. Safa, Simulation numérique des phénomènes thermiques et magnétohydrodynamiques dans une cellule de Hall-Héroult, (2005).

[18] Y. Safa, M. Flueck, J. Rappaz, Numerical simulation of thermal problems coupled with magnetohydrodynamic effects in aluminium cell, Appl. Math. Model. 33 (2009) 1479–1492. doi:10.1016/J.APM.2008.02.011.

[19] V. Bojarevics, K. Pericleous, Comparison of MHD models for aluminium reduction cells, Proc. TMS Light Met. (2006) 347–352.

[20] Z. Sun, H. Zhang, P. Li, B. Li, G. Lu, J. Yu, Modeling and simulation of the flow field in the electrolysis of magnesium, JOM. 61 (2009) 29–33. doi:10.1007/s11837-009-0066-y.

[21] M. Flueck, A. Janka, C. Laurent, M. Picasso, J. Rappaz, G. Steiner, Some mathematical and numerical aspects in aluminum production, J. Sci. Comput. 43 (2010) 313–325.

[22] Z. Sun, P. Li, G. Lu, B. Li, J. Wang, J. Yu, Effect of Electromagnetic Field on Three-Phase Flow Behavior, Ind. Eng. Chem. Res. 49 (2010) 10798–10803.

[23] Z. Sun, C. Liu, G. Lu, X. Song, S. Sun, Y. Sun, J. Yu, Coupled thermoelectric model and effects of current fluctuation on thermal balance in magnesium electrolysis cell, Energy & Fuels. 25 (2011) 2655–2663.

[24] D. Marceau, S. Pilote, M. Désilets, J.-F. Bilodeau, L. Hacini, Y. Caratini, Advanced numerical simulation of the Thermo-Electro-Chemo-Mechanical behaviour of Hall-Héroult cells under electrical preheating, in: Light Met. 2011, Springer, 2011: pp. 1041–1046.

[25] L. Zhongxing, W. Liangliang, W. Yongfu, W. Xiaoqing, 3D Simulations of electric field on 40 kA sodium electrolysis cell, Energy Procedia. 14 (2012) 418–423. doi:10.1016/J.EGYPRO.2011.12.952.

[26] C. Liu, Z. Sun, G. Lu, X. Song, Y. Ding, J. Yu, Scale-up design of a 300 kA magnesium electrolysis cell based on thermo-electric mathematical models, Can. J. Chem. Eng. 92 (2014) 1197–1206.

[27] M. Ariana, M. Désilets, P. Proulx, On the analysis of ionic mass transfer in the electrolytic bath of an aluminum reduction cell, Can. J. Chem. Eng. 92 (2014) 1951–1964. doi:10.1002/cjce.22047.

[28] Q. Zhang, M.P. Taylor, J.J.J. Chen, Computational Modeling of Thermochemical Evolution of Aluminum Smelter Crust, Metall. Mater. Trans. B. 46 (2015) 1520–1534. doi:10.1007/s11663-015-0304-3.

[29] B. Bardet, T. Foetisch, S. Renaudier, J. Rappaz, M. Flueck, M. Picasso, Alumina Dissolution Modeling in Aluminium Electrolysis Cell Considering MHD Driven Convection and Thermal Impact, in: Light Met. 2016, Springer, 2016: pp. 315–319.

[30] D. Li, K. Chattopadhyay, L. Gao, B. Davis, R. Schwarze, A. Asad, C. Kratzsch, Mathematical Modeling of Molten Salt Electrolytic Cells for Sodium and Lithium Production, in: S. Wang, M.L. Free, S. Alam, M. Zhang, P.R. Taylor (Eds.), Appl. Process Eng. Princ. Mater. Process. Energy Environ. Technol. An EPD Symp. Honor Profr. Ramana G. Reddy, Springer International Publishing, Cham, 2017: pp. 129–138. doi:10.1007/978-3-319-51091-0_11.

[31] Z. Sun, Y. Zhao, G. Lu, P. Li, J. Wang, J. Yu, Novel Method Based on Electric Field Simulation and Optimization for Designing an Energy-Saving Magnesium Electrolysis Cell, Ind. Eng. Chem. Res. 50 (2011) 6161–6173. doi:10.1021/ie101091p.

[32] G.N. Kannan, P.S. Desikan, Current trends towards energy reduction in electrolytic magnesium production, Bull. Electrochem. 6 (1990) 776–779.

[33] G.M. Rao, Electrolytic production of magnesium: Effect of current density, J. Appl. Electrochem. 16 (1986) 775–780. doi:10.1007/BF01006932.

[34] G. Demirci, \.Ishak Karakaya, Molten Salt Electrolysis of MgCl2 in a Cell with Rapid Chlorine Removal Feature, in: S.N. Mathaudhu, W.H. Sillekens, N.R. Neelameggham, N. Hort (Eds.), Magnes. Technol. 2012, Springer International Publishing, Cham, 2016: pp. 59–62. doi:10.1007/978-3-319-48203-3_11.

[35] C. Liu, Z. Sun, G. Lu, J. Yu, Analysis of magnesium droplets characteristics and separation performance in a magnesium electrolysis cell based on multiphysics modeling, Can. J. Chem. Eng. (2018).

[36] J. Cloyd Down, Electrolytic process and cell, US 1501756 A, 1924.

[37] J. Grosbois, J.Y.Y. Dumousseau, Process for the continuous production of lithium by electrolysis of lithium chloride in a molten salt mixture, and apparatus for carrying out said process, EP0107521A1, 1984.

[38] I. V. Kadija, K.E. Woodard Jr, Diaphragms for use in the electrolysis of alkali metal chlorides, 1979.

[39] J.M. Verdier, S. Jacubert, J. Grosbois, J.Y. Dumousseau, Continuous electrolysis of lithium chloride into lithium metal, US4617098, 1986.

[40] O.R. Bergmann, H.M. Blank, R.B. Diemer, D. Jain, T.A. Messing, W.J. Simmons, Modified electrolyte and diaphragm for fused salt electrolysis, 2000, US6063247.

[41] J. Muller, R. Bauer, B. Sermond, E. Dolling, Process and apparatus for producing high-purity lithium metal by fused-salt electrolysis, 1988.

[42] E. Le Roux, P. Nataf, S. Jacubert, Continuous production of lithium metal by electrolysis of lithium chloride, US 4724055 A, 1988.

[43] J. Christensen, D.K. Creber, G.C. Holywell, Electrolysis cells, 2002.

[44] E. Nakamura, H. Takata, Y. Yokoyama, H. Miyamoto, Process for producing metallic lithium, US20100051470, 2010.

[45] J.F. Cooper, O.H. Krikorian, R. V Homsy, Electrolytic method for the production

of lithium using a lithium-amalgam electrode, US 4156635 A, 1979.

[46] D.S. van Vuuren, E. Swanepoel, Fundamental Differences between Magnesium and Alkali Metal Electrowinning, Adv. Mater. Res. 1019 (2014) 160–168. doi:10.4028/www.scientific.net/AMR.1019.160.

[47] G.J. Janz, N.P. Bansal, Molten Salts Data: Diffusion Coefficients in Single and Multi-Component Salt Systems, J. Phys. Chem. Ref. Data. 11 (1982) 505. doi:10.1063/1.555665.

[48] K. Sridharan, S. Martin, M. Mohammadian, J. Sager, T. Allen, M.M. Simpson, M. Anderson, M.M. Simpson, Thermal properties of LiCl-KCl molten salt for nuclear waste separation, Trans. Am. Nucl. Soc. 106 (2012) 1240–1241.

[49] K. Andreassen, Electrolytic Production of Magnesium, Erzmetall J. Explor. Min. Process. Metall. Recycl. A. 31 (1978) 301–309.

[50] R. Taylor, R. Krishna, Multicomponent mass transfer, John Wiley & Sons, 1993.

[51] A. Bard, L. Faulkner, Electrochemical Methods: Fundamentals and Applications, second esi, Wiley, New York, 2001. doi:10.1023/A:1021637209564.

[52] K. Aldas, N. Pehlivanoglu, M.D. Mat, Numerical and experimental investigation of two-phase flow in an electrochemical cell, Int. J. Hydrogen Energy. 33 (2008) 3668–3675. doi:10.1016/j.ijhydene.2008.04.047.

[53] H. Vogt, R.J. Balzer, The bubble coverage of gas-evolving electrodes in stagnant electrolytes, Electrochim. Acta. 50 (2005) 2073–2079. doi:10.1016/j.electacta.2004.09.025.

[54] R. Clift, J.R. Grace, M.E. Weber, Bubbles, Drops, and particles, Academic p, Academic press, New York, 1978.

[55] H.K. Versteeg, W. Malalasekera, An introduction to computional fluid dynamics: The finite volume method, Longman Sc, Pearson Education, Harlow, 2007.

[56] G. Huber, M. Lutz, M. Wille, H. Friedrich, J. Guth, U. Behling, A. Franke, E. Gunkel, Electrolysis device for the production of alkali metal, US8114258, 2012.

[57] H.M. Blank, O.R. Bergmann, W.J. Simmons, Fused chloride salt electrolysis cell, US5904821, 1999 .

[58] J. Thonstad, P. Fellner, G.M. Haarberg, J. Híves, H. Kvande, A. Sterten, Aluminium Electrolysis: Fundamentals of the Hall-H{é}roult Process, Aluminium-Verlag, 2001.

[59] H. Vogt, On the gas-evolution efficiency of electrodes. II - Numerical analysis, Electrochim. Acta. 56 (2011) 2404–2410. doi:10.1016/j.electacta.2010.11.004.

[60] G. Nelissen, B. Van Den Bossche, J. Deconinck, A. Van Theemsche, C. Dan, Laminar and turbulent mass transfer simulations in a parallel plate reactor, in: J. Appl. Electrochem., 2003: pp. 863–873. doi:10.1023/A:1025811727594.

[61] I. Calmet, J. Magnaudet, Large-eddy simulation of high-Schmidt number mass transfer in a turbulent channel flow, Phys. Fluids. 9 (1997) 438–455.

[62] S.L. Lyons, T.J. Hanratty, J.B. McLaughlin, Large-scale computer simulation of fully developed turbulent channel flow with heat transfer, Int. J. Numer. Methods Fluids. 13 (1991) 999–1028.

[63] B. Tjaden, S.J.J. Cooper, D.J.J. Brett, D. Kramer, P.R.R. Shearing, On the origin and application of the Bruggeman correlation for analysing transport phenomena in electrochemical systems, Curr. Opin. Chem. Eng. 12 (2016) 44–51. doi:10.1016/J.COCHE.2016.02.006.

[64] D.-W. Chung, M. Ebner, D.R.R. Ely, V. Wood, R.E.E. García, Validity of the Bruggeman relation for porous electrodes, Model. Simul. Mater. Sci. Eng. 21 (2013) 74009.

[65] M. Ebner, V. Wood, Tool for tortuosity estimation in lithium ion battery porous electrodes, J. Electrochem. Soc. 162 (2015) A3064–A3070.

[66] M.E. Díaz, A. Iranzo, D. Cuadra, R. Barbero, F.J. Montes, M.A. Galán, Numerical simulation of the gas-liquid flow in a laboratory scale bubble column. Influence of bubble size distribution and non-drag forces, Chem. Eng. J. 139 (2008) 363–379. doi:10.1016/j.cej.2007.08.015.

[67] A. Alexiadis, M. Dudukovic, P. Ramachandran, A. Cornell, J. Wanngård, A. Bokkers, On the electrode boundary conditions in the simulation of two phase flow in electrochemical cells, Int. J. Hydrogen Energy. 36 (2011) 8557–8559. doi:10.1016/j.ijhydene.2011.04.149.

[68] K. Oldham, J. Myland, A. Bond, Electrochemical science and technology: fundamentals and applications, John Wiley & Sons, 2011.

[69] S.C. Amendola, L. Swonger, S. Goldman, Electrolytic production of lithium metal, (2014).

[70] G.J. Kipouros, D.R. Sadoway, Toward new technologies for the production of lithium, JOM. 50 (1998) 24–33.

[71] Y.C. Hoh, T.M. Chiu, Z.J. Chung, Preparation of lithium metal by molten salt electrolysis, in: Prod. Electrolysis Light Met., Elsevier, 1989: pp. 223–234. doi:10.1016/B978-0-08-037295-2.50025-9.

[72] J. Muller, R. Bauer, B. Sermond, E. Dolling, Process and apparatus for producing high-purity lithium metal by fused salt electrolysis, 4740279 A, 1988.

[73] G. Litrico, C.B. Vieira, E. Askari, P. Proulx, Strongly coupled model for the prediction of the performances of an electrochemical reactor, Chem. Eng. Sci. 170 (2017) 767–776. doi:10.1016/J.CES.2016.12.060.

[74] A. Kaneko, Y. Yamamoto, C. Okada, Electrochemistry of rare earth fluoride molten salts, J. Alloys Compd. 193 (1993) 44–46. doi:10.1016/0925-8388(93)90305-7.

[75] E.P. Rivero, E. Mayen, F.F. Rivera, M. Cruz-Diaz, I. González, Mass Transfer Modeling and Simulation under Turbulent Flow in Filter-Press-Type FM01-LC Electrochemical Reactor, ECS Trans. 29 (2010) 205–214.

[76] Y. Liu, O. Hinrichsen, Study on CFD–PBM turbulence closures based on k–ε and

Reynolds stress models for heterogeneous bubble column flows, Comput. Fluids. 105 (2014) 91–100. doi:10.1016/j.compfluid.2014.09.023.

[77] M. Philippe, H. Jérôme, B. Sebastien, P. Gérard, Modelling and calculation of the current density distribution evolution at vertical gas-evolving electrodes, Electrochim. Acta. 51 (2005) 1140–1156.

[78] P. Mandin, A.A. Aissa, H. Roustan, J. Hamburger, G. Picard, Two-phase electrolysis process: From the bubble to the electrochemical cell properties, Chem. Eng. Process. Process Intensif. 47 (2008) 1926–1932.

[79] A. Ghione, Development and validation of a two-phase cfd model using openfoam, (2012).

[80] E. Oliaii, M. Désilets, G. Lantagne, Numerical analysis of the effect of structural and operational parameters on electric and concentration fields of a lithium electrolysis cell, J. Appl. Electrochem. 47 (2017). doi:10.1007/s10800-017-1073-2.

[81] S. Corzo, S. Marquez Damian, D. Ramajo, N. Nigro, Numerical simulation of bubbly two-phase flow using eulerian-eulerian model, Asoc. Argentina Mec. Comput. 31 (2012) 85–112.

[82] O. Borchers, C. Busch, A. Sokolichin, G. Eigenberger, Applicability of the standard k–ε turbulence model to the dynamic simulation of bubble columns. Part II:: Comparison of detailed experiments and flow simulations, Chem. Eng. Sci. 54 (1999) 5927–5935. doi:10.1016/S0009-2509(99)00181-5.

[83] R.F. Mudde, O. Simonin, Two- and three-dimensional simulations of a bubble plume using a two-fluid model, Chem. Eng. Sci. 54 (1999) 5061–5069. doi:10.1016/S0009-2509(99)00234-1.

[84] D. Pfleger, S. Gomes, N. Gilbert, H.-G. Wagner, Hydrodynamic simulations of laboratory scale bubble columns fundamental studies of the Eulerian–Eulerian modelling approach, Chem. Eng. Sci. 54 (1999) 5091–5099. doi:10.1016/S0009-2509(99)00261-4.

[85] A. Sokolichin, G. Eigenberger, Applicability of the standard k–ε turbulence model to the dynamic simulation of bubble columns: Part I. Detailed numerical simulations, Chem. Eng. Sci. 54 (1999) 2273–2284. doi:10.1016/S0009-2509(98)00420-5.

[86] B. Selma, R. Bannari, P. Proulx, A full integration of a dispersion and interface closures in the standard k–ε model of turbulence, Chem. Eng. Sci. 65 (2010) 5417–5428. doi:10.1016/J.CES.2010.06.020.

[87] A. Behzadi, R.I. Issa, H. Rusche, Modelling of dispersed bubble and droplet flow at high phase fractions, Chem. Eng. Sci. 59 (2004) 759–770. doi:10.1016/J.CES.2003.11.018.

[88] G. Litrico, Strongly coupled models for the prediction of electrochemical reactors performances, Université de Sherbrooke, 2017.

[89] I. ANSYS, Fluent theory guide, 14.0, 2011.

[90] J. Mathieu, J. Scott, An introduction to turbulent flow, Cambridge University Press, 2000.

[91] S.B. Pope, Turbulent flows, Meas. Sci. Technol. 12 (2001) 2020.

[92] D.C. Wilcox, Turbulence modeling for CFD, DCW industries La Canada, CA, 1998.

[93] M. Lesieur, Turbulence in fluids, Springer Science & Business Media, 2012.

[94] P.A. Libby, An introduction to turbulence, CRC Press, 1996.

[95] H. Tennekes, J.L. Lumley, A first course in turbulence, MIT press, 1972.

[96] H. Schlichting, K. Gersten, E. Krause, H. Oertel, Boundary-layer theory, 9th ed., Springer, 2017. doi:10.1007/978-3-662-52919-5.

[97] J. Newman, K.E. Thomas-Alyea, Electrochemical systems, John Wiley & Sons, 2012.

[98] D. Lucas, E. Krepper, H.-M. Prasser, Use of models for lift, wall and turbulent dispersion forces acting on bubbles for poly-disperse flows, Chem. Eng. Sci. 62 (2007) 4146–4157. doi:10.1016/J.CES.2007.04.035.

[99] H. Vogt, The actual current density of gas-evolving electrodes - Notes on the bubble coverage, Electrochim. Acta. (2012). doi:10.1016/j.electacta.2012.05.124.

[100] H. Vogt, Electrochimica Acta On the gas-evolution efficiency of electrodes I – Theoretical, Electrochim. Acta. (2011). doi:10.1016/j.electacta.2010.08.101.

"This is not the end
It is not even the beginning of the end
But it is, perhaps, end of the beginning."

Winston Churchill